ABSTRACT

Title of Document: **EXPERIMENTAL INVESTIGATION OF FILM COOLING PERFORMANCE IN A SUPERSONIC ENVIRONMENT**

Matthew D. Collett
Master of Science Aerospace Engineering, 2015

Directed By: Associate Professor, Christopher P. Cadou, Department of Aerospace Engineering

This thesis reports the results of an experimental investigation of film cooling in a supersonic environment using a modified version of an apparatus originally developed by Daanish Maqbool. A test matrix of conditions relevant to those found in the nozzle extension of the NASA J-2X rocket engine was used as the basis for the testing plan. A film heater was designed and constructed to enable operation at all points in the test matrix. Temperature-time histories from thermocouples embedded in the test section walls were used to compute the spatial evolution of the film cooling effectiveness at each test condition. The results were compared to numerical simulations by NASA's Loci-CHEM CFD tool. Standard speed (30 Hz) Schlieren videos of the film injection region were recorded and new machine vision-based techniques for automatically extracting flow information from Schlieren images were implemented.

EXPERIMENTAL INVESTIGATION OF FILM COOLING PERFORMANCE IN A SUPERSONIC ENVIRONMENT

By

Matthew D. Collett

Thesis submitted to the Faculty of the Graduate School of the
University of Maryland, College Park, in partial fulfillment
of the requirements for the degree of
Master of Science
2015

Advisory Committee:
Assoc. Professor Christopher Cadou, Chair
Assoc. Professor Andre Marshall
Assoc. Professor Kenneth Yu

Table of Contents

List of Tables

List of Figures

Chapter 1: Introduction

1.1: Motivation

As a general rule, both the power and efficiency of a chemical propulsion system increases with increasing internal gas temperature [1][2]. As a result, improvements in engine performance over the last 50 years are closely related to improvements in the techniques and methods used to protect engine components from ever higher temperatures. These thermal protection techniques fall into two general categories: active and passive. Passive cooling techniques dissipate heat in a manner that does not require the expenditure of energy. Active cooling techniques require the input of energy but are more effective. Due to the large amount of heat that must be dissipated in large liquid-fueled rocket engines, passive cooling techniques are often not adequate and must be supplemented with active methods.

One important application of 'active' techniques is to the internal surfaces of rocket nozzles. Their walls are directly exposed to hot exhaust gas and if not properly cooled can quickly overheat and disintegrate. A number of active cooling methods have been developed but the most common are 'regenerative' and 'film' cooling [3]. Regenerative cooling (see Figure 1.1) involves circulating fuel through the walls of the nozzle. The fuel absorbs heat from the walls and provides the additional benefit of recovering thermal energy lost during combustion. Film cooling involves the injection of a coolant fluid along the wall of the nozzle through holes or slots so as to create a thin layer of cooler gas that separates the hotter central exhaust gasses from the wall. Many modern rocket engines use both methods to protect the thrust chamber

walls [4]. Finally, a distinguishing aspect of film cooling in rockets as opposed to gas turbines and other engines/vehicles is that extreme weight limitations require that the film fluid serve as both a coolant and a propellant. While this propulsive requirement is secondary, it is important and serves to illustrate the importance and challenge of choosing the optimum coolant.

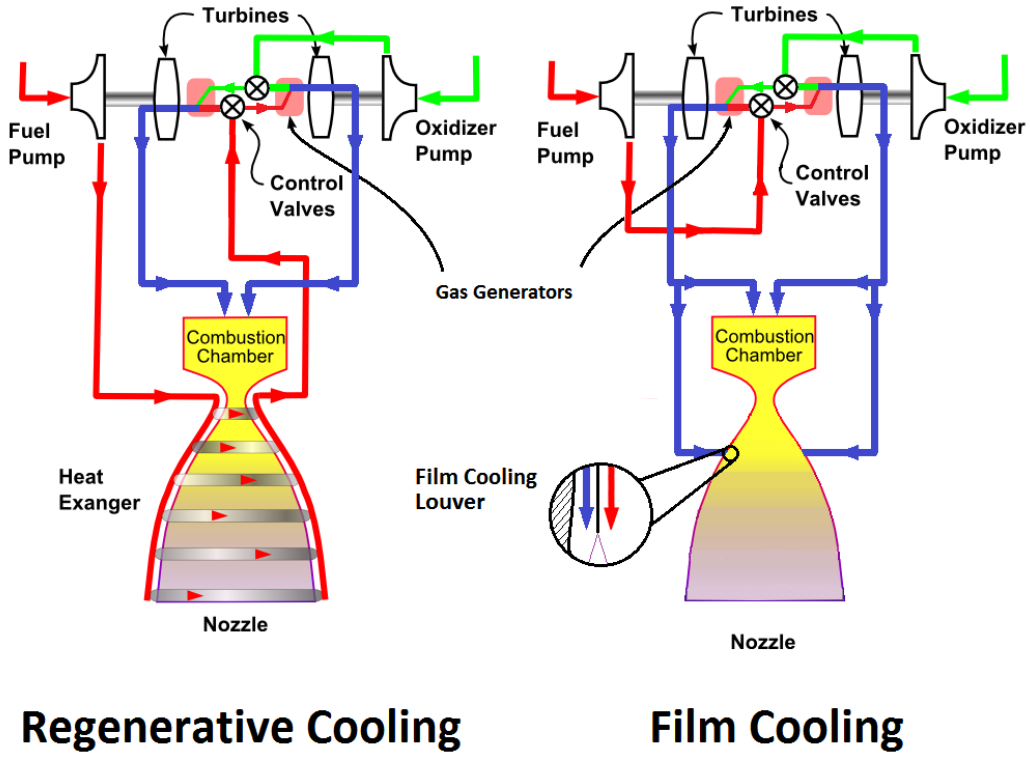

Figure 1.1: Schematic illustrations of Liquid rocket engines with Regenerative Cooling (left) and Film Cooling (right) {Adapted from Dellimore [5]}. Red indicates fuel, green indicates oxidizer, and blue indicates partially combusted fuel and oxidizer.

NASA has been successfully designing and building high-powered rockets for well over half a century. Their current effort in the area of liquid rocket engines (LRE's) is known as the J-2X. This engine is being co-developed with Pratt & Whitney Rocketdyne for use in the upper stage of NASA's next generation launch

vehicle known as the Space Launch System (SLS). This system is the replacement for the Space Shuttle and will serve to reinforce the current commercial space transportation efforts being developed in the United States. The J-2X is the result of the accumulation of design lessons that NASA has learned over its long history. Although it is a descendant of the J-2 engine that powered the legendary Saturn V launch vehicle, it incorporates a vast number of modern design elements and modern materials. This allows for high performance while also producing a robust and affordable engine.

The J-2X is of specific interest in the aerospace industry for many of its design elements, and one of the most important of these is its inclusion of a film cooled nozzle extension. The nozzle extension is required to achieve acceptable propulsive efficiency in the upper atmosphere. Cooling the approximately 8 extra feet of structure presents significant design and development challenges because there are few relevant data describing film cooling performance in accelerating flows like those found in nozzles.

NASA's current design methods rely heavily on computational fluid dynamics (CFD) to predict the performance of various critical engine components. NASA has partnered with Mississippi State University to develop a Reynolds Averaged Navier Stokes (RANS)-based generalized flow solver known as LOCI-CHEM. Unfortunately, the current version of the code is unable to predict film cooling performance with sufficient accuracy. So, NASA partnered with the University of Maryland beginning in 2007 to acquire experimental data in a series of 'canonical'

film cooling configurations that could be used to improve LOCI-CHEM's predictive capabilities.

The Maryland effort began with Dellimore [5] who studied the physics of mixing layer flows under conditions analogous to those expected in the J-2X nozzle extension. The work identified several critical parameters that influence film cooling performance: the core-to-coolant velocity ratio (r), the blowing ratio (λ), the density ratio (s), the total temperature ratio (θ_0), the Kays acceleration parameter (K_p), the convective Mach number (M_c), and the Mach number of the high speed stream (M_{HS}). The velocity ratio and acceleration parameter (r and K_p) are important for understanding the influence of pressure gradients while the other parameters (Mc, λ, s, θ_0, and M_{HS}) are important for understanding the influence of density gradients and overall flow compressibility.

This study also cleared up a significant lack of consensus in the literature regarding the effect of streamwise pressure gradients on film cooling performance: some studies said that it improved performance while others said that it degraded performance. Dellimore showed that the influence of a streamwise pressure gradient depends on whether the film cooling flow is a wall jet ($r < 1$) or core driven ($r > 1$) and was able to bring 9 of the 11 previously conflicting studies into agreement by accounting for this fact.

The results of the analysis and consultation with NASA and Pratt & Whitney Rocketdyne led to the development of a series of carefully planned experiments in the University of Maryland's supersonic wind tunnel aimed at understanding the effects of the convective Mach number and streamwise pressure gradients on film cooling

performance. This, in turn, led to the development of a test matrix in which the convective Mach number, velocity ratio and type of pressure gradient were varied.

Tests	J-2X Engine	Baseline	Off-Baseline #1	Off-Baseline #2	Off-Baseline #3
Pressure Gradient	FPG	ZPG	ZPG	ZPG	FPG
h (m)	6.35×10^{-3}	6.35×10^{-3}	6.35×10^{-3}	6.35×10^{-3}	6.35×10^{-3}
Core Film	H_2/O_2 H_2/H_20^*	Air Air	Air Air	Air Air	Air Air
M_∞ M_f	3.74 1.40	2.40 0.73	2.40 0.50	2.40 1.40	2.40 0.73
$T_{0,\infty}$ (K) $T_{0,f}$ (K)	3767 539	300 340	300 340	300 340	300 340
U_∞ (m/s) U_f (m/s)	4117.2 1833.3	568.0 255.6	568.0 180.4	568.0 438.6	568.0 255.6
T_w (K) T_∞ (K) T_f (K)	- 1667.6 323.9	340.0 139.4 307.5	340.0 139.4 323.8	340.0 139.4 244.3	340.0 139.4 307.5
$\Delta T_{f\rightarrow\infty} = T_f - T_\infty$ (K) $\Delta T_{w\rightarrow f} = T_w - T_f$(K)	1343.8 -	168.1 32.5	184.4 16.2	104.8 95.8	168.1 32.5
$s = \rho_f/\rho_c$	1.39	0.45	0.43	0.57	0.45
$\lambda = \rho_f U_f/\rho_\infty U_\infty$	0.62	0.20	0.14	0.44	0.20
$R = U_\infty/U_f$	2.22	2.22	3.13	1.30	2.22
$M_c = (U_\infty - U_f)/(a_\infty + a_f)$	1.08	0.53	0.65	0.24	0.53

Figure 1.2: Proposed test matrix developed by Dellimore [5].

Maqbool [6] designed and constructed a wind tunnel apparatus (Figure 1.3) for collecting fundamental data that can be used to validate numerical simulations of film cooling performance in the NASA/Pratt & Whitney Rocketdyne J-2X rocket engine. Particular attention was paid to selecting conditions that reflect – to extent possible in an atmospheric total T/P tunnel – those encountered in the J2X. The key non-

dimensional parameters are the velocity ratio, the convective Mach number and the type of pressure gradient. Their values and how they compare to those in the full-scale engine are presented in the test matrix illustrated in Figure 1.2. Physical explanations of these parameters are provided in Section 2.6. Note that the impracticality of reproducing rocket core temperatures in the laboratory made it necessary to 'reverse' the direction of heat transfer. Thus, heat transfer occurs from the walls to the core in the experiment. While this limits the direct applicability of the results to the 'real' engine, it is acceptable for code validation, which is the main objective of the work.

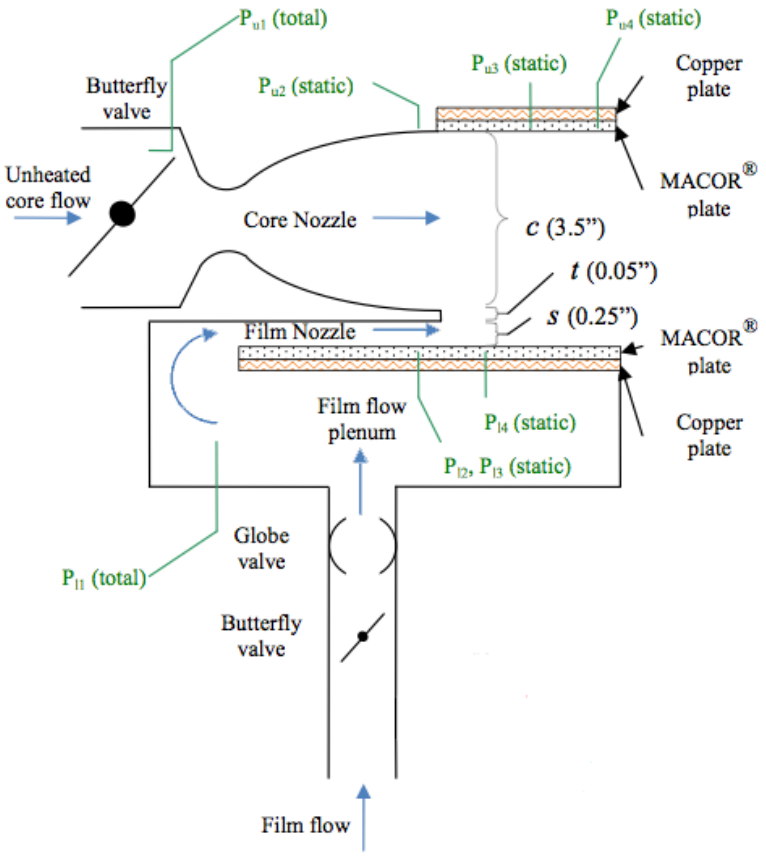

Figure 1.3: Wind tunnel apparatus as designed by Maqbool {Adapted from Maqbool [6]}.

Maqbool demonstrated the efficacy of his apparatus by acquiring some preliminary experimental data and comparing them to LOCI-CHEM CFD. The results showed that LOCI-CHEM predicted heat flux within +/- 15% in the far field (x/s > 15) but did poorly near the injection region. However, these findings were based on a very limited number of experiments and much more work was necessary. The test matrix was not explored completely, more experiments were needed at each condition in order to establish repeatability, matching Schlieren images needed to be acquired, and the film flow needed to be heated in order to ensure that all heat flux vectors pointed in the same direction. All of these improvements were necessary before the preliminary results could be confirmed or explained.

1.2: Objectives

The objectives of this thesis are twofold: 1: Use the experiment designed by Maqbool [6] to acquire sets of experimental data that are suitable for code validation following the test matrix developed by Dellimore [5]. This data set will consist of heat flux and pressure measurements at various places along the upper (uncooled) and lower (cooled) walls of the experiment and Schlieren images to visualize the shear layer growth rate. Sufficient numbers of experiments need to be performed in order to establish confidence intervals for each data point and to develop some understanding of the statistical reliability of the results. Some means of heating the film flow also needs to be devised. 2: Use machine vision techniques developed by Smith [14] to automatically extract the geometries of important flow features like shock waves and shear/mixing layers from Schlieren images. The idea is to eliminate

variability associated with human interpretation of images and to develop a tool for future investigations that can extract quantitative information from the large number of images produced by high-speed Schlieren movies.

1.3: Approach

These objectives were met by performing the following tasks:

1. Improve the initial experiment design to eliminate unforeseen structural weaknesses. Pressure fluctuations during tunnel startup caused the failure of several heat flux gauges. Additionally, the test surfaces developed cracks at key mounting locations, which eventually led to a catastrophic failure during testing. Re-designing the test surfaces will increase their durability and the reliability of the heat flux measurements.
2. Construct and implement a film heater for the experiment to fully realize all of the planned test conditions. It is important that all heat flux vectors (i.e. those between the walls and the film, and between the film and the core) point in the same direction. In order to ensure this, the total temperature of the film flow must be raised to an intermediate value lying between that of the walls (heated to 340 K) and that of the core flow (295 K).
3. Acquire at least 10 wall pressure distributions and temperature-time histories (i.e. at least 10 experiments) for each set of conditions in the test matrix. Compute the heat flux distribution from the wall temperature-time histories and use these to compute film cooling effectiveness (and uncertainty in

effectiveness) as a function of downstream distance for each condition in the test matrix.

4. Acquire Schlieren images (in the form of video) of flow structures at each point in the test matrix.
5. Use automated Schlieren interpretation techniques recently developed by Smith [14] to extract the geometries of flow features from the Schlieren video. The flow features being sought (in order of importance) are:
    a. Shear layer between core and film flows.
    b. Shockwave emanating from film injection lip (lip shock).
    c. Shockwaves emanating from nozzle geometry or imperfections in test surface.

Chapter 2: Background and Previous Work

2.1: Film Cooling Background

Film cooling is an active cooling technique that is frequently used to protect components in modern rocket and gas turbine engines. It involves the injection of a coolant fluid through a series of small holes or slots in order to create a protective barrier between the wall and the hot core flow. A shear layer forms at the interface between the hot outer ('core') and the film. It begins at the point of coolant injection and spreads downstream until its lower boundary reaches the wall as illustrated in figure 2.1 Predicting the location of this impingement point is very important because the thermal protection provided by the film degrades rapidly beyond it.

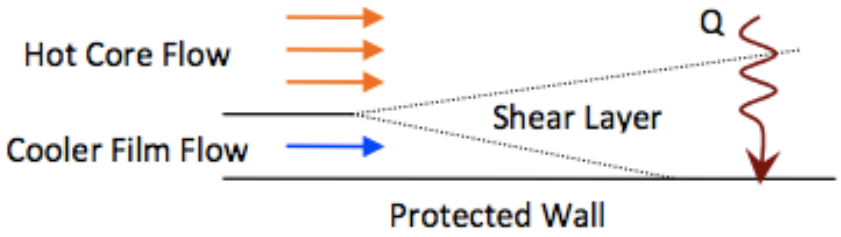

Figure 2.1: Schematic of film cooling experiment showing expansion of shear layer {Adapted from Maqbool [6] (2011)}.

An important distinction to make in the study of film cooling is the difference between the velocities of the core and film flows. A film with a core flow velocity greater than that of the film flow is referred to as a "core driven". The opposite case - in which the film flow has a greater velocity than the core flow - is referred to as a "wall-jet". This difference is illustrated in figure 2.2.

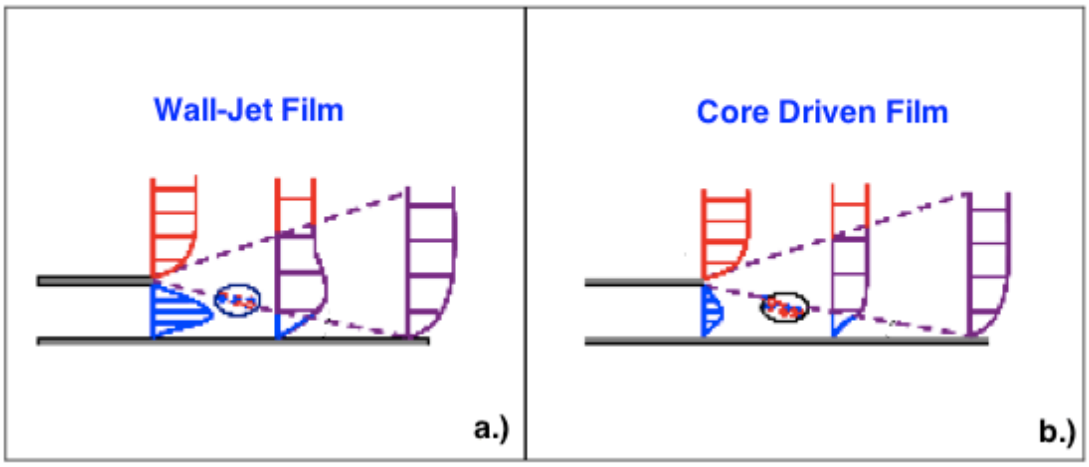

Figure 2.2: Velocity profiles of a.) Wall-Jet Film and b.) Core Driven Film {Adapted from Dellimore [5] (2010)}.

A common metric of film cooling performance is the effectiveness [7]. One definition is based on temperatures:

$$\eta(x) = \frac{T_w(x) - T_r}{T_f - T_r} \tag{2.1}$$

In this equation T_w is the adiabatic wall temperature, T_f is the recovery temperature of the film flow, and T_r is the recovery temperature of the core flow. Physically, it is a non-dimensional temperature difference. The recovery temperature of the flow is the 'real world' value of the total temperature when energy losses during stagnation are accounted for. Equation 2.1 shows that the effectiveness depends upon downstream distance from the injection point. At the point of injection, the wall temperature T_w should be the same as the recovery temperature of the flow, T_r and $\eta = 1$. The effectiveness decreases with downstream distance due to the growth of the shear layer. Farther downstream, the shear layer contacts the wall resulting in a large

temperature spike and the eventual breakdown of the film layer. At this point, T_w approaches T_r and η approaches 0.

Another way to think about film cooling effectiveness is in terms of local heat fluxes [8]:

$$\eta(x) = 1 - \frac{Q(x)}{Q_0} \tag{2.2}$$

In this expression, *Q(x)* is the heat flux into the wall through the protective film layer and Q_0 is a 'reference' heat flux associated with an unprotected wall. Note that this could either be a film cooled wall with no flow being injected or a wall designed without any film cooling at all. *Q(x)* generally increases with downstream distance as the shear layer grows and the film layer breaks down. This implies that *Q(x = 0)* is expected to be minimum. It follows from equation 2.2 that η will be maximum at *x=0* and decrease with increasing distance from the injection point. Heat transfer is expected to 'spike' in the region where the shear layer contacts the wall and thus η approaches 0 as *Q(x)* approaches Q_0.

2.2: Image Analysis Background

Two of the most common techniques for studying shear layer growth rates are Particle Image Velocimetry (PIV) and Schlieren imaging. PIV is a technique that uses small tracer particles, an illumination source (laser or strobe), and a camera to make instantaneous measurement of velocity in a plane. The size of the particles is selected to closely follow the smallest possible fluid dynamic scales while still scattering enough light to be visible [9]. While it has been used extensively to study shear layer growth [10][11], implementing it in this experiment would be extremely challenging

because of the need to seed both the core and film flows and because of the large amount of seed that would be required.

Schlieren imaging is a very well-established technique for visualizing density gradients. It involves passing a collimated light beam through a flow field and using a system of mirrors or lenses to focus an image of the constant illumination onto some kind of screen or detector array. A 'stop' (which can be a knife edge or a pinhole) is placed at the focal point of the optical system between the test section and the screen/detector array. Density gradients in the flow steer individual rays into or over the stop resulting in patterns of light and dark on the image that correspond to the local magnitudes of the density gradients in the test section [12]. Schlieren photography is simple to perform and has been used for years to measure shear layer growth rates in supersonic flows [13]. However, extracting growth rates from these images is somewhat inexact as it relies on human interpretation of photographic images. This is particularly problematic here as supersonic shear layer growth rates are quite small and their edges somewhat indistinct.

Recently, image processing techniques originally developed for machine vision applications have been adapted by Smith et. al. [14] to make automated measurements of shock angles in high speed schlieren movies of shock-boundary layer interactions. Therefore, an important objective of this thesis is to try to use these image processing techniques to extract shear layer growth rates automatically.

2.3: Previous Work: Film Cooling

Film cooling has been studied extensively for well over a half century. Both general knowledge studies and studies for specific applications have greatly

contributed to the information base that is available today. Boden published one of the earliest film cooling studies focused on rocket applications in 1951 [15]. This study investigated and compared the effects of film cooling and sweat cooling[1] on a rocket motor with 1000 lbs of thrust. The injected coolant for both types of cooling was water. His results showed that film cooling outperformed sweat cooling by approximately 10-15% and showed that the overall heat transfer near the throat of the rocket motor could be reduced by almost 75%.

Goldstein et al performed another important early study of supersonic film cooling in 1966 [16]. It investigated a flat plate in a Mach 3.01 core flow film cooled through a step down slot. Both air and helium coolants were investigated. The blowing ratio λ (referred to as M in the study) was set at 0.408 for air and between 0.01 and 0.02 for helium. Rather than heating the core flow, the study took the opposite but analogous approach of heating the film. This reversed the direction of heat transfer but still allowed the investigation of film cooling effectiveness in a manageable fashion. The results of the adiabatic wall temperature measurements showed that film cooling effectiveness is close to 1 for some distance downstream and then falls off on an approximately exponential curve. The results for the injection of air show that increasing the blowing ratio up to a value of 0.13 increases the protection of the film slowly. Increasing the blowing ratio beyond this value increases the protected area at a more rapid rate (see figure 2.3). In addition to the work on film cooling effectiveness, Goldstein also performed Schlieren imaging of the injection slot area [16]. These images clearly show the basic flow structures including lip

[1] Sweat cooling is an alternative active cooling method that requires the use of specialized porous walls. Liquid coolant is forced through the walls in order to lower their temperature. This method is also referred to as transpiration cooling.

shocks and shear layer mixing area. He also noted that as the blowing ratio was increased, the reattachment point of the compression shock moves downstream and decreases in strength until it eventually disappears. This was due to the increased protection offered by the higher blowing ratio.

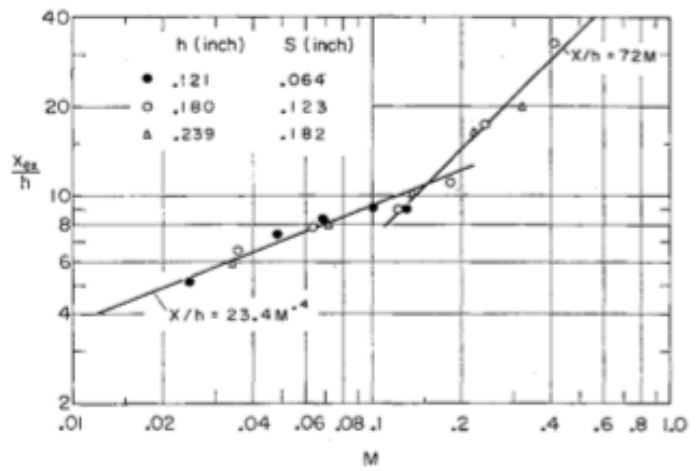

Figure 2.3: Plot showing distance (normalized by slot height) fully insulated by film for increasing blowing ratio {Adapted from Goldstein [16] (1966)}.

Hunt, Juhany, and Sivo presented another major film cooling work in 1991 [17]. In this study, the relationship between film cooling effectiveness and injection Mach number, velocity, and mass flux were examined. A core Mach number of 2.4 and injection Mach numbers ranging from 1.2 to 1.9 were investigated with both air and helium as coolants. They concluded that in general, film cooling effectiveness increased as the blowing ratio λ increases. They also noted that with larger film Mach numbers, there is a slight increase in the effective cooling length per mass injection rate - similar to what was found in Goldstein et al [16]. Another interesting finding was that effectiveness profiles for both air and helium collapsed to a single line when the blowing ratios were the same and the streamwise distance was non-

dimensionalized by the slot height. This confirmed similar findings by Bass et al [18]. The researchers also concluded that helium performed better as a coolant than air.

A more recent study by Aupoix et al. [19] was done with very similar motivations to the current one. The objective was to replicate conditions found in a VULCAIN rocket nozzle [20], make measurements, and compare them to values obtained through computer simulations of the same nozzle. Replicating the exact conditions found in the engine was deemed impossible given the limitations of the facility. Therefore the study was designed to match the convective Mach number and blowing ratio found in the VULCAIN nozzle as closely as possible. The experiments used a half nozzle configuration with a core flow Mach number of 2.78 and a film flow cooled with liquid nitrogen to 125 K and injected at a Mach number of 2. A film injected at ambient temperature was also studied in order to examine the relationship between film temperature and mixing layer growth rate. In addition to investigating two different film temperatures, the pressure ratio between the film and core flow was varied to study three cases: an underexpanded film (pressure of the film greater than that of the core), pressure matched (pressure of the film and core flows equal), and overexpanded film (pressure of the film less than that of the core). This investigation showed that an underexpanded film provided better protection than both a pressure matched or an overexpanded film (see figure 1.3). Schlieren imaging of the film injection region also showed that as the film pressure was increased, the impingement location of the shock emanating from the film injection lip moved downstream (analogous to the phenomenon noted in Goldstein et al [16]).

In addition to these findings, Aupoix et al. closely examined the results of several different numerical techniques to match the results obtained through the experiment. They noted that although the type of method (a boundary-layer approach) used to calculate the solution was not appropriate for all of the flow, it provided a computationally inexpensive way of investigating film cooling as long as a two-equation turbulence model was used. The boundary-layer approach struggled to correctly reproduce the results of the experiment close to the injection point, but was able to predict wall temperature farther downstream. The ability to correctly calculate much of the flow field in addition to being inexpensive computationally makes this approach an attractive method for gaining initial insight into film cooling flows.

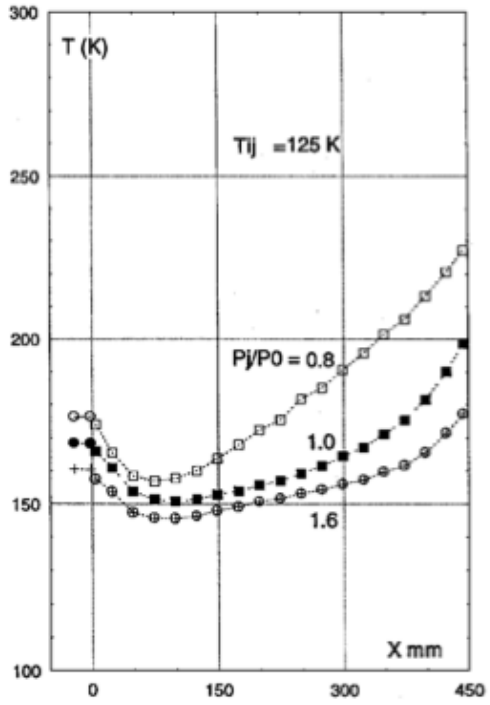

Figure 2.4: Wall temperature distribution for three separate film to core pressure ratios, Open squares: Overexpanded film ($P_i/P_0 = 0.8$). Solid squares: Pressure matched film ($P_i/P_0 = 1.0$). Solid circles: Underexpanded film ($P_i/P_0 = 1.6$) {Adapted from Aupoix [19] (1998)}.

2.4: Previous Work: Schlieren Imaging and Image Analysis

Schlieren photography has been used extensively in aerospace applications for almost 150 years. The man credited with first applying Schlieren photography to visualize fluids, August Toepler, developed the method in 1864 [21]. He used the optical technique to examine the shock waves generated by electric sparks in air. In addition, he developed a very fast delay circuit that allowed him to generate a spark and then illuminate the shockwave created by that spark with a second spark. This initial work in Schlieren photography was an inspiration to Ernst Mach who eventually improved Toepler's time delay circuit and used the technique to study the interaction between multiple shock waves. Subsequent modifications of Schlieren photography led to the development another optical technique called shadowgraphy [22].

Many diagnostics advances in the early 20th century were driven by innovation in the field of ballistics imaging. The invention of the Cranz-Schardin camera capable of capturing up to 24 images at a time at one million frames a second [23] was a huge step forward in Schlieren photography that enabled the study of very high speed flow phenomena. Schardin continued to advance Schlieren photography throughout his career and published an incredibly broad and important work on Schlieren imaging in 1942, "Schlieren Methods and Their Applications" [24]. In this all-encompassing work, scores of high quality photographs accompany explanations of the mathematical theory behind many techniques and the introduction of several new Schlieren methods and systems. This work drove the field forward for decades and

some of the methods introduced such as the lens-grid focused Schlieren technique are just beginning to be utilized today.

Schlieren photography, like other optical techniques, has evolved to exploit the inexpensive processing power available with modern computers. One example is recent work by Smith et al [14], which has shown that computer vision techniques can identify and measure flow structures automatically. This is demonstrated on a set of high-speed Schlieren photographs of double cone structures created by a Mach 14 free stream flow (Figure 2.5). The algorithm correctly identified flow structures and measured shock angles with an approximately 95% success rate. This is an important development because removing the need for human interpretation of images could make Schlieren imaging techniques quantitative and greatly facilitate making comparisons between experiments.

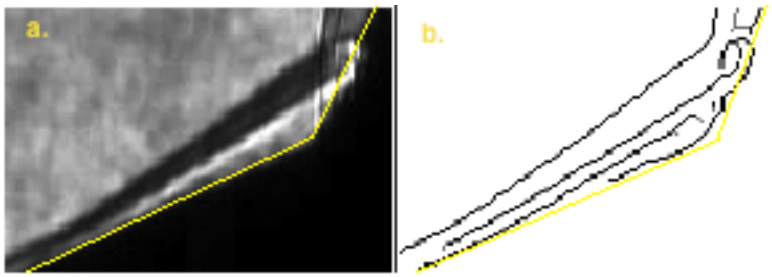

Figure 2.5: Example of Schlieren photograph interpreted with Canny edge detection. Yellow lines indicate approximate wall boundaries of double cone experiment used by Smith. a.) Original image b.) Edges detected by Canny algorithm {Adapted from Smith [14] (2012)}.

The Schlieren photography with machine-vision interpretation is a powerful pairing that combines the highly useful optical capabilities of Schlieren with the repeatability and quantitative power of computers. Using these methods together enables one to extract quantitative information about flow structure using relatively simple apparatus.

2.5: Previous Work: Heat Flux Measurements

Many different types of studies require heat flux measurements to be made. Film cooling studies often require that heat flux be obtained for the calculation of film cooling effectiveness (defined previously as equation 2.2). There are several different methods of gathering heat flux data including thin-film gauges, slug calorimeters, and embedded temperature sensors [28]. All of these methods are suited to different types of experiments and have drawbacks that limit their usefulness in certain testing scenarios.

Thin-film gauges consist of a temperature sensor that is placed on the surface of the test article being investigated (see figure 2.6). This sensor can be either a thermocouple or a thermistor and provides a temperature-time history of the surface of the material. Assuming that the thickness of the test surface is effectively semi-infinite (i.e. that the experiment is of short enough duration that the thermal wave does not reach the back side of the test surface before the experiment is over), a numerical model of heat transfer within the wall can be used to infer the heat transfer into the wall from the surface temperature-time history [29]. This method has a very short response time and is extremely useful in short duration tests like those performed in shock tunnels. However, the presence of these gauges on the surface of the experiment can disturb the flow and complicates their use in film cooling experiments – especially those in the supersonic regime.

Slug calorimeters are small masses made of highly conductive material with a temperature sensor located at the center. If they are embedded in the test surface (see figure 2.6) any effect on or disturbance to the flow is eliminated. As heat is

transferred to the surface and gauge, the temperature of the slug rises. A key requirement is that the thermal conductivity of the slug material be much higher than that of the substrate into which it is embedded so that its effective Biot number is small. The main disadvantages of slug calorimeters are that response times can be slow and that they introduce a non-uniformity in the thermal properties of the wall that distorts the temperature field and thus potentially corrupts the heat flux measurement.

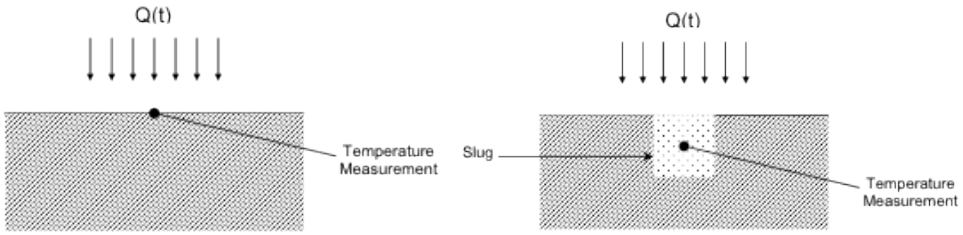

Figure 2.6: (left) Schematic showing placement of thin-film gauge. (right) Schematic showing placement of slug calorimeter gauge {Adapted from Maqbool [6] (2012)}.

Temperature sensors embedded within the test surface provide another method of measuring heat flux. This method uses the temperature-time history of a thermocouple embedded inside the test surface to infer heat transfer and surface temperature through the use of the one-dimensional conduction equation [31][32]. Mechanically, this is a robust and simple method that does not disturb the test surface or the flow past it. However, the determination of heat flux from the temperature-time history of the embedded gauge is an extremely complex process and is usually only performed by specialists in that area [33][34][35][36][37][38]. Recent work by Maqbool [6] showed that under the conditions expected in the film cooling experiments, the problem can be simplified greatly at little cost in accuracy.

Therefore, the methods of Maqbool are used in this study to infer surface heat fluxes from temperature-time histories of subsurface points in the wall.

2.6: Test Conditions and Cases

2.6.1: Test Case Design

A number of non-dimensional parameters were identified by Dellimore [5] as being important for describing film cooling flows. The following parameters are the most relevant to this study: the convective Mach number M_C, the blowing ratio λ, the density ratio s, and the velocity ratio r [5]. These are defined as:

$$M_C = \frac{u_\infty - u_f}{a_\infty + a_f} \tag{2.4}$$

$$\lambda = \frac{\rho_f u_f}{\rho_\infty u_\infty} \tag{2.5}$$

$$s = \frac{\rho_f}{\rho_\infty} \tag{2.6}$$

$$r = \frac{u_\infty}{u_f} \tag{2.7}$$

The values of these parameters in the film cooling situation expected in the J-2X nozzle extension are presented in Table 2.1. An ideal experiment would match all of these non-dimensional parameters but actually doing so is impractical in almost any laboratory setting because of the extremely high temperatures and velocities of the 'real' flow.

The objective is to study film cooling effectiveness in an environment that is as relevant as possible to the one present in the J-2X nozzle extension. However, it is impossible to match the J-2X density or blowing ratios in the Maryland supersonic

wind tunnel because it is an atmospheric total pressure/temperature facility. Therefore, the goal was to select conditions that are expected to produce significant variations in the shear layer growth rate and the convective Mach number while getting as close as possible to true J-2X conditions. The wind tunnel will be described more completely in Chapter 3. Analyses undertaken by Dellimore [5] and Maqbool [6] led to the test matrix presented in Table 2.1.

Table 2.1: Experiment Test Matrix

	J-2X	***Test Case 0***	***Test Case 1***	***Test Case 2***	***Test Case 3***
Pressure Gradient	FPG	ZPG	ZPG	ZPG	ZPG
Core	H20	Air	Air	Air	Air
Film	H20, H2	Air	Air	Air	Air
M_∞	3.74	2.40	2.40	2.40	2.40
M_f	1.4	0.00	0.50	0.73	1.40
$T_{0,\infty}$ **(K)**	3767	300	300	300	300
$T_{0,f}$ **(K)**	539	N/A	340	340	340
u_∞ **(m/s)**	4117	568.0	568.0	568.0	568.0
u_f **(m/s)**	1833	N/A	180.4	255.6	438.6
M_C	1.08	2.40	0.65	0.53	0.24
λ	0.62	N/A	0.14	0.2	0.44
s	1.39	0.0	0.43	0.45	0.57
r	2.22	N/A	3.13	2.22	1.30

Note also that the direction of heat transfer is reversed in these experiments (ie. the walls lose heat to the flow) compared to the J-2X engine in which the flow loses heat to the walls (see Figure 2.7). This approach has been taken previously in literature by Goldstein et al. [16] and is not expected to change the key physical

aspects of the problem for the film cooling application – as long as the total temperature of the film lies between that of the wall and the core flow (ie. the heat flux vector does not change sign between the wall and the film and the film and the core). Since this is an atmospheric total temperature tunnel, this means that both the film and test surfaces must be heated to a temperature that is greater than ambient. It also means that the total temperature of the film must lie between that of the wall and the core flow to ensure that all of the heat flux vectors point in the same direction. In this experiment, the total temperature of the film was the same as that of the test surface in order to ensure that the wall heat flux at the film injection point is zero. Cartridge heaters are used to heat the walls to 40 degrees C above ambient as described by Maqbool [6]. The film is heated using a propane-fueled combustor that will be discussed in Chapter 3.

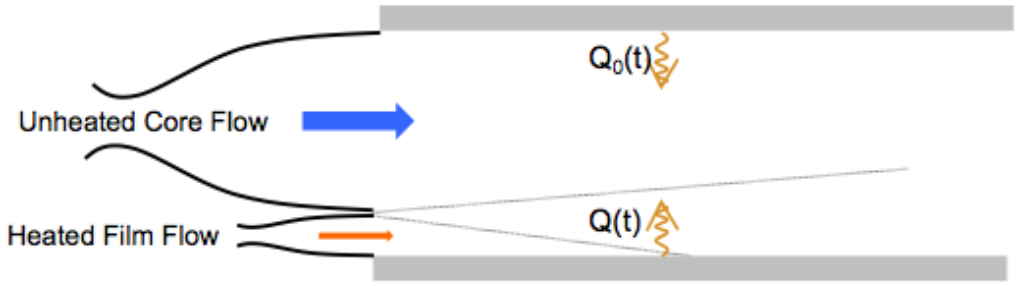

Figure 2.7: Reverse Film Cooling arrangement studied in experiment {Adapted from Maqbool [6] (2012)}.

In addition to the test cases listed in Table 2.1, test cases 1, 2 and 3 were also performed without heating the film. These measurements were made as an initial investigation of the flow physics before the film-heating device described in chapter 3

was constructed. These results are presented along with the results from the heated film flow in chapter 4.

2.6.2: Loci-CHEM CFD Simulations

The primary focus of this study is the acquisition of a large amount of film cooling data that can be used to validate LOCI-CHEM (NASA's preferred design tool) simulations under conditions that are relevant to the J-2X film cooling problem.. This entails making enough film cooling measurements at each of the test conditions proposed in Table 2.1 so that plots of measured film cooling effectiveness vs. downstream distance can be generated and that the uncertainty in the measured effectiveness profiles is known. The design tool will be validated by comparing film cooling effectiveness computed from the LOCI-CHEM simulations to those computed from the results from this experiment. The LOCI-CHEM simulations that have been performed are summarized in Table 2.2. Some simulations were performed at NASA Marshall by Joe Ruf while others were performed at UMD by Dellimore [5] (p. 213-244). While the table shows that at present simulations of unheated wall situations are only available for the no film injection case (*Case 0*) and the supersonic injection case (*Case 3*), experimental results from all cases are included in this study in order to provide bases of comparison to future simulations.

Table 2.2: Summary of CFD results obtained from NASA and Dellimore.

	NASA CFD		***Dellimore CFD***	
Case 0	***Yes***		***Yes***	
	Heated	***Unheated***	***Heated***	***Unheated***
Case 1	No	No	Yes	No
Case 2	No	No	Yes	No
Case 3	Yes	Yes	Yes	No

Chapter 3: Apparatus

3.1: Experiment Overview

3.1.1: Supersonic Wind Tunnel

All experiments were conducted in the University of Maryland supersonic wind tunnel. It is a blow-down facility that is capable of producing flows of up to Mach 3 through a rectangular, 6-inch wide test section for at least several seconds (see Figure 3.1). The operation of the tunnel starts with the evacuation of the test section and large tank at the test section exit, which serves as the low-pressure reservoir to a pressure of approximately 2 in Hg. A pneumatically actuated butterfly valve located immediately upstream of the test section (and nozzle) entrance seals the system for evacuation and is opened to initiate flow from the room into the test section. A separate valve seals the film flow intake and is opened simultaneously with the main valve when an experiment is begun.

Figure 3.1: University of Maryland supersonic wind tunnel. In near field right, the intake bell (a.) can be seen. In the center of the picture, the butterfly valve and control arm are shown (b.). At the far left is the test section housing the experiment and instrumentation (c.).

3.1.2: Film Cooling Test Section

The flow through the core of the experiment test section is initiated using a converging-diverging nozzle designed to generate Mach 2.4 flow. Flow passes through this nozzle into the constant area test section (see Figure 3.2). Flow through the film intake passes into a plenum and is then drawn through a slot and injected through a nozzle located on the underside of the core flow nozzle. This nozzle is designed to produce a Mach 1.4 film[2] parallel to the wall and core flow. It is important to note that the film nozzle expands the flow in a span-wise direction (i.e. perpendicular to the expansion in the core nozzle.)

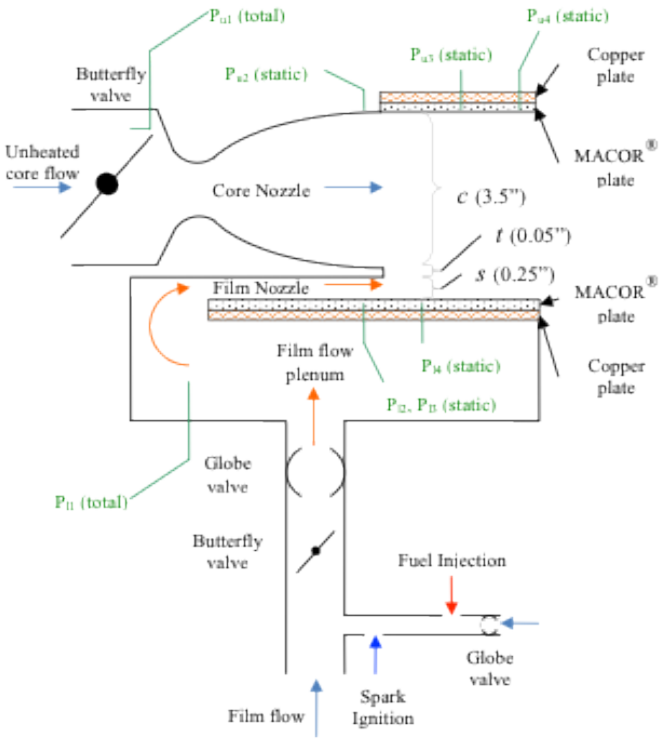

Figure 3.2: Schematic of test section showing main core intake, film intake, and approximate location of pressure sensors {Adapted from Maqbool [6] (2012)}.

[2] Note: The film injection nozzle is not always operated at Mach 1.4. This was the design condition for pressure matched supersonic injection. It is also operated at pressure conditions that produce Mach 0.50 and Mach 0.73 films.

The butterfly valve controlling the film intake is operated by a solenoid that opens at the same time as the tunnel main valve. The flow through the film cooling louver is controlled by a globe valve installed in the film flow intake. Varying the opening of this valve adjusts the total pressure in the film flow plenum. As long as the pressure difference between the plenum and the Mach 2.4 core remains large enough to sustain supersonic flow in the louver, it is possible to adjust the globe valve to match the louver exit pressure to that of the free-stream so that no shocks or expansion waves form at the louver exit. The velocity ratio can be controlled to a certain degree by varying the total temperature of the louver flow but it must remain between the wall temperature and free-stream recovery temperatures. The louver total temperature is usually set to be between the wall and free-stream recovery temperatures. The louver total temperature ranges from 5 K to 15 K below the wall temperature depending on the case being studied. Subsonic (and inherently pressure-matched) louver flows are generated at smaller pressure differences (valve openings). Test times range from approximately 4.5 seconds for supersonic injection up to 6 seconds for no film injection.

The test section walls are made of a specialized machinable ceramic (MACOR®) attached to a solid copper backing plate with embedded cartridge heaters (see Figure 3.3). The heaters are used to raise the temperature of the walls above the recovery temperature of the flow, which is approximately 280 K [6]. The MACOR® material was chosen for its electrically insulating properties as well as its very low thermal diffusivity. A more detailed explanation of this material choice is presented elsewhere

[6]. The wall thickness is set to ensure that the wall behaves as a thermally semi-infinite structure. This is a necessary condition for the 1-D model used to infer heat flux from subsurface temperature-time histories. In order to ensure this condition, the thickness of the plate and spacing of the individual temperature sensors must be greater than the thermal penetration depth of the heat transfer during the experiment. It has been shown [39] that this condition is met as long as the thickness of the plate and sensor spacing are at least:

$$d \geq 4\sqrt{\alpha t} \tag{3.1}$$

where d is the thermal penetration depth, α is the thermal diffusivity of the material, and t is the duration of the experiment. This yields a required minimum thickness of $d = 0.33$ *in.* A plate thickness of 0.625 inches was used in the final experiment. This distance was also used for the minimum spacing distance between heat flux sensors.

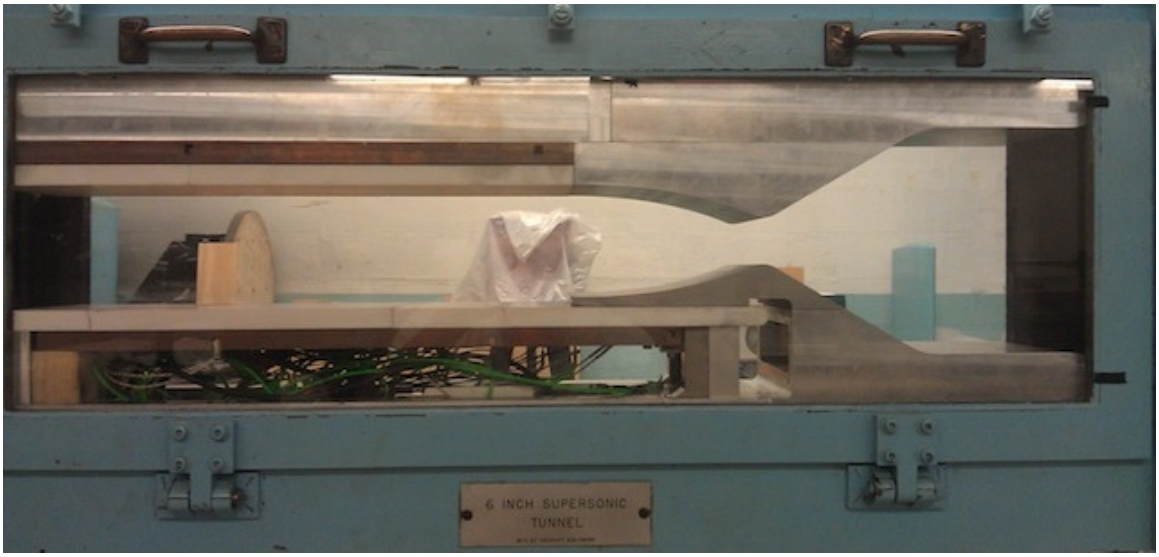

Figure 3.3: Full experiment installed in wind tunnel. Nozzle blocks can be seen on the right side of the test section feeding into the instrumented MACOR® surfaces in the center. These surfaces are attached to the copper heating plates.

The nozzles for both the core flow and film flow were designed using the method of characteristics [6](p 26-27) [40](p 261-282). The core and film nozzles were

designed to produce Mach numbers of 2.4 and 1.4 respectively. The entire mechanical structure was constructed of aluminum except for the film injection nozzle, which had to be constructed of steel because of the extremely thin cross-section at the discharge plane.

3.1.3: Instrumentation

The basic quantities being measured and recorded in this experiment are pressure and temperature. The pressure measurements are used to establish the film condition (P, M) as it exits the louver and to determine the strength of shocks, expansions, and other structures in the flow. Most pressure measurements are made along the wall but pressure is also measured in the film plenum, upstream of the nozzle, at the nozzle exit, and outside of the tunnel (in order to obtain atmospheric conditions). Most temperature measurements come from thermocouples embedded in the walls (for measuring heat flux) but thermocouples are also located in the film plenum to measure total temperature and outside the tunnel to measure atmospheric pressure. The locations of the static pressure taps are listed in Table 3.1 and illustrated schematically in Figure 3.4. Note that 'lower' in the figure refers to the film cooled wall on the bottom of the test section (see Figure 3.3) and 'upper' refers to the upper wall of the test section.

Total pressures are measured using a pitot probe in the core stream before the nozzle contraction and in the film flow plenum to determine the respective core and film total pressures.

Table 3.1: Pressure tap locations

Sensor	***Location (x/s)***	***DAQ Channel***	***Status***
P_{l1}	Film Plenum	NI-9205-4	Active
P_{l2}	-0.6	NI-9205-5	Active
P_{l3}	-0.6	NI-9205-6	Active
P_{l4}	3.75	NI-9205-7	Active
P_{l5}	17.5	-	Not Connected
P_{l6}	32.5	-	Not Connected
P_{l7}	55	-	Not Connected
P_{u1}	Upstream of Nozzle	NI-9205-0	Active
P_{u2}	Nozzle Exit	NI-9205-1	Active
P_{u3}	17.5	NI-9205-2	Active
P_{u4}	60	NI-9205-3	Active
P_{u5}	32.5	-	Not Connected

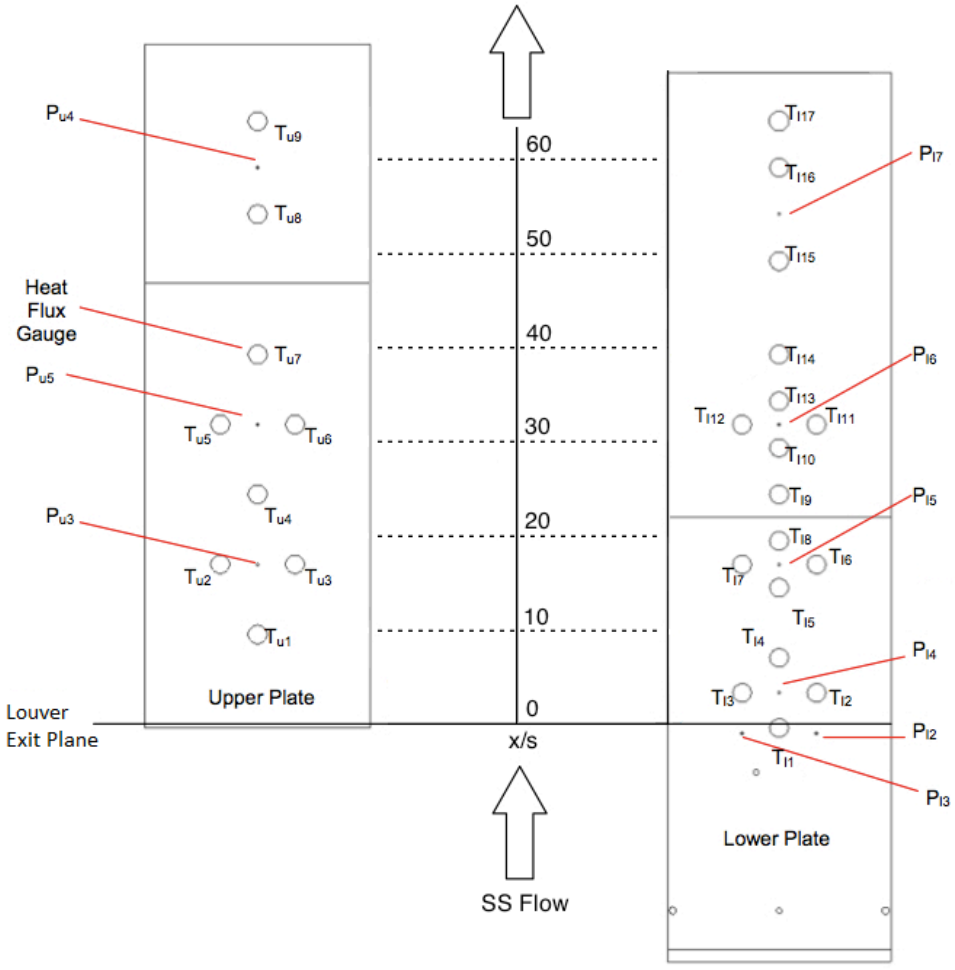

Figure 3.4: Locations of pressure taps and heat flux gauges along upper and lower testing surfaces.

The Mach numbers of the core and film flows were determined using the total pressure measurement for each flow and the static pressure measurement at each nozzle exit. Due to the limited number of data acquisition channels, only three pressure taps along the lower wall were utilized during experimentation (see Table 3.1). Each pressure tap was connected to an Omega PX309-015A5V voltage output absolute pressure transducer. Approximately 24-inch lengths of 1/16 inch ID plastic tubing ran from the taps and through the tunnel walls to the transducers, which sat on top of the tunnel and outside of the test section. The transducers have a 0-15 psia range and output a voltage between 0-5 volts with a frequency response of 1000 Hz.

The heat flux gauges consist of 0.50-inch diameter thermocouples held just below the test surface by MACOR plugs inserted into matching flat bottomed bores in the back side of the MACOR walls. Grooves on the side of each plug and across one accommodate the beads and leads of T-type unsheathed butt-welded thermocouples. The junction is centered on the face of the MACOR cylinder and the thermocouple/plug assembly is coated with Thermaltake TG-2 heat transfer grease to ensure good thermal contact between the plugs and the bores. Figure 3.5 is an illustration of the assembled gage installed in the bore. Heat flux is computed from the temperature-time history of the thermocouple embedded in the wall in this manner.

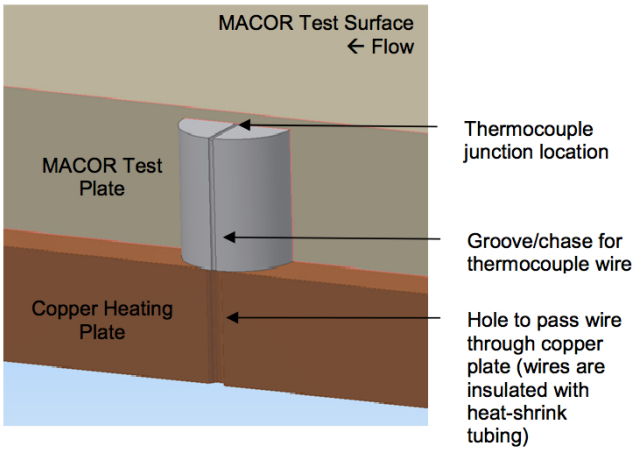

Figure 3.5: Thermocouple assembly in MACOR ® test surface {Adapted from Maqbool [6] (2012)}.

The heat flux gauges were installed on both the upper and lower walls at locations starting at the film injection point and continuing downstream. Most sensors were placed on the centerline but some sensors on both the upper and lower walls were placed off-centerline in order to assess three-dimensional effects. Table 3.2 reports the locations of all temperature sensors embedded in the upper and lower walls in terms of x/s (streamwise position downstream of the louver exit divided by the height of the louver (0.25 inches)). It is important that the embedded temperature sensors be as close to the surface of the material as possible in order to maximize the temperature change measured over the course of an experiment. The limiting factor is the strength of the thin layer of MACOR® at the bottom of the bore that separates the thermocouple from the flow. The initial design by Maqbool placed the thermocouples 0.050 inches below the surface but this distance proved too small. A re-design of the test section and sensors in order to make them more robust will be described in section 3.3.

Table 3.2: Summary of temperature sensor locations for re-designed experiment

Sensor	***Location (x/s)***	***DAQ Channel***	***Status***
T_{l1}	0	N-9213-0	Active
T_{l2}	3.75	N-9213-1	Active
T_{l3}	3.75	N-9213-2	Active
T_{l4}	7.5	N-9213-3	Active
T_{l5}	15	N-9213-4	Active
T_{l6}	17.5	-	Not Connected
T_{l7}	17.5	-	Not Connected
T_{l8}	20	N-9213-5	Active
T_{l9}	25	N-9213-6	Active
T_{l10}	30	N-9213-7	Active
T_{l11}	32.5	N-9213-8	Active
T_{l12}	32.5	N-9213-9	Active
T_{l13}	35	N-9213-10	Active
T_{l14}	40	N-9213-11	Active
T_{l15}	50	N-9213-12	Active
T_{l16}	60	N-9213-13	Active
T_{l17}	65	N-9213-14	Active
T_{u1}	10	N-9213-0	Active
T_{u2}	17.5	N-9213-1	Active
T_{u3}	17.5	N-9213-2	Active
T_{u4}	25	N-9213-3	Active
T_{u5}	32.5	N-9213-4	Active
T_{u6}	32.5	N-9213-5	Damaged
T_{u7}	50	N-9213-6	Active
T_{u8}	55	N-9213-7	Active
T_{u9}	65	N-9213-8	Active

All data were logged on a Lenovo R500 PC running LabView 8.6. Separate data acquisition modules and chassis were used for the temperature and pressure sensors. In order to minimize the number of penetrations through the wind tunnel wall, two thermocouple amplifiers (NI-9213 TC modules mounted on a NI USB-9162 single-slot chassis) and 24 bit A/D converters were located within the test section (one each in the upper and lower wall). The DAQ systems were connected to the data logging computer via an air-tight feed through and a USB cable. The 16 channels of temperature data were acquired at 50 Hz. The pressure data were recorded at 500 Hz using a 16-bit NI-9205 A/D module installed in an NI cDAQ-9178 chassis.

3.2: Film Heater

Section 2.6 explained that it is necessary to heat the film so that its recovery temperature (T_f) lies between the wall temperature (T_w) and the recovery temperature of the core flow ($T_{r,\infty}$). The short test time (~5 sec) and large contact area and current flow required by electrical solutions rendered them impractical. A relatively simple and cost-effective solution is a propane-fired vitiated air heater. In this configuration, a small burner is used to heat a portion of the air entering the film flow intake (see Figures 3.6 and 3.7).

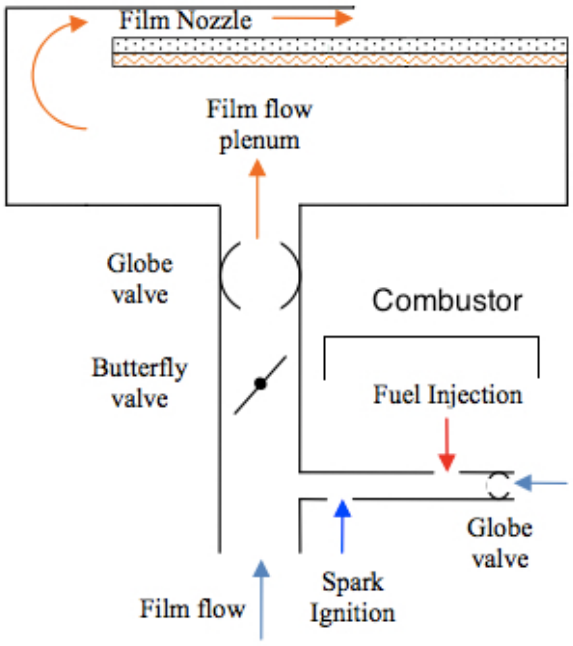

Figure 3.6: Diagram of film heater attached to film flow intake. Heated air mixes with the main film flow and enters the plenum before being injected through the film nozzle. A solenoid opens the butterfly valve at the same time as the main tunnel butterfly valve opens.

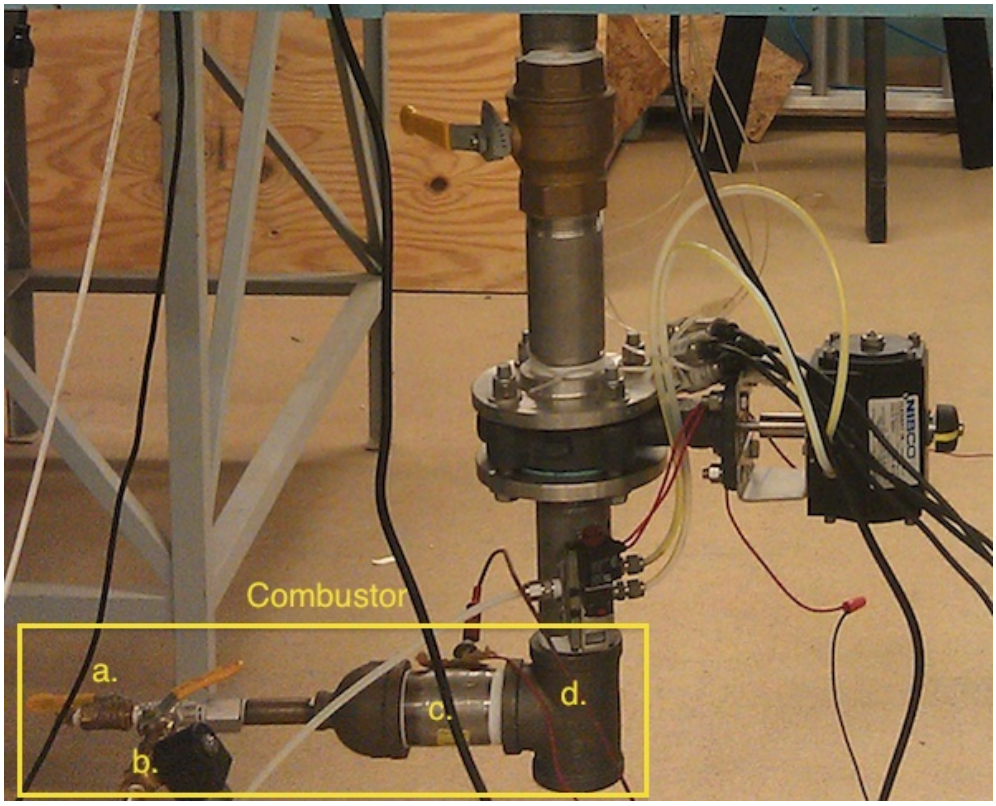

Figure 3.7: Film burner and intake. The combustor is visible on the lower left of the photograph. Air enters from the left (a.) and is mixed with propane entering through a globe valve (b.). It then enters the combustion chamber and is ignited (c.). The heated air then joins with flow from the main intake (d.) and travels upward into the plenum.

Identifying the proper fuel-air ratio for all of the test cases was a necessary first step in the design of the film flow heater. Of particular concern was ensuring that the propane and air were properly mixed before entering the combustion chamber and slowing the mixture of gasses down enough so that ignition can occur.

An initial burner design by Maqbool [6](p 30-32) was used as a starting point for the development of the burner used in the experiments reported here. The initial design consisted of two valves that controlled the amount of air and propane entering the burner connected to a long narrow pipe mounted perpendicular to the intake tube (see Figure 3.8). The air and propane were mixed and then entered the combustion area where they were ignited by a spark plug operating at 200 Hz. The heated air then entered the film flow intake pipe and continued into the film plenum.

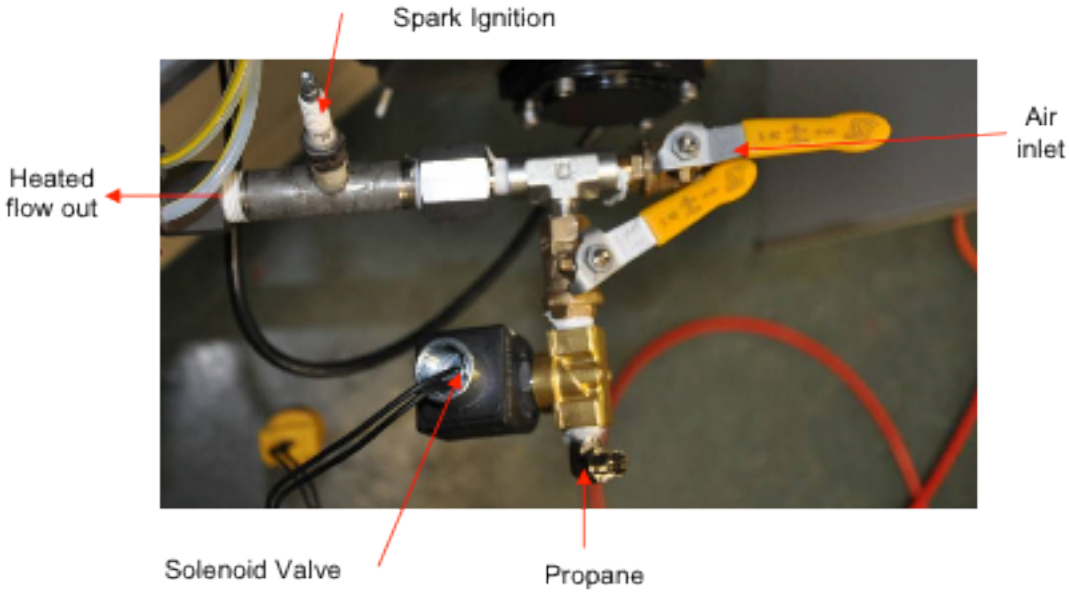

Figure 3.8: Initial burner design {Adapted from Maqbool [6] (2012)}.

Testing showed that this design did not provide enough residence time in the combustion chamber for the flow to ignite consistently. The primary problem was that the diameter of the film-flow burner was too small and caused the flow to pass through the combustion chamber too quickly. In order to slow the fuel-air mixture and provide time for it to ignite, the decision was made to increase the size of the combustion chamber.

The film heater was rebuilt with a 2-inch diameter combustion chamber which discharged directly to the main film flow through a 'T' coupling of the same diameter as the combustion chamber as illustrated in Figure 3.7. This removed the flow obstruction from the smaller mounting nozzle. This configuration was also tested in the lab and produced stable combustion.

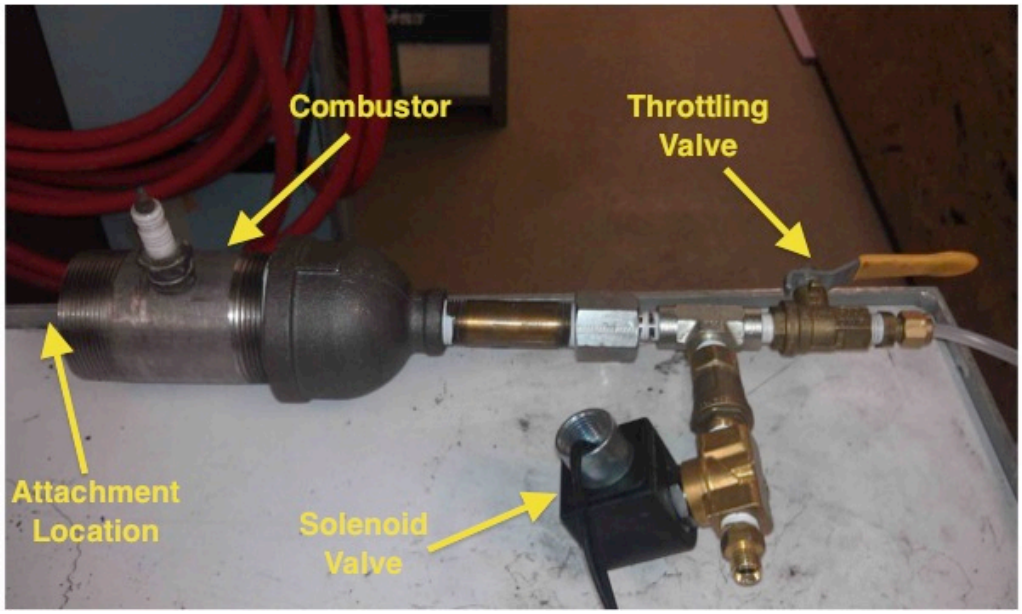

Figure 3.9: Final configuration of film flow heater.

After initial testing in the lab, the film flow heater was attached to the testing apparatus in the wind tunnel. The total temperature of the flow was measured in the film plenum during trial runs. Analysis of this measurement between tests allowed the fuel-air ratio of the burner to be adjusted to provide an approximately 40 K increase in total temperature. This ensured that the heat flux vector always pointed in the appropriate direction (into the main flow).

3.3: Test-Section Redesign

The initial testing phase by Maqbool [6] uncovered several shortcomings in the original experimental design. One of the earliest problems discovered was with the MACOR ® test surface covering the heat flux gauges. This material was only 0.050 inches thick and pressure variations at tunnel startup caused failures at several heat flux gauge locations (see Figure 3.10). These were patched with body filler in order to

reduce disturbances to the flow but the gages were rendered inoperable. This reduced the number of active sensors to 14 on the lower wall and only 5 on the upper wall.

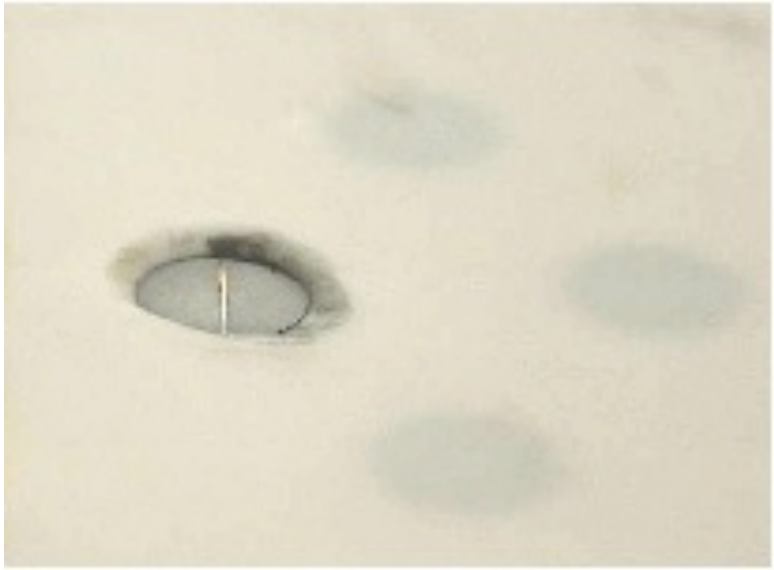

Figure 3.10: Close up of broken MACOR ® surface over a heat flux gauge showing the exposed thermocouple bead and leads. In the initial experiment configuration, this was repaired by covering with Bondo, a body filler to minimize disturbances to the flow.

Later, a catastrophic wall failure completely destroyed the test section's walls (Figure 3.11). Subsequent investigation showed that stress cracks had developed in the MACOR ® plates around key mounting bolts in the lower wall testing surface causing the plates to fail during tunnel startup. When the lower wall broke loose, it traveled across the tunnel destroying the heat flux gages on the upper surface as well. Since the entire test-section needed to be rebuilt, it was decided to take the opportunity to change the design of the walls and the heat flux gages to increase their reliability and strength.

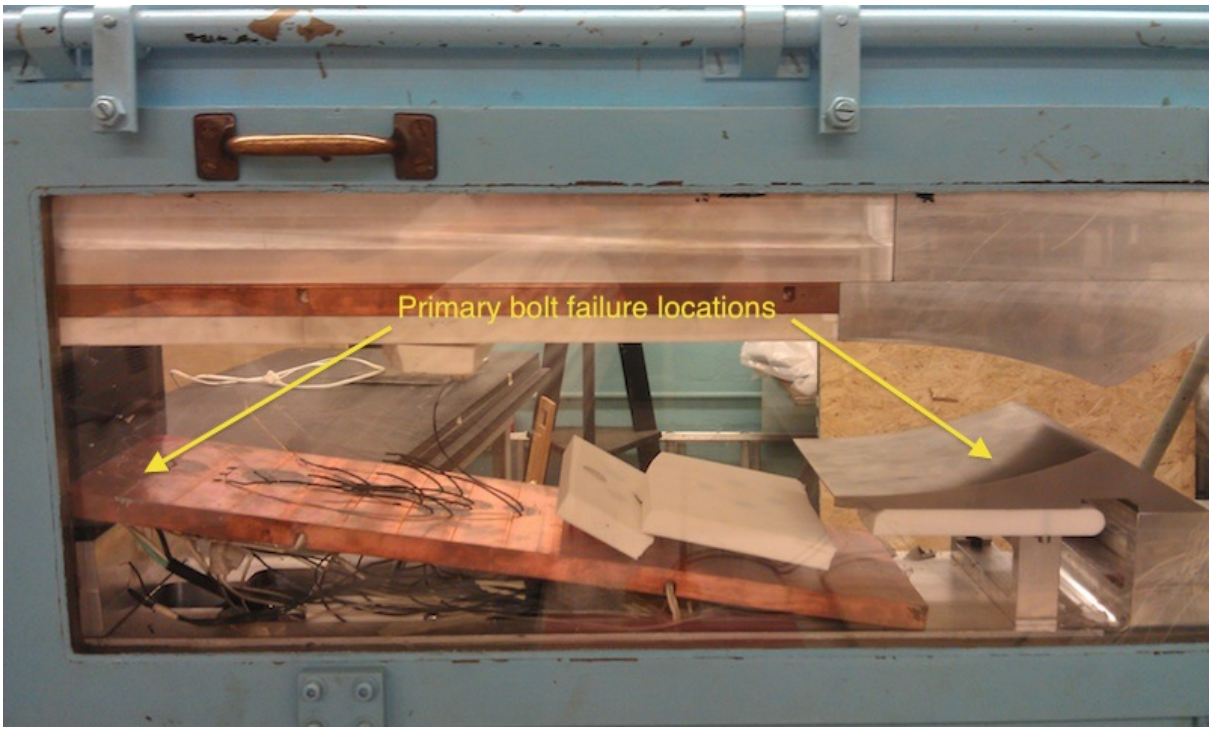

Figure 3.11: Failure of lower testing surfaces. Arrows indicate locations of bolt failures.

Figure 3.12: Photo of bolt failure near the film injection point.

3.3.1: Heat Flux Gauges

Numerous failures of the 0.050 inch MACOR ® membrane above the heat flux gauges prior to the catastrophic wall failure indicated that the membrane needed to be strengthened by increasing its thickness. However, this needed to be done carefully because making it thicker reduces the response of the thermocouple and thus the sensitivity of the gage. As a result, a parametric study was performed of the impact of surface thickness on strength and temperature signal loss.

The maximum shear stress occurs during start up due to the pressure differential between the incoming air and the near-vacuum present inside the tunnel. This pressure difference has a maximum value of 13.62 psi. This value was used to

calculate the maximum stress in the material. The maximum stress in the material over each gage(s) is given by [41](p 488):

$$\sigma_{\max} = \frac{6M_c}{t^2} \tag{3.14}$$

where t is the thickness of the membrane over the gage and M_c is the elastic modulus given by:

$$M_c = \frac{qa^2(1+\nu)}{16} \tag{3.13}$$

This is calculated using the maximum shear stress q, the radius of the bore hole a, and the Poisson ratio of MACOR® ν.

Table 3.3: Maximum stress in heat flux gage membranes at a pressure difference of 13.62 psi.

Thickness (t)	***Max Stress (σ)***
0.050	164.72
0.055	136.13
0.060	114.39
0.075	73.21
0.10	41.18
Units: inches	Units: psi

The modified transient heat conduction equation developed by Maqbool [6] to account for the presence of an initial temperature gradient was used to compute the change in temperature signal resulting from a change in the heat flux gage membrane thickness:

$$T - T_\infty = \left(T_0 - T_\infty - \frac{k}{h}a\right)\left\{erf\left[\frac{x}{2\sqrt{at}}\right] + e^{\frac{hx}{k}+\frac{k^2at}{k^2}} erfc\left[\frac{x}{2\sqrt{at}} + \frac{h}{k}\sqrt{at}\right]\right\} + a\left(\frac{k}{h} + x\right) \tag{3.15}$$

Figure 3.13, shows simulated temperature-time histories associated with different membrane thicknesses. It shows that doubling the thickness of the material from

0.050 inches to 0.10 inches halves (approximately) the temperature drop experienced by the heat flux gauge over the course of the experiment from approximately 6K to 3K.

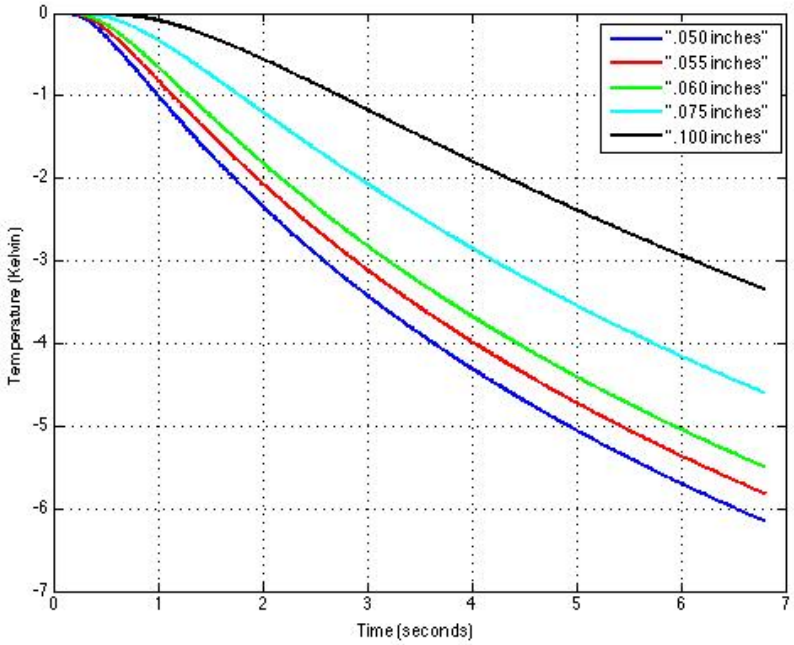

Figure 3.13: Temperature drop at a single heat flux gauge of varying distance from surface for simulated experiment.

A compromise between signal strength and membrane strength was made by plotting the percent increase in membrane strength and the percent reduction in temperature signal as a function of membrane thickness (Figure 3.14 and 3.15). It was decided that increasing the material thickness by 10% to 0.055 inches represented the best compromise. At this thickness, peak stress dropped by 18% while signal loss only decreased by 9%.

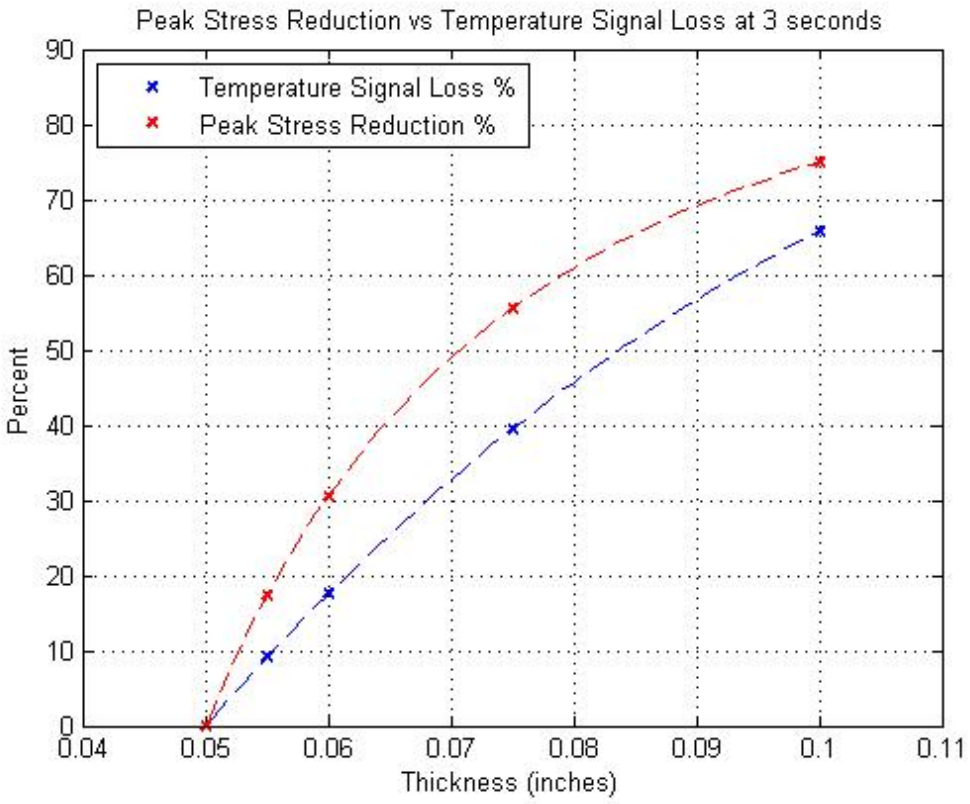

Figure 3.14: Percentage of peak stress reduction and temperature signal loss for increasing material thickness above each heat flux gauge.

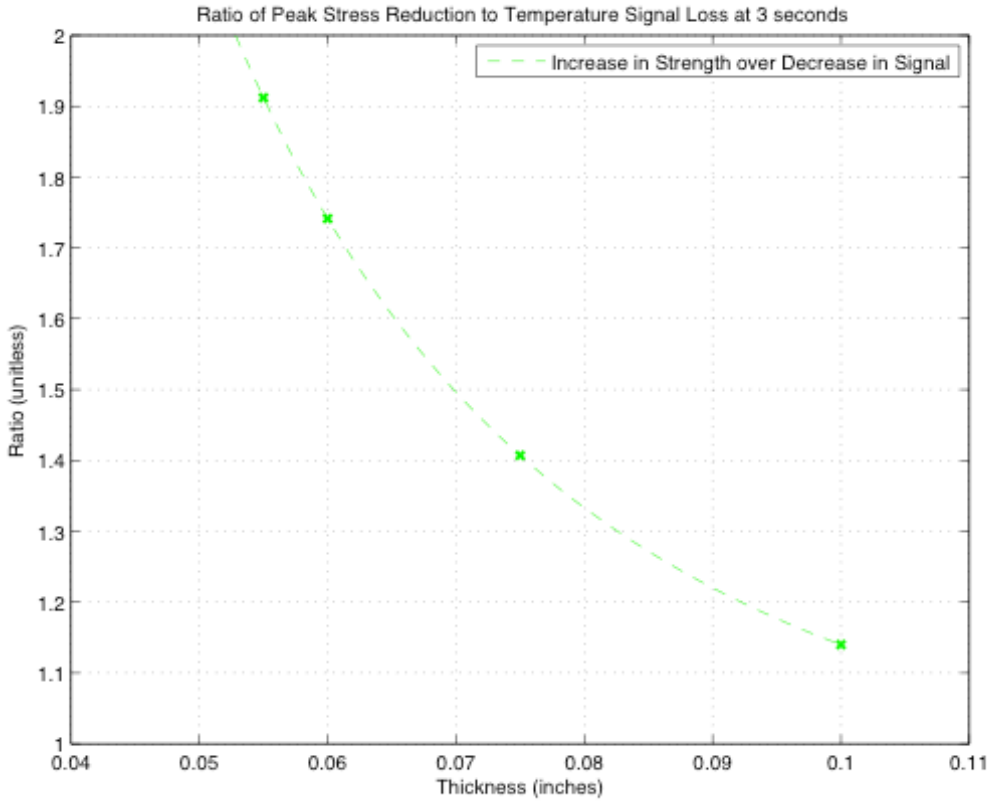

Figure 3.15: Ratio of increase in material strength to decrease in temperature signal plotted versus increasing material thickness.

A radius (or fillet) was also added to the inside of the cylindrical hole holding each gauge. This reduced the stress concentration factor along the corner of the gage bore and further reduced the peak stress by at least a factor of 2 (estimate from *Peterson's Stress Concentration Factors*) [41](p 488)[42]. Due to machining concerns and limitations, this radius was set at 0.125 inches. Increasing the radius beyond this amount would have further reduced the stress, but tool sizing and availability limited the fillet choices. Hole clearance necessitated the use of a filleting tool smaller than 0.2 inches and sizes in between were not available at the time of machining. Adding the radius to the bottom of the bore holes also required that the MACOR® plugs be re-machined with a matching radius (see Figure 3.16).

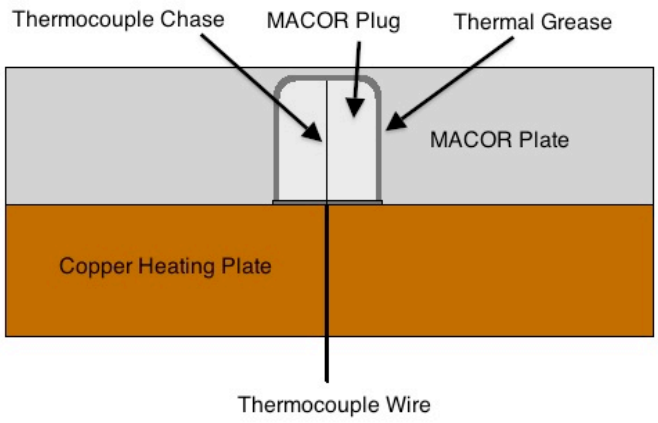

Figure 3.16: Diagram of redesigned bore hole and MACOR® plug insert.

3.3.2: Connections to MACOR

Another area of weakness in the original experiment was the attachment between the MACOR ® test plates and the copper heating plates. The plates were held together using bolts that engaged threads machined into the MACOR ®. These threads tended to disintegrate under heavy loads or repeated use. The new design used Heli-Coil ® inserts to provide a more robust interface between the MACOR and the attachment screws. The inserts reduce stress in the MACOR by distributing the load over a wider area while eliminating steel-MACOR sliding contact as the bolts are installed and removed.

However, installing the Helicoil inserts into the MACOR plates posed its own set of challenges. Unseen stress cracks developed during the initial process of machining the threads for the inserts. The net result was that when a load was applied to fasten the MACOR ® and copper plates together, the surface around some of the inserts failed (see Figure 3.16). Unfortunately, this meant that new MACOR walls had to machined at a significant cost of time and money. In discussions with Ceramic Products Inc., a company who regularly machines MACOR®, it was discovered that

the Helicoil inserts had to be installed in a specific way in order to function robustly. The procedure involved seating the metal insert further into the threads machined in the MACOR® and ensuring that the top of the Helicoil was well below the surface of the test plate. This eased the transfer of stress from the Helicoil to the surface of the MACOR® and alleviated the problem of divots developing around the bolt holes seen in Figure 3.17.

Figure 3.17: Heli-Coil ® insert and failure of surrounding MACOR ® surface.

3.3.3: Lower wall support structure

Another area of concern when examining the failure of the initial experiment was the support of the lower testing surface. In the old design, the entire weight of the lower testing surfaces and its attached copper heating plate was supported by the MACOR ® segments at each end (see Figure 3.18). Additionally, only a single bolt on the upstream section secured the testing plate. The new design includes two additional supports at the upstream end to further secure the lower MACOR wall (see Figure 3.19

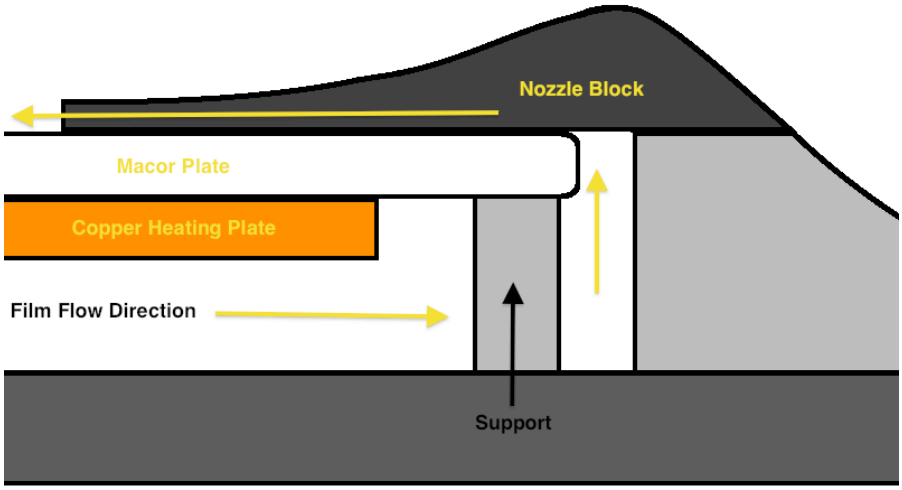

Figure 3.18: Original layout of experiment with only one structural support. Entire weight of experiment is supported by MACOR.

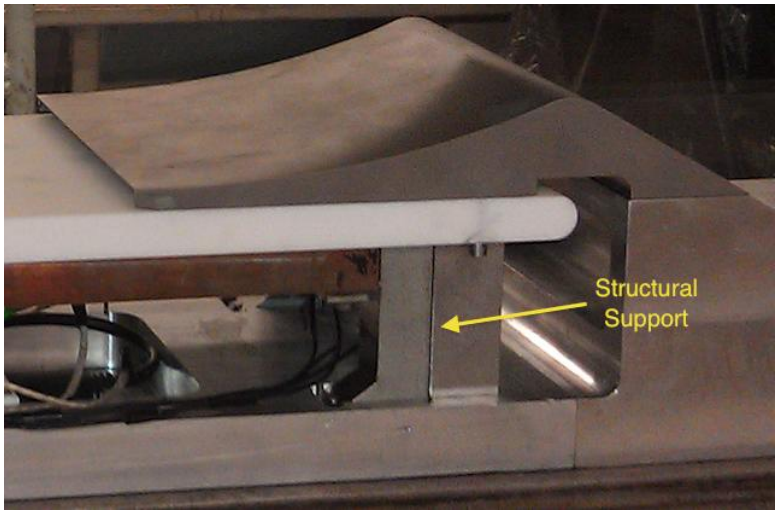

Figure 3.19: Additional structural support added to reduce moment applied to MACOR ® plate.

3.4: Schlieren Imaging and Apparatus

Schlieren imaging was used to visualize density gradients, shockwaves, and shear layers in the test section and especially in the vicinity of the film louver exit. These images provide qualitative insight into the physical processes occurring within the experiment. Schlieren video will be used to study the steady and unsteady aspects of the flow. These images will be interpreted using machine-vision techniques

developed by Smith [14] for extracting quantitative flow structure information from schlieren movies.

The schlieren system used to make all measurements for this experiment is a Z-type configuration (see Figure 3.20). It uses a point light source (provided by an aircraft landing light with a frosted lens behind a 0.25 in diameter aperture), two parabolic mirrors, and a digital camera for the acquisition of images. The point light source is placed at the focal point of the first mirror (M1), which creates a collimated beam that passes through the test section. This beam is reflected by the second mirror (M2) into a digital camera placed at the focal point of the second mirror. The camera's aperture functions as the schlieren stop. This is not ideal but was necessary because of space limitations and the focal lengths of M1 and M2. The camera is a Nikon D90 digital SLR. Color images are recorded at a resolution of 1024 x 580 at a frame rate of 24Hz.

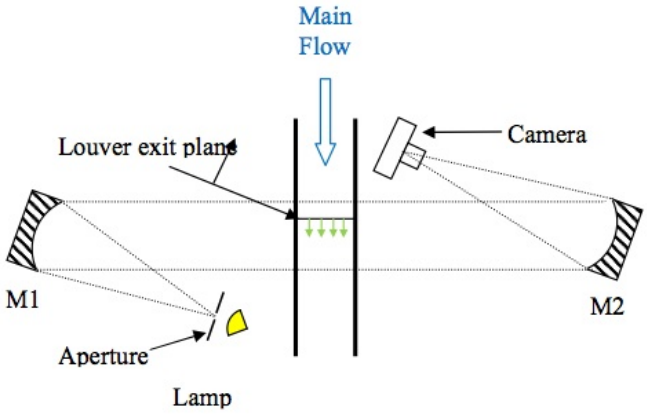

Figure 3.20: Schlieren Apparatus {Adapted from Maqbool [6] (2012)}.

The camera was used in color (not black and white) mode so it is important to understand how the camera produces color images so that we can understand how the essentially grayscale illumination produced by the Schlieren system is captured by a

color imager. The Nikon D90 uses a CMOS sensor covered by a Bayer filter to capture images [43]. The Bayer filter (Figure 3.21) is an array of green, red and blue filters that overlay each pixel of the image sensor. Twice as many green filters are used compared to red and green in order to simulate the response of the human eye which is more sensitive to green light. When photons pass through the filter and are counted by the sensor, the count is associated with the respective color of the Bayer filter. To obtain a full color image, the resulting Bayer pattern image must be interpolated to provide a complete set of green, red and blue values at each point. Note that images can also be stored in a 'raw' format and post-processed outside the camera to obtain a better quality image.

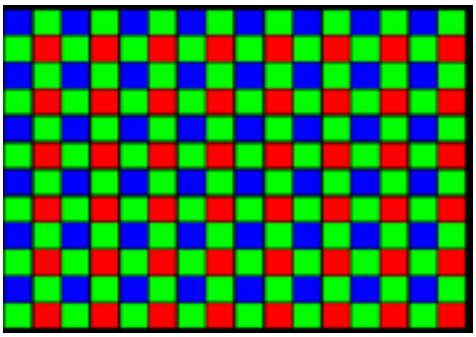

Figure 3.21: Bayer filter pattern. Contains twice as many green filters as red and blue.

The interpolation methods, called demosaicing algorithms, vary between camera manufacturers and come at varying computing costs. These algorithms are proprietary and can vary significantly between manufacturers. The specific method used by the D90 is proprietary to Nikon, so the exact method of interpolation is unknown. However, all of the demosaicing methods have elements in common and share some basic constraints. One important one is that the algorithms be simple and efficient enough to be performed by basic hardware

Each individual pixel on the imaging sensor initially has a red, green, or blue value depending on where it is located on the sensor. These pixels ONLY contain information from one of these spectrums. The Bayer filter corresponds directly to the "color" of the light the pixel beneath it is sensing. The demosaicing algorithms function by using the RGB information from surrounding pixels to form a composite value at each individual pixel being examined (see Figure 3.22). The key to these algorithms is that the individual RGB values from the Bayer pattern image can be used multiple times in order to correctly determine the real world color of surrounding pixels. Many different demosaicing methods exist and are constantly being improved to reduce blurring and improve color interpretation. Several of the most popular methods include: bilinear interpolation, edge directed interpolation, constant-hue-based interpolation, and weighted sum interpolation [44].

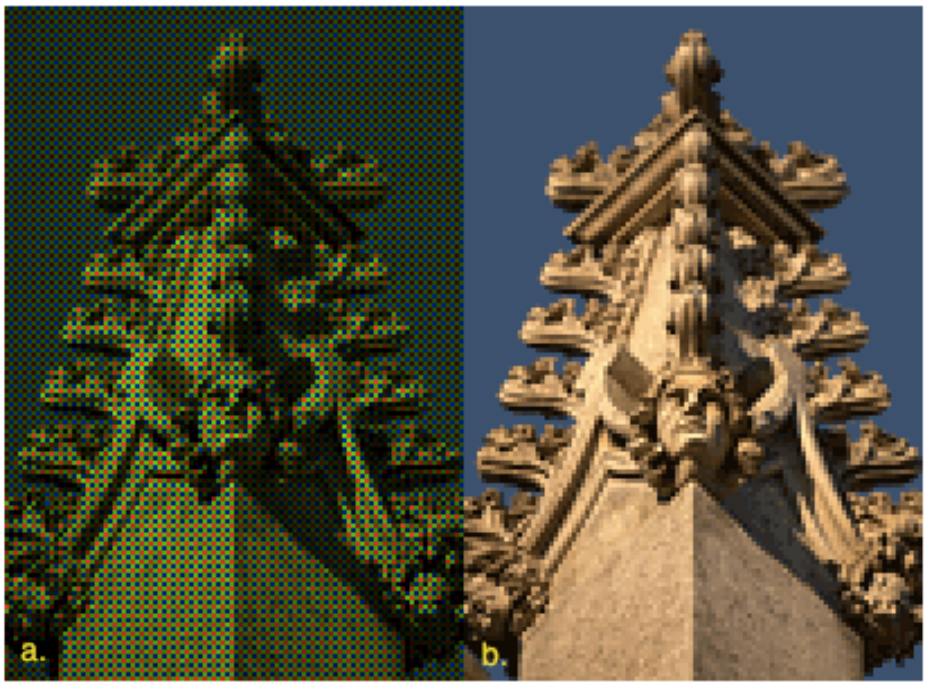

Figure 3.22: Example of: a.) Bayer pattern image b.) Image interpreted from Bayer pattern image by demosaicing algorithm [45].

3.5: Description of CFD Tool

One of the primary objectives of this research was to provide sets of experimental results across a range of test conditions for use in numerical code validation. Numerical simulations of the test cases used in this research have been performed previously by Dellimore [5] using the Loci-CHEM software. NASA has provided additional test cases for validation and comparison.

Loci-CHEM is a NASA computational fluid dynamics tool developed at Mississippi State University (for a full description, refer to Dellimore [5] p. 138–149.). It uses a computationally inexpensive Reynolds Averaged Navier-Stokes (RANS) methodology to predict film cooling effectiveness, skin friction, and thermal and momentum mixing. The Navier-Stokes equations are descretized using a finite volume method and converted to Reynolds averaged form. For compressible flows such as the one being considered in the current study, the equations are mass-weighted (averaged over mass) over time. Menter's two-equation shear stress transport (SST) model [46] is used to close the set of equations.

This set of equations is solved on a generalized grid using the finite volume approach.

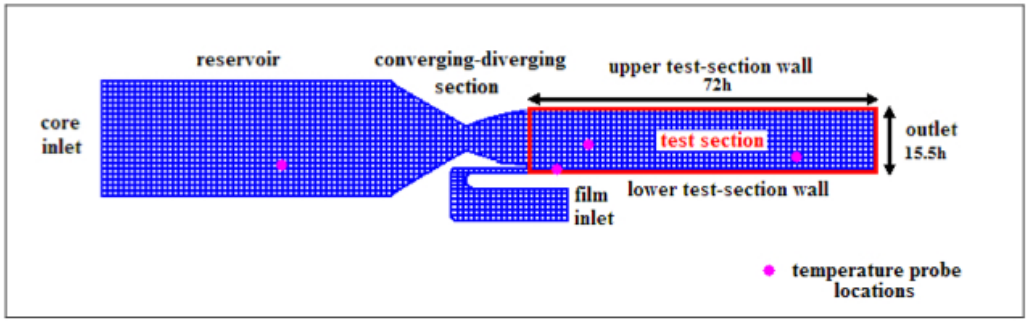

Figure 3.27: Schematic of grid used in numerical simulations of test cases {Adapted from Dellimore [5] (2010)}

Figure 3.27 shows the grid used to compute the solution to all test cases. The computational domain consists of the core stream diffuser inlet, a converging-diverging section, the main test section (lower and upper walls), and the coolant stream inlet manifold. Note that the grid in the figure is for illustrative purposes only and does not show areas of refinement. Much effort was devoted to ensuring that the temperature and velocity gradients were adequately resolved in the viscous sub-layer at the wall boundary and in the shear region between the core and film flows. However, the limiting factor turned out to be the wall heat flux. Isothermal boundary conditions are applied at the test section walls and the heat flux into the wall must be resolved. This required a grid that is an order of magnitude finer than what is needed to resolve temperature and velocity gradients [5] (p 229).

A series of boundary and initial conditions must be provided in order to solve for the flow through the test section. No slip is enforced at all interior walls and all walls are assumed to be isothermal. The wall temperature was set to 340K in the test section (to reflect the wall heating in the experiment) and 300K elsewhere to reflect the temperature of the rest of the tunnel structure which is at ambient conditions in the room. A reflecting boundary condition is specified along the side walls. The flow conditions upstream of the converging diverging section were set to $P_0 = 1\ atm$ and $T_0 = 300\ K$ to reflect ambient conditions in the room. The temperature of the film in the film plenum was set at $T_0 = 340\ K$ to reflect the influence of the film and wall heaters. The outlet flow is assumed to be fully developed so $\partial U/\partial x = 0$, $\partial P/\partial x = 0$, and $\partial T/\partial x = 0$. The pressure in the film plenum depends on the particular test case. The film plenum pressure for Test Cases 1,2 and 3 are $P_0 = 0.08$, $P_0 = 0.12$, and $P_0 =$

0.2 respectively. These initial and boundary conditions fully constrain the problem and allow the flow for all test cases to be solved.

Chapter 4: Schlieren Image Interrogation

4.1: Automated Analysis Techniques

Recent work by Smith [14] has shown how machine vision techniques can be applied to identify flow structures and automatically extract geometric features (like shock angles, etc). Smith applied computer vision techniques to high-speed Schlieren video (10KHz sampling rate) of a double cone structure tested at Mach 14 where the large number of images makes manual interpretation impractical. Using a combination of techniques, primarily Canny edge detection and Hough Transforms, he was able to extract shock angles and separation regions with over 94% accuracy. Smith's work is the first published use of computer vision techniques to accurately identify flow features in high-speed video format. The objective here is to see if Smith's techniques can be used to extract the angles of the film-core interfaces that can be used to determine the shear layer growth rates and to measure the angles associated with shock and expansion structures.

The two computer vision techniques that are vital to the process that Smith developed are Canny edge detection and Hough Transforms. Canny edge detection [25] is a numerical technique that identifies object boundaries in images based on image gradients. It is the preferred method for edge detection because of its low error rate, localization, and the minimization of responses. A low error rate ensures that edges that occur in the image are not missed and that no spurious edges are delivered. The criteria of localization states that the detected edges must be as close as possible to the edges in the real image. Minimization of responses refers to the ability to keep

the same edge from being reported multiple times. This criteria also reduces the detection of edges from image noise. Together these three requirements lead to the development of Canny's edge detection algorithm.

The algorithm follows four basic steps (explained in detail in Table 4.1 in next section). First, small scale noise is suppressed using a Gaussian function (blurring). Second, the gradient magnitude and direction are constructed by convolving the first derivative of the Gaussian function in the X and Y directions with the blurred image. Third, a binary image is formed by a process known as "non-maximum suppression" of the gradient image. This process sets all pixels that are less than the maximum value in the current interrogation window to zero. Fourth, high and low threshold filters are applied as a way to link weak detected edges to strong detected edges. This step functions by first identifying all detected edges that are above the high threshold value. From there, all edges that are connected to edges above the high threshold and between the high and low threshold values themselves are also classified as edges. This method has been demonstrated to be mathematically robust [26] and is used in a variety of image processing applications [27].

The fact that the Canny edge detection algorithm can find edges between objects is useful on its own as a way of highlighting image structures. However, the edge angles and coordinates are necessary to provide quantitative data. These can be extracted automatically using a mathematical function called the Hough transform. The Hough transform uses an accumulator[3] to detect the presence of a line based on a

[3] An accumulator is an array that is used to detect the existence of the line $y = mx+b$. The accumulator's dimension is the same as the number of unknown parameters of the problem being examined. A standard linear problem has two unknown parameters: either (m,b) or (r,θ). For each pixel and its surrounding area, the Hough algorithm determines if there is evidence of a line present and if so, calculates the equation of

set of parameters in polar coordinates. In this space r is the normal distance of the line to the origin and θ is the inclination of the line. Thus the equation of a line is given by equation 2.3.

$$x\cos(\theta) + y\sin(\theta) = r \tag{2.3}$$

The parameters r and θ are used to categorize each line and also are used to differentiate between accumulator bins. The algorithm functions by examining each pixel and its surrounding pixels to determine if there is enough evidence that an edge is present. If there is, it then increases that particular accumulator's bin. Once the entire image is processed, lines can be interpreted by finding the bins with the highest values.

Both techniques are used to process the image data from this experiment. Individual images were extracted from the Schlieren videos frame-by-frame in MATLAB and converted to grayscale. They were then processed using MATLAB's Canny edge-detection algorithm to identify edges (see Figure 4.1 a., b. and c.). The edge maps produced by the Canny algorithm were then processed using the Hough transform to identify line features in images. This method produces endpoint and angle data for all detected lines in the image. The blue lines in Figure 4.1 d. show the lines detected by the computer after being passed through Canny edge detection and the Hough transform. When comparing 4.1 c. and d., it can be seen that not all lines evident in the image are captured by this method. The lines that are visible but are not detected by the computer are not considered "strong" by the vision techniques.

---

that line. It then increases the value of the accumulator bin that that line falls into. There is a bin for each pixel in the photograph, yielding a [2xN] construct where N is the number of pixels.

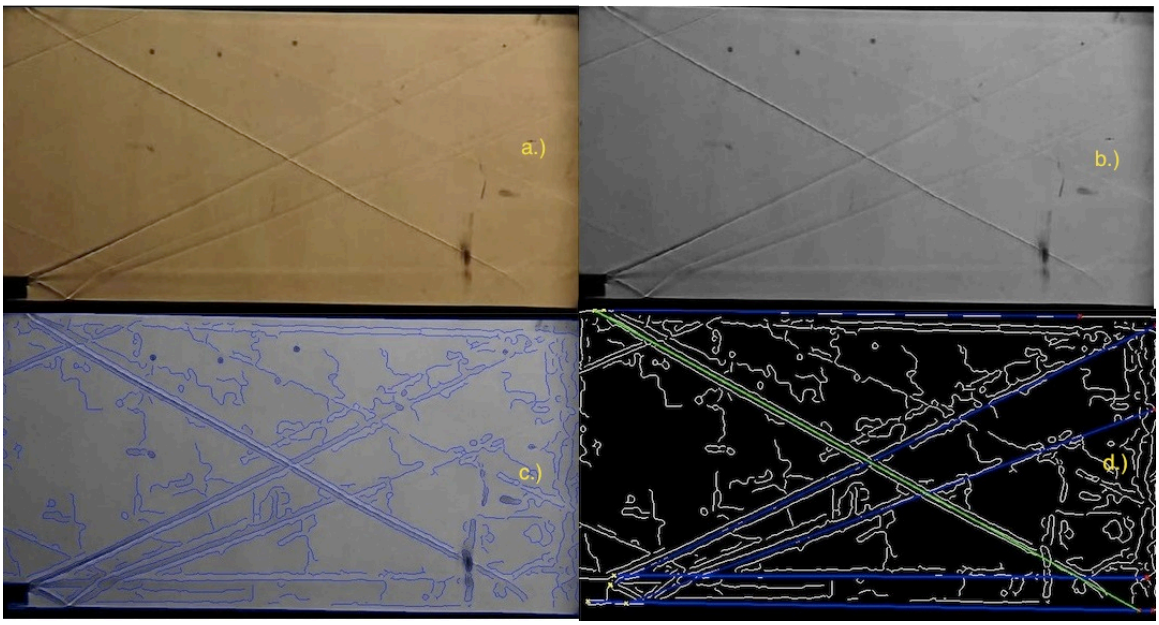

Figure 4.1: a.) Original image taken from schlieren video b.) Grayscale conversion of original image c.) Edge overlay produced by Canny algorithm d.) Edge and line overlay produced by combination of Canny edge detection and Hough transform.

The criteria that are used by the techniques to determine the strength of individual lines can be modified to a certain degree by choosing different threshold values for the Hough transform. However, there is minimal change for these particular sets of images when this threshold value is changed even by a significant amount. It was determined through trial and error that the images in Figure 4.1 represented an "optimal" set of threshold values (see Section 4.2: Determination of Image Processing Parameters).

The main flow features that are being sought, in order of importance, are:

1.) Shear layer between core and film flows.

2.) Shockwave emanating from film injection lip (lip shock).

3.) Shockwaves (Mach waves) emanating from nozzle geometry or imperfections in test surface.

Due to the somewhat poor quality of the schlieren images obtained, not all features were found in each image. A feature that was detected in an individual frame from the video was not necessarily present in every frame. This presented problems in how to correlate the lines detected in each frame and how to compare those lines to their corresponding flow feature. It is important to note that the code itself does not identify the "features", but rather detects the line structures present in the image (see Figure 4.2 for code flow chart). The sets of lines detected in one image must be compared to those detected in the other images to see which of the structures correlate to the same "feature". This was done using a comparison method. The code compares each image and its detected features to a reference image chosen from the middle of the data set. The reference image was automatically chosen by the code to be an image that contains all of the detected line structures. Each of these detected lines was then classified as a "feature" by the code. All other images and the lines detected in them were then compared to this reference image in order to ascertain which features are present in each image. The code is not able to indentify the flow structures themselves, but is able to sort the detected lines by their physical properties, allowing for easy visual identification. Once the calculated data was sorted by its physical properties, it could be used to examine the properties of the flow features throughout the duration of the experiment (i.e. angle fluctuation, shock movement, etc). These results are presented in Chapter 6 and the relevant code can be found in the Appendix.

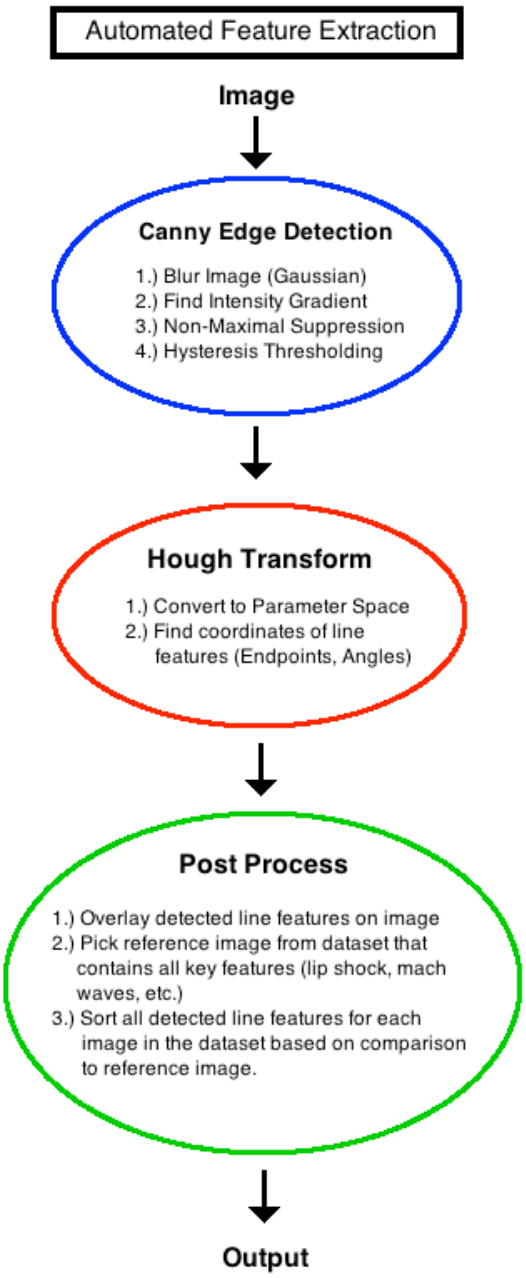

Figure 4.2: Flow chart describing the feature extraction code.

4.2: Determination of Image Processing Parameters

The Canny edge detection algorithm and the Hough Transform algorithm both contain input variables and threshold values that influence their outputs. A set of values was chosen for both functions that produced the least noise and spurious edges

while still preserving the detection of the flow structures. This was done through trial and error by varying each set of variables individually for a reference image and examining the change in output. The main inputs to the Canny edge detection algorithm is the value of σ, which is used to determine the Gaussian function and filter that are used inside the algorithm, and high and low hysteresis threshold values that classify edges and reduce spurious results (see explanation of method in Table 4.1).

Table 4.1: Canny Edge Detection Method

Canny Edge Detection Steps	
1.) Blur image using a Gaussian filter.	a.) 2-D Gaussian Distribution: $$G(x,y) = \frac{1}{2\pi^2} e^{-\frac{x^2+y^2}{2\sigma^2}}$$ b.) Calculate 5x5 Gaussian Kernel using (x,y) locations in matrix and 2-D Gaussian formula: $$\begin{bmatrix} (-2,2) & (-1,2) & (0,2) & (1,2) & (2,2) \\ (-2,1) & (-1,1) & (0,1) & (1,1) & (2,1) \\ (-2,0) & (-1,0) & (0,0) & (1,0) & (2,0) \\ (-2,-1) & (-1,-1) & (0,-1) & (1,-1) & (2,-1) \\ (-2,-2) & (-1,-2) & (0,-2) & (1,-2) & (2,-2) \end{bmatrix}$$ c.) Convolve 5x5 Gaussian Kernel with image.
2.) Find the intensity gradient of the image.	a.) Calculate the vertical and horizontal derivatives of the blurred image, G_x and G_y. b.) Calculate the edge gradient and direction: $$G = \sqrt{G_x^2 + G_y^2}$$ $$\Theta = \arctan(G_y, G_x)$$ c.) Edge direction is rounded to one of 4 angles: 0°, 45°, 90°, 135°

3.) Non-maxium suppression of gradient image.	a.) Image gradients are examined to determine if the gradient magnitude assumes a local maximum in the gradient direction. There are 4 possible variations: i. For 0°: The pixel is considered to be an edge if it's gradient magnitude is greater than the magnitudes directly above and below the pixel. ii. For 45°: The pixel is considered to be an edge if it's gradient magnitude is greater than the magnitudes above and left of the pixel and below and right of the pixel. iii. For 90°: The pixel on considered to be an edge if it's gradient magnitude is greater than the magnitudes directly to the left and right of the pixel. iv. For 135°: The pixel is considered to be an edge if it's gradient magnitude is greater than the magnitudes above and right of the pixel and below and left of the pixel. b.) The output of the previous step produces an edge map in the form of a binary image. Pixels that correspond to edges are stored as a value between 0 and 1 (depending on the gradient magnitude). Those that do not correspond to edges are stored as 'zeroes' in the binary image.
4.) Hysteresis thresholding.	a.) A final step to reduce spurious edges is to use two threshold values (T_1, T_2) to classify the edges. This requires three steps: i. Any pixel value in the binary image that is greater than the T_1 threshold is marked as an edge. ii. Any pixel value in the binary image that is between T_1 and T_2 AND is connected to a pixel above the T_1 threshold is considered to be an edge. iii. Any pixel value in the binary image

	that is less than the T_2 threshold OR is between T_1 and T_2 and not connected to a pixel greater than T_1 is replaced with a 'zero'. b.) This step further reduces small-scale noise and useless edges while preserving data attached to 'strong' edges. Common threshold values are $T_1 = 0.3$ and $T_2 = 0.1$.

Proper selection of σ for the Canny operator is essential in order to detect the edges in an image without including extra noise. This is particularly important for Schlieren images, as many flow structures are faint and change over time. In order to properly select the value of σ, a reference image was manually interrogated to determine the present structures. The value of σ was varied in order to ascertain its effect upon the reference image. A value was chosen that allowed the detection of the relevant flow features while still suppressing noise. The default value of $\sigma = 2$ proved to be the best choice for detecting the most flow features in the Schlieren images (see Figure 4.3). Reducing the value of σ increased the noise (visible as curling and wavy lines in between structures in Figure 4.3) present in the images and did not assist in the detection of flow features. Increasing the value of σ decreased the noise present in the images, but also reduced the number of detected flow features. Changing the hysteresis threshold values proved to have little effect on the images. The default values of $T_1 = 0.3$ and $T_2 = 0.1$ were used.

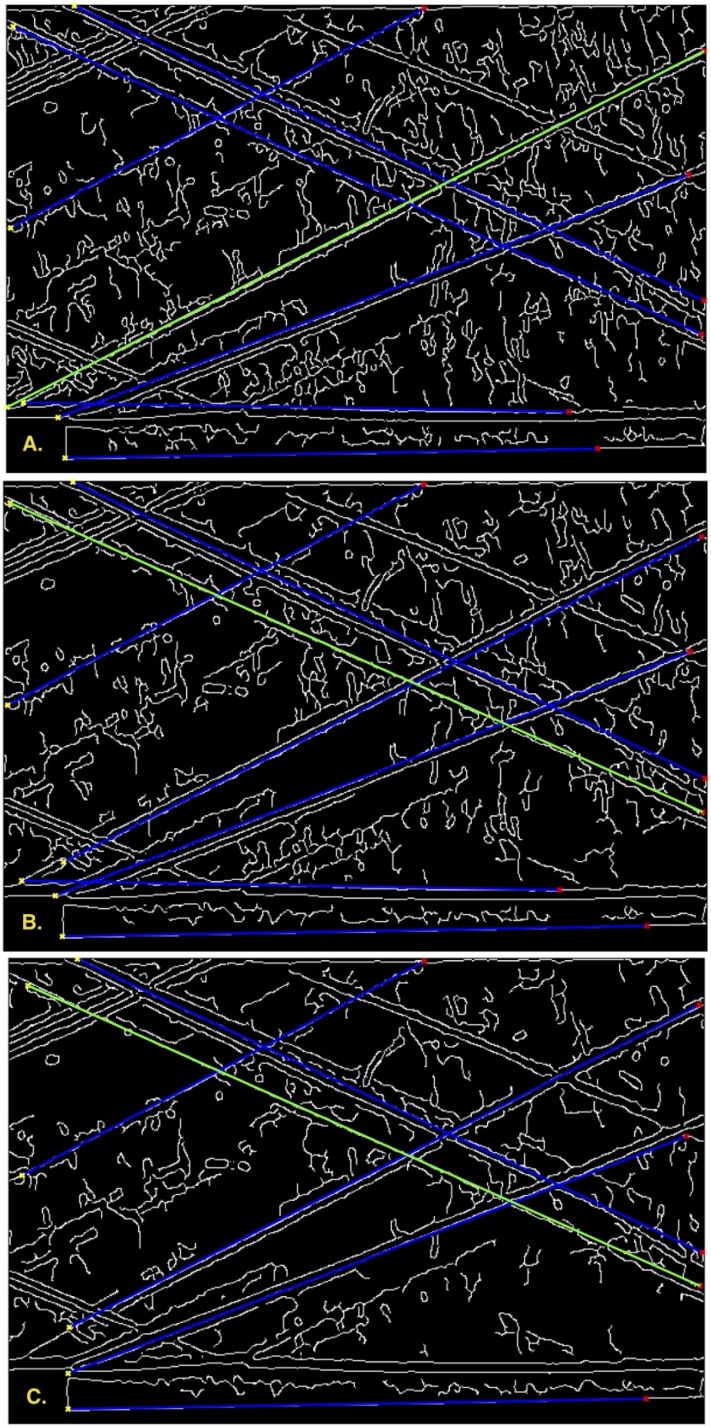

Figure 4.3: Schlieren image after processing with flow feature detection code. A.) Results with Canny edge detector set to $\sigma = 1.75$. B.) Results with Canny edge detector set to $\sigma = 2$. C.) Results with Canny edge detector set to $\sigma = 2.25$. Increasing the value of σ decreases noise but also decreases the number of flow features detected. A value of $\sigma = 2$ proved to be the best tradeoff.

The Hough Transform algorithm uses the output of the Canny edge detector to compute angles and end points for straight lines. It uses two input variables in order to determine what features in the Canny image qualify as lines. The first of these is *MinLength*. This specifies how long an edge needs to be before it is considered a line. If a detected edge is a straight line but is under this distance, it is discarded. The second variable, *FillGap*, is used to determine if two separate line segments with the same angle and along the same linear path should be linked together to form a single line. Any separate line segments that meet these criteria and are closer than the distance specified by *FillGap* are assumed to be a part of the same feature.

The Schlieren images specific to this experiment contain faint, long straight lines that, presumably, indicate Mach waves. Due to the low quality of the images obtained, it was necessary to set the *MinLength* variable low and the *FillGap* variable high. This allowed for the most consistent determination of line features within each set of images. Changing these values in the opposite manner decreased the number of line features that were detected and increased the segmentation of the lines that were detected (i.e. smaller lines along the same linear path). The values were chosen so that they produced long, continuous lines along the flow features that were determined manually.

The default value for *MinLength* is 40. This value allowed for the detection of all of the flow structures that were manually located in the flow, but did not produce the correct end points (see Figure 4.4). Yellow and red X's in the output images denote the start and end points respectively. Blue lines indicate the detected edges, with the green line indicating the longest continuous feature. The blue line at the bottom of

each image corresponds with the lower wall of the experiment. As the value of *MinLength* was decreased, more line segments were detected along a linear path corresponding to the flow features that were identified manually. In Figure 4.4a., only short sections of the boundary layer and lip shock are detected by the code. Further decreasing the value of *MinLength* allows the code to detect more of the line segments along the same linear features (Figure 4.4c.). A value of *MinLength = 1* was used (Figure 4.4c.) in order to detect the maximum number of linear constructs in the images. It was not observed that this produced any incorrect or spurious results.

The *FillGap* variable is used to determine if line segments that occur along the same linear path and angle should be linked. If the gap between two segments is less than what is specified for *FillGap*, the algorithm links them into one line. The default value of 20 for *FillGap* did not link many of the segments that occurred along the same linear path when used with the previously chosen value of *MinLength* (Figure 4.5a.). In order to successfully link lines from the same flow feature, the variable was increased to 50 (Figure 4.5b). This linked many of the smaller segments along the flow features, but several still exhibited breakages. A value of 200 (Figure 4.5c.) proved to be adequate to link all of the line segments along all flow features. Increases beyond this value had no notable effect.

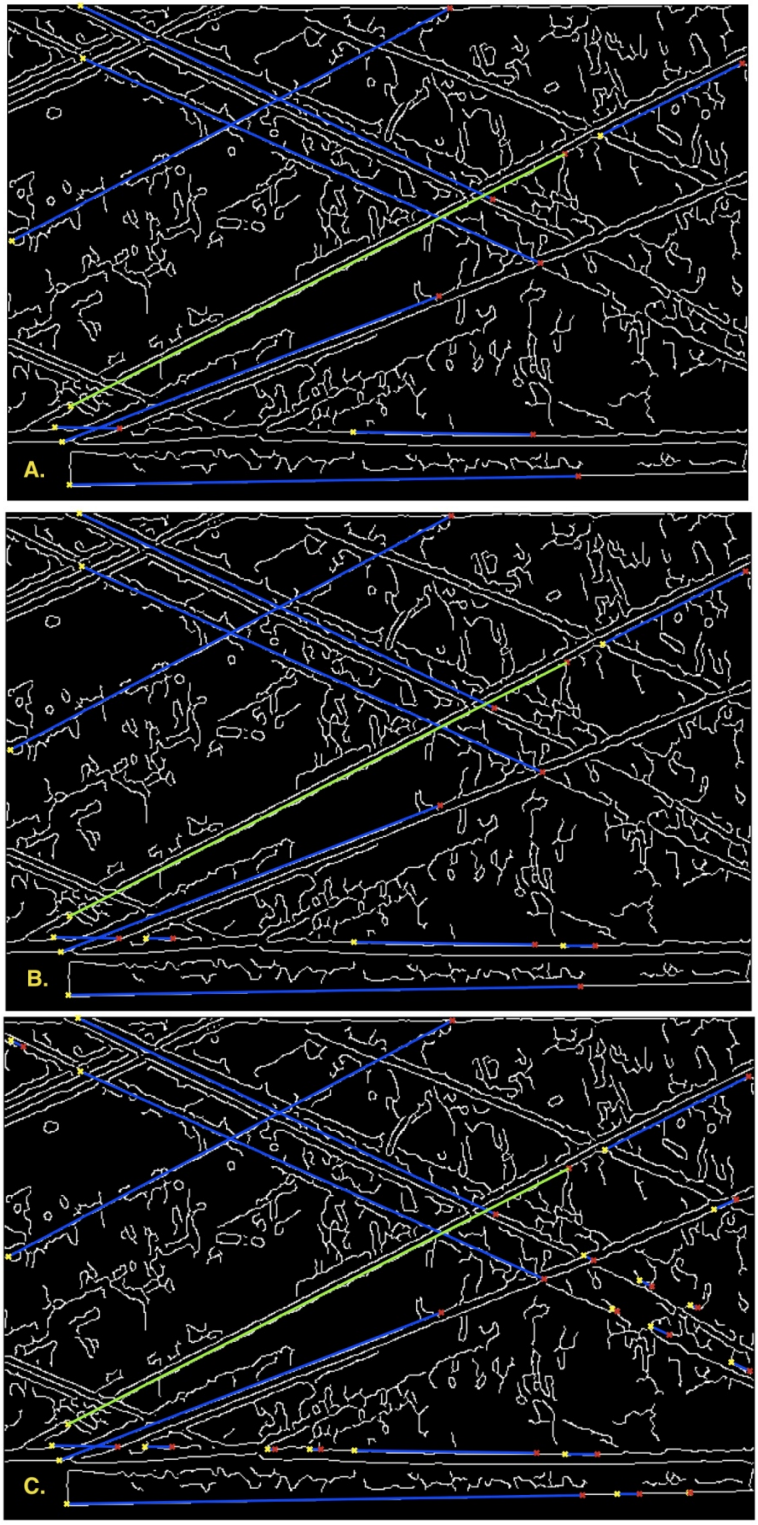

Figure 4.4: Schlieren image after processing with flow feature detection code. A.) Results with *MinLength* variable set to 40. B.) Results with *MinLength* variable set to 20. C.) Results with *MinLength* variable set to 1. Decreasing the value of *MinLength* improved the detection of lines in unclear areas of the image. A value of *MinLength =1* produced the best results.

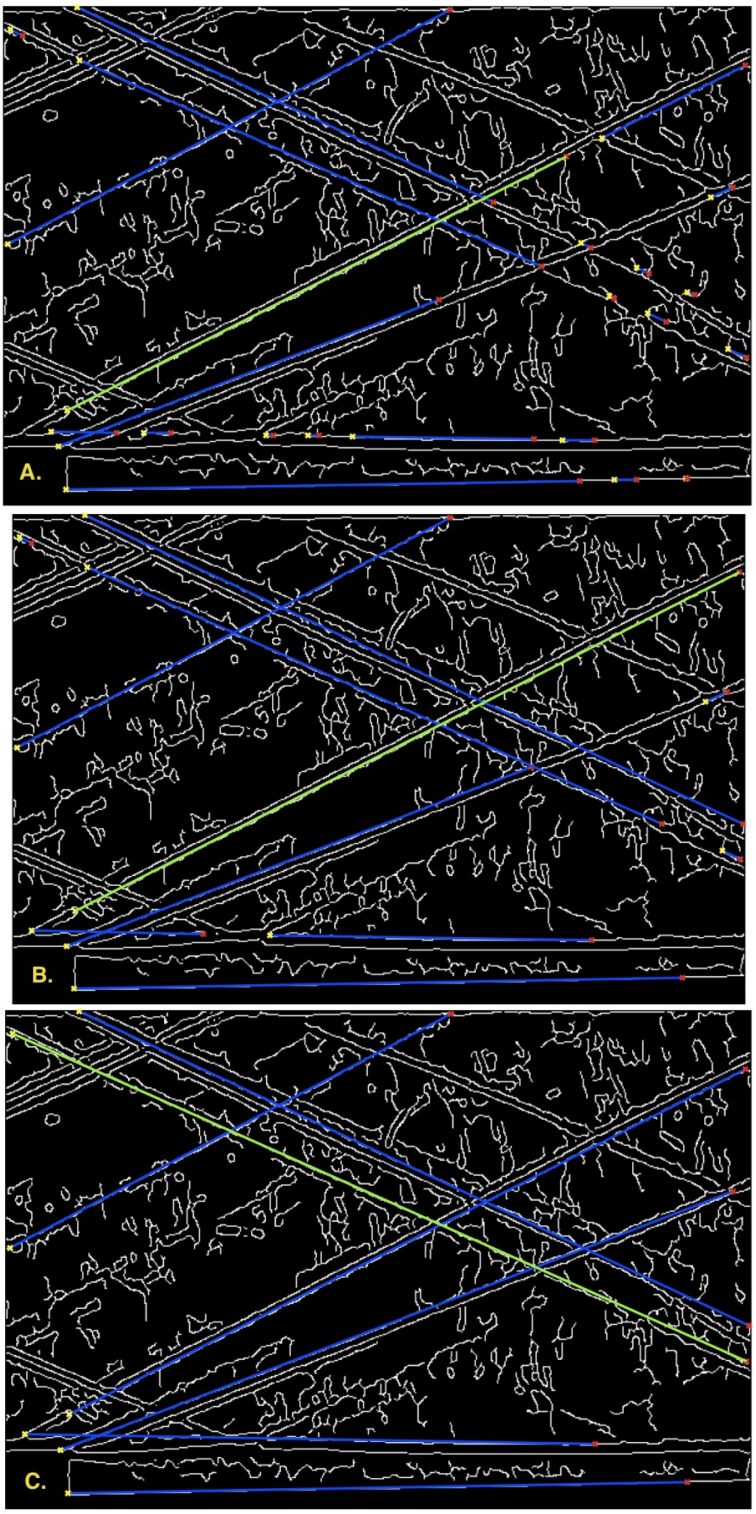

Figure 4.5: Schlieren image after processing with flow feature detection code. A.) Results with *FillGap* variable set to 20. B.) Results with *FillGap* variable set to 50. C.) Results with *FillGap* variable set to 200. Increasing the value of *FillGap* improved the grouping of detected lines along the same path into a single feature. A value of *FillGap = 200* produced the best results.

Chapter 5: Uncertainty Analysis and Data Processing Methods

5.1: Summary of Measurements

A great quantity of data was acquired for this experiment in several different formats. Temperature data was acquired through the use of thermocouples embedded in the test surface. The temperature-time histories from these probes were used to compute the heat flux at specific locations. Pressure transducers connected to small pressure taps throughout the test section provide Mach number and pressure information at key locations. These physical quantities and how they are acquired were explained thoroughly in Section 3.1.3.

In addition to making physical measurements throughout the test section, optical measurements were made through the use of schlieren videos. These were acquired using the z-type schlieren setup described in Section 3.4. The videos were processed in MATLAB using the machine vision techniques and code outlined in Chapter 4. The line features that were obtained from the code output were compared to a reference schlieren image from each test case and interpreted by hand. This was required in order to associate the calculated results with real flow phenomena. A specific set of flow features were sought in each test case. These features were chosen based on several criteria:

1.) Physical importance to wall heat flux distribution.

2.) Presence of flow feature in majority of test cases.

3.) Consistency of flow feature in relation to injection conditions.

For the subsonic film injection cases (Test Cases 0,1, and 2), five flow features were identified for examination (See Figure 5.1). The first of these features is the shear layer between the core and film flows. The expansion of this shear layer directly correlates to the wall heat flux. The shear layer is present in all test cases but is heavily dependent upon film injection conditions. The second flow feature of interest is the shockwave emanating from the film injection lip. This is a strong shockwave that changes angle depending on film injection conditions. The point at which it contacts the upper wall greatly influences heat flux. The other flow features that were identified for study originate from defects in the test surfaces or nozzle geometry and are present in every test case. They change little with film injection conditions and originate in the core flow. Each contacts the test surfaces or shear layer at a point in the test section and causes a fluctuation in heat flux.

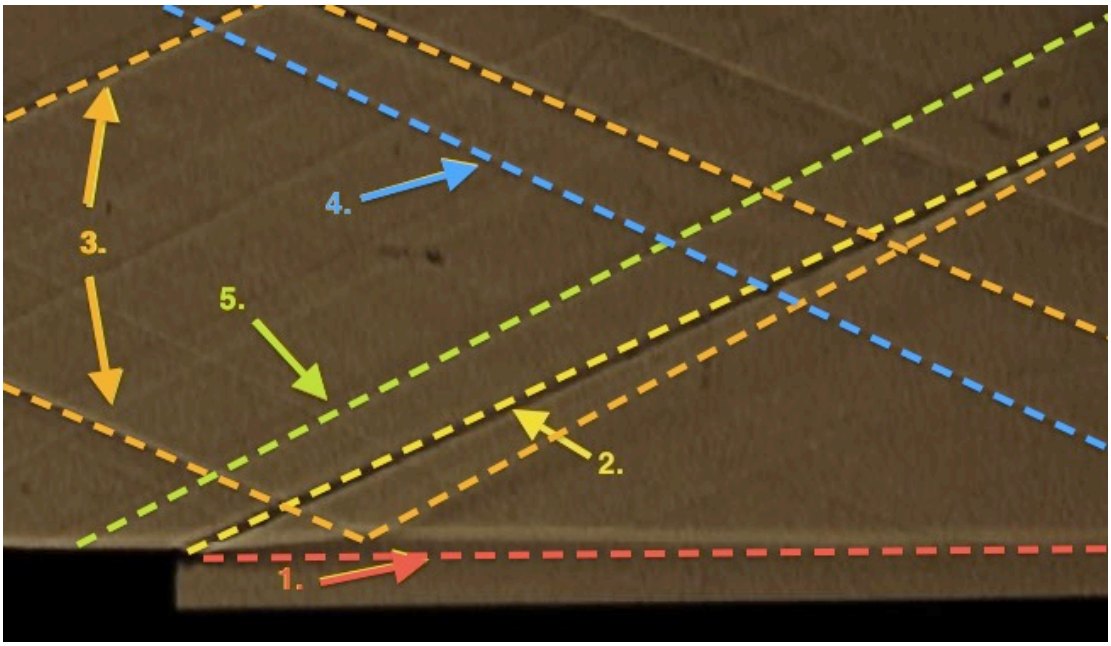

Figure 5.1: Sample schlieren image for subsonic injection cases (Test Cases 0, 1, and 2) showing important flow features. These are: 1.) Shear layer 2.) Shock emanating from injection lip 3.) Shock waves from nozzle geometry 4.) Shock wave emanating from start of upper wall test section 5.) Shock wave emanating from end of nozzle.

The supersonic film injection case (Test Case 3) has another flow feature of interest in addition to the five already identified in the previous test cases (see Figure 5.2). The expansion fan that emanates from the film injection lip reflects off the experiment test surface as a shockwave and passes through the shear layer. In addition to affecting the heat flux at the wall contact point, it also changes angle after it passes through the shear layer and goes on to contact the upper wall. This feature is only present during supersonic injection and occurs at a fixed angle for this test case.

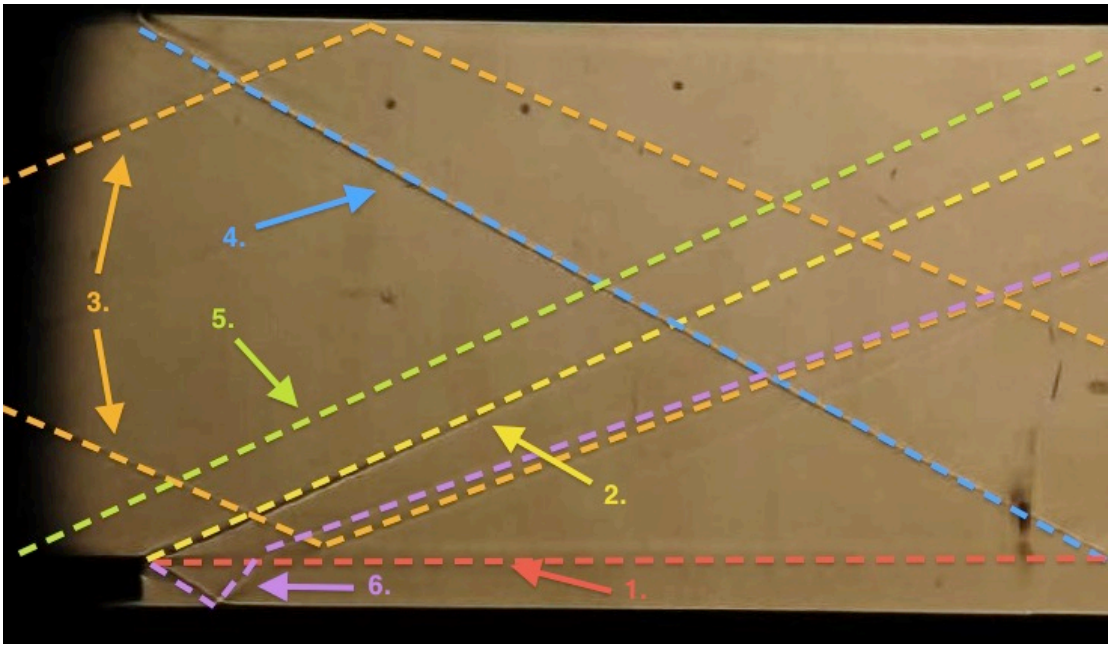

Figure 5.2: Sample schlieren image for Test Case 3 showing important flow features. These are: 1.) Shear layer 2.) Shock emanating from injection lip 3.) Shock waves from nozzle geometry 4.) Shock wave emanating from start of upper wall test section 5.) Shock wave emanating from end of nozzle 6.) Expansion fan and reflected shock emanating from film injection lip.

5.2: Uncertainty Analysis

The systematic and random components of uncertainty have been calculated for use with the heat flux results. The systematic component of the error is associated with inaccuracies inherent to the experimental system. For this experiment, systematic errors in the heat flux measurements can arise from four sources: the

temperature readings themselves, machining tolerances, the MACOR® thermal properties, and the numerical curve-fitting process that determines heat flux (see Table 5.1). The assumption is made that the uncertainty at the thermocouple is equal to a maximum of +/- 0.5 K even though the thermocouple is located below the testing surface. The response time of the testing surface is much slower than that of the thermocouple.

Table 5.1: Sources of Systematic Uncertainty

Source of Error	Error Margin
Uncertainty in temperature readings	+/- 0.5 K
Machining tolerances	+/- 0.005 in.
Uncertainty in MACOR® thermal properties	+/- 3%
Heat flux numerical curve-fitting process	+/- 3%

The systematic component of the error was calculated and outlined in detail by Maqbool [6](p 62-65). The following equations were used to calculate the uncertainty:

$$V\left(P_1,P_2...P_N\right)=\sqrt{\sum_{i=1}^{N}\left(\theta_i,\delta_i\right)^2} \tag{5.1}$$

$$\theta_i=\frac{\Delta V}{\Delta P_i} \tag{5.2}$$

The systematic error of a calculated quantity, V, is a function of multiple parameters ($P_1,P_2,...P_N$). The variable δ_i is the uncertainty in the i^{th} parameter and the term ($\theta_i\delta_i$) is the uncertainty in V due to the i^{th} parameter.

The uncertainty in V due to the i^{th} parameter, ($\theta_i\delta_i$), was calculated numerically by observing the effect of changing the temperature, sensor location, and thermal diffusivity by their maximum error margin in the heat flux code. The curve fitting

process itself induced approximately a 3% error. Combining all four sources yielded a maximum systematic error of 9.5% for all heat flux measurements.

The random component of the uncertainty depends on the experiment-to-experiment variability and decreases as the number of experiments increases. These errors can be minimized by running a large number of experiments at each test conditions. A minimum of 10 experiments were performed at each test condition (except Test Case 1H due to difficulties with film heater) in an effort to reduce the random error. The random error was computed using standard uncertainty analysis methods [48]. All quantities were computed at each *x/s* location for every test case. The first quantity necessary for computing random error is the sample mean value:

$$\bar{x} = \frac{1}{N}\sum_{j=1}^{N} Q_j \tag{5.3}$$

The sample mean value at a given *x/s* location is the averaged heat flux across all experiments performed for a single test case. These values are then used to compute the sample variance, standard deviation, and standard deviation of means:

$$S_x^2 = \frac{1}{(N-1)}\sum_{j=1}^{N}\left(Q_j - \bar{x}\right)^2 \tag{5.4}$$

$$S_x = \sqrt{S_x^2} \tag{5.5}$$

$$S_{\bar{x}} = \frac{S_x}{\sqrt{N}} \tag{5.6}$$

Once the standard deviation of means has been obtained, t-distribution values can be used to directly calculate the random error at each *x/s* location:

$$err_{random} = S_{\bar{x}} \times t_N \tag{5.7}$$

The t-distribution value t_N is dependent upon the number of experiments and the confidence interval required. Values corresponding to a confidence interval of 97.5% were used for the uncertainty analysis.

5.3: Heat Flux and CFD Comparison

Average heated and unheated test results are reported together along with CFD simulation data from Dellimore [5] and NASA (where available) so that comparisons can be made. Average heat flux results are computed using equation 5.3. The comparison between experiment and CFD is made quantitative by computing the difference between the heat flux predicted by CFD and the average of the experimentally determined values at each axial station *i* (corresponding to x/s) and normalizing by the experimental value:

$$\Omega_i = \frac{\left(Q_{CFD_i} - Q_{EX_i}\right)}{Q_{EX_i}} \tag{5.8}$$

Averaging over the all collected datasets and entire x/s range provides a means for measuring how well the CFD predicts film cooling performance:

$$\overline{\Omega} = \frac{1}{N}\sum_{i=1}^{N}\Omega_i \tag{5.9}$$

$$\Omega = \frac{1}{M}\sum_{i=1}^{M}\overline{\Omega} \tag{5.10}$$

where N is the number of experiments and M is the number of *x/s* locations. This provides an average Ω_{bar} value at each *x/s* location and an average Ω value for each test case. This method is used to compare all CFD and experimental data. Results from equations 5.8 -5.10 are used to assess the accuracy of the CFD and the

variability between datasets. It's primary use is to show the *x/s* locations where the experimental and numerical results differ greatly.

$$RMS_i = \sqrt{\frac{1}{N^2}\left(\Omega_i^2\right)} \tag{5.10}$$

The RMS average (equation 5.10) of the numerical and experimental results is also computed.

With the numerical data obtained from the automated computer analysis of schlieren images, a quantitative comparison to density gradient images generated from CFD is possible. This was done in a similar manner to equation 5.8 in order to compare shockwave angles:

$$\theta = \frac{\left(\theta_{CFD} - \theta_{EX}\right)}{\theta_{EX}} \tag{5.11}$$

This allows for a better estimation of the performance of the CFD analysis when taken in conjunction with the results of equation 5.8.

5.4: Variability of Results

Several of the methods listed in the previous sections are used to quantify the variability of the results. The primary measure used to do this is the random component of the uncertainty. When viewed against the axial location (*x/s*), it provides a good metric to investigate if enough datasets have been acquired and if there are any areas in the flow that fluctuate a great deal. These results are presented in chapter 6 for each test case. Figure 5.3 shows a sample plot of random error vs. *x/s* for Test Case 0.

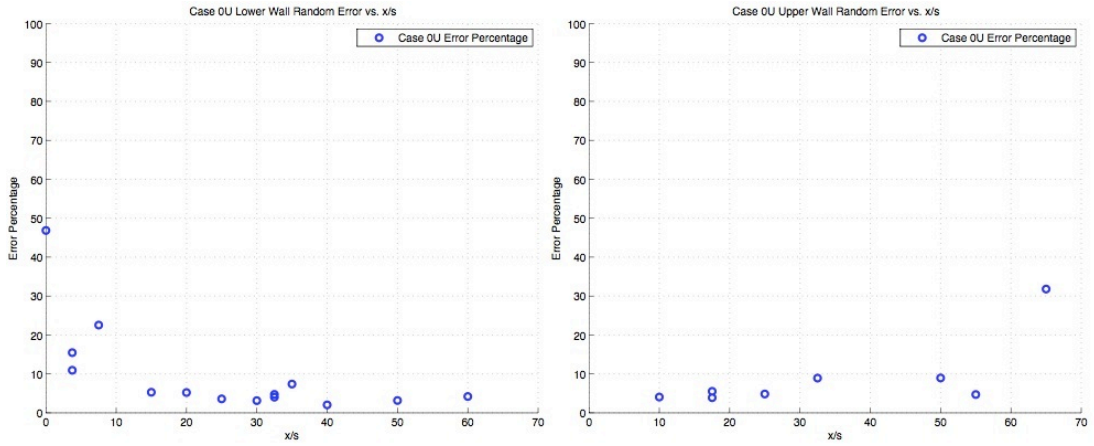

Figure 5.3: Random error vs. x/s location for Test Case 0. Left: Lower wall. Right: Upper wall.

The results of this analysis show that the majority of the test section exhibits a random uncertainty component between 0 - 10 %. For the lower wall, the first 15 slot heights exhibit a larger amount of variability. This appears to be worse for the lower film mach numbers. This problem is compounded by the fact that the heat fluxes in this area are small (order of magnitude less) in comparison to those beyond $x/s > 15$. A change of a 100 W/m^2 between test runs results in a large fluctuation of the random uncertainty. The upper wall shows similar results to the lower, with the majority of the x/s locations exhibiting a random error between 0 - 10 %. There does not appear to be a single area that has a larger variability, but there does appear to be some fluctuation at $x/s = 32.5$ and 65. This is due to the impingement of shockwaves on the upper wall (explained in Chapter 6). Overall, the majority of the test section (both upper and lower wall) has a random uncertainty below 10 %. This indicates that an adequate number of datasets has been acquired.

The Ω variables defined in equations 5.8, 5.9, and 5.10 are another way to measure variability. When Ω_i is plotted against axial location, the deviation between experiment values and CFD results from individual datasets can be viewed. These

results are also presented in chapter 6. Figure 5.4 shows a sample plot of Ω_i vs. axial location for Test Case 0.

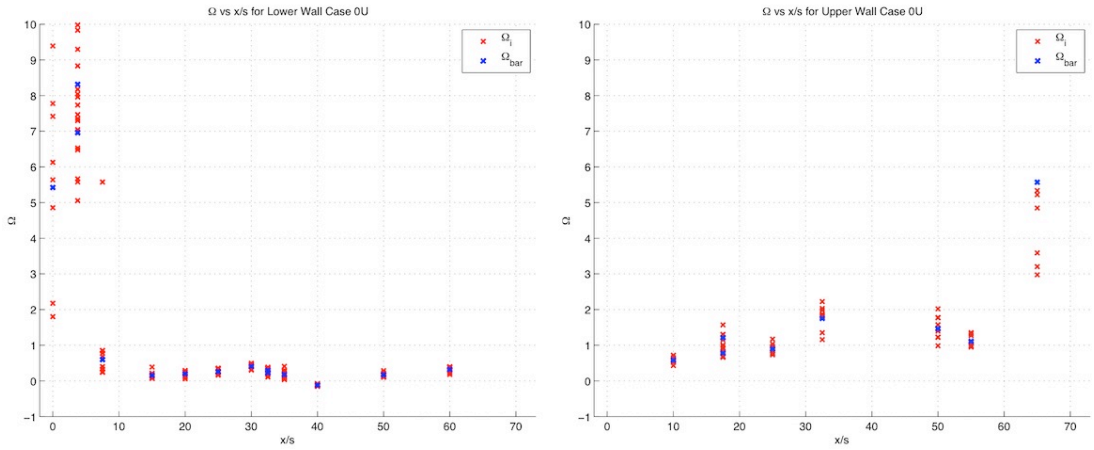

Figure 5.4: Ω_i vs. x/s location for Test Case 0. Left: Lower wall. Right: Upper wall.

The plots of Ω show similar results to the random uncertainty analysis. The majority of the variability between datasets on the lower wall occurs between $0 < x/s < 15$. For the region beyond $x/s = 15$, the Ω values are all closely grouped. This signifies a very small amount of change between datasets. For the unheated film injection cases, the CFD over-predicts the heat flux throughout the test section. The opposite is true for the heated film injection cases, with the experimental heat flux greater than that predicted by CFD. The upper wall also shows similar results to the random error analysis. There is a large variation in Ω at $x/s = 65$ and a lesser but still significant one at $x/s = 32.5$. The individual Ω values are grouped less closely than on the lower wall, but still exhibit small spreads. The majority of the test section (both upper and lower wall) has Ω values between $-1 < \Omega < 1$. The areas with the largest variability are the first 15 slot heights on the lower wall and around $x/s = 65$ on the upper wall.

Chapter 6: Results

Results are reported for each individual test case along with CFD data where available (see Table 6.1). The individual test cases are further categorized by upper and lower wall and the heating of the film. For example, Test Case 1UH refers to upper wall data from Test Case 1 with heated film injection. This naming convention is used to refer to all test cases. CFD data is also reported in this manner with an additional identifier to indicate whether the results were obtained from NASA or the University of Maryland.

Table 6.1: Labeling conventions and test conditions for all Test Cases. Small x's indicate number of experiments.

	Experiment and CFD Condition Summary					
	Type	**Heated/ Unheated**	**Test Case 0**	**Test Case 1**	**Test Case 2**	**Test Case 3**
			$M_f = 0$	$M_f = 0.5$	$M_f = 0.73$	$M_f = 1.20$
Upper Wall	Experiment	Unheated	0UU; x = 10	1UU; x = 10	2UU; x = 10	3UU; x = 10
	Experiment	Heated	N/A	1UH; x = 5	2UH; x = 10	3UH; x = 10
	CFD UMD	Unheated	0UU MCFD			
	CFD UMD	Heated	N/A	1UH MCFD	2UH MCFD	3UH MCFD
	CFD NASA	Unheated	0UU NCFD			3UU NCFD
	CFD NASA	Heated	N/A			3UH NCFD
Lower Wall	Experiment	Unheated	0LH	1LU; x = 13	2LU; x = 14	3LU; x = 14
	Experiment	Heated	N/A	1LH; x = 5	2LH; x = 10	3LH; x = 10
	CFD UMD	Unheated	0LH MCFD			
	CFD UMD	Heated	N/A	1LH MCFD	2LH MCFD	3LH MCFD
	CFD NASA	Unheated	0LH NCFD			3LU NCFD
	CFD NASA	Heated	N/A			3LH NCFD

CFD results from both NASA and the University of Maryland are reported for every test case available. The boundary and flow conditions used for the CFD simulations are reported in Table 6.2. There are a few differences between the flow conditions and the boundary conditions used in CFD. The primary difference is the heated film temperature. The simulations from both NASA and UMD use film temperatures 40 K above ambient. In the experiments, the film flow was only heated by 35 K. This was due to limitations with the film heater. Pressure data for the CFD solutions provided by NASA was not available for comparison.

Table 6.2: Summary of Boundary Conditions for all CFD data and comparison to experiment.

			Boundary Conditions								
	Type	**Heated/ Unheated**	**T_0, Air**	**P_0, Air**	**T U&L Walls**	**T Other Walls**	**T_0 Film**	**P_0 Film**			
								0	1	2	3
Upper Wall	Exp.	Unheated	295	0.99	340	-	295		0.0644	0.090	0.214
	Exp.	Heated	295	0.98	340	-	330		0.0725	0.0105	0.278
	CFD UMD	Unheated									
	CFD UMD	Heated	300	1	340	337	340		0.08	?	0.2
	CFD NASA	Unheated	297		337	297	297		?	?	?
	CFD NASA	Heated	297		337	297	337		?	?	?
Lower Wall	Exp.	Unheated	295	0.99	340	-	295		0.0644	0.090	0.214
	Exp.	Heated	295	0.98	340	-	330		0.0725	0.0105	0.278
	CFD UMD	Unheated			340	337	340				
	CFD UMD	Heated	300	1	340	337	340		0.08	?	0.2
	CFD NASA	Unheated	297		337	297	297		?	?	?
	CFD NASA	Heated	297		337	297	337		?	?	?
Units			**K**	**Atm**	**K**	**K**	**K**		**Atm**	**Atm**	**Atm**

Experimental heat flux results are reported over an *x/s* range of $0 < x/s < 65$. CFD simulation data is available up to $x/s = 75$. Due to the limitations of the imaging system, schlieren images focused on the area between $0 < x/s < 18$. This was done so that the film injection region was adequately captured. The flow structures that are most important to film cooling (shear layer, lip shock, etc.) originate at the film injection louver at $x/s = 0$. Unfortunately, focusing on the injection region removed the upper wall from the imaging region. Figure 6.1 shows all spatial domains and the types of measurements made in each region.

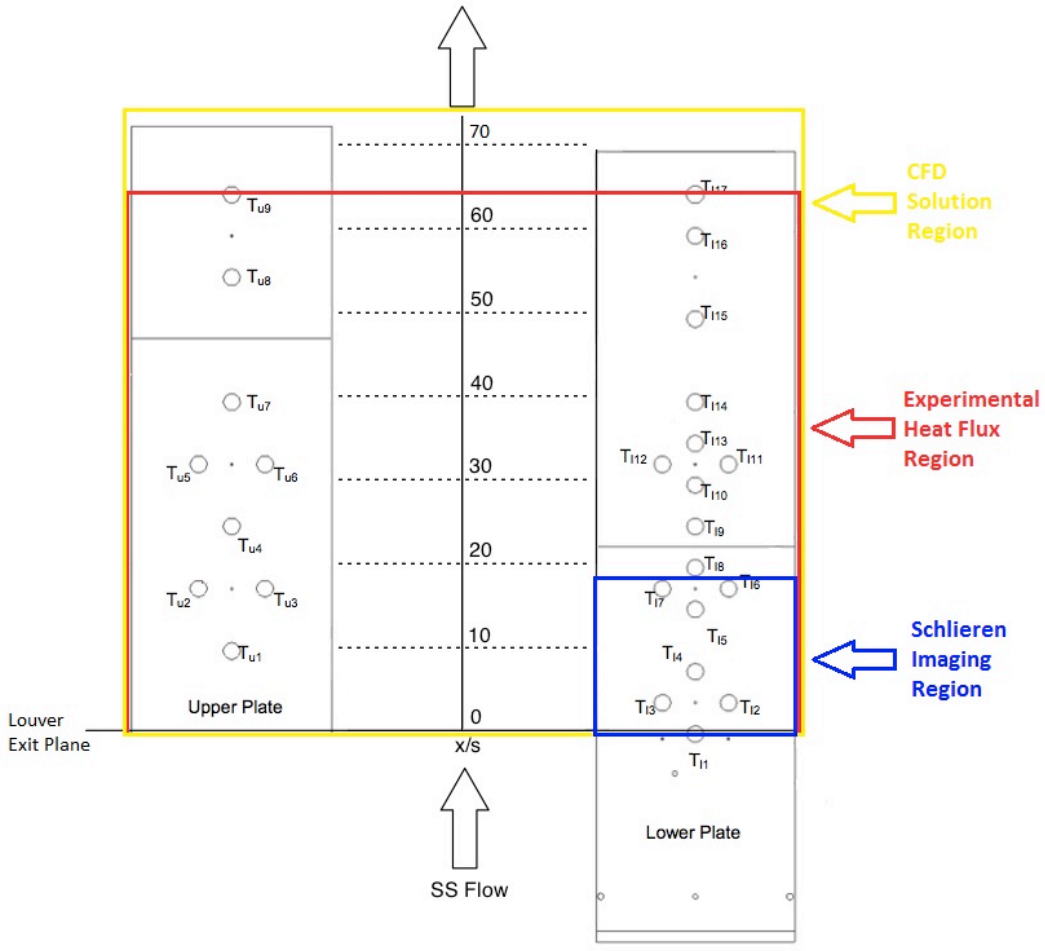

Figure 6.1: Spatial domains of all measurement data. Blue indicates Schlieren imaging region. Red indicates experimental heat flux region. Yellow indicates CFD solution region.

Each test case will be reported and analyzed individually. Comparisons between test cases will be presented in section 6.5. Density gradient images from CFD were not available for comparison to the quantitative data obtained from the schlieren image analysis. Schlieren image data is reported together with the heat flux results in order to provide as much information about the flow as possible.

6.1: Test Case 0

Test Case 0 is the no-film injection case where the film -throttling valve in the intake pipe is fully closed so as to prevent air from entering the film plenum. This creates a situation in which the lower wall is unprotected except for the very small region near the injection point where the core flow expands and turns around the film slot. This case was used to provide the reference heat flux Q_0 in equation 2.2. The decision was made to use this data set as a reference because it corresponds to no film cooling. No air is injected through the film louver. The other choice for the reference heat flux is the results from the upper wall. This wall does not have a protective film layer in any of the test cases. However, the *x/s* locations of the sensors on the upper wall do not correspond directly to the *x/s* locations of the sensors on the lower wall at every point. In order to calculate film cooling effectiveness from equation 2.2, heat fluxes must be compared at the same axial locations. Using the results from Test Case 0 as the reference heat flux allows film cooling effectiveness to be calculated at every *x/s* location on the lower wall. The data points in all plots represent averages of 13 experiments for the lower wall and 10 experiments for the upper.

6.1.1: Schlieren Image Analysis

Figure 6.2: Sample schlieren image for Test Case 0.

Figure 6.2 shows a sample schlieren image for Test Case 0. This image was extracted from a schlieren video taken during one of the experiments and was used as the reference image for the image analysis code. Figure 6.3 shows five flow features that are important to the film cooling results. These structures and their importance to the film cooling results were listed and explained in section 5.2. They are:

1.) Top of shear layer
2.) Lip shockwave
3.) Shockwaves emanating from nozzle throat geometry
4.) Shockwave emanating from start of upper wall test section
5.) Shockwave emanating from end of nozzle curvature.

All of these features are visible in the sample schlieren image and were sought using the image analysis code.

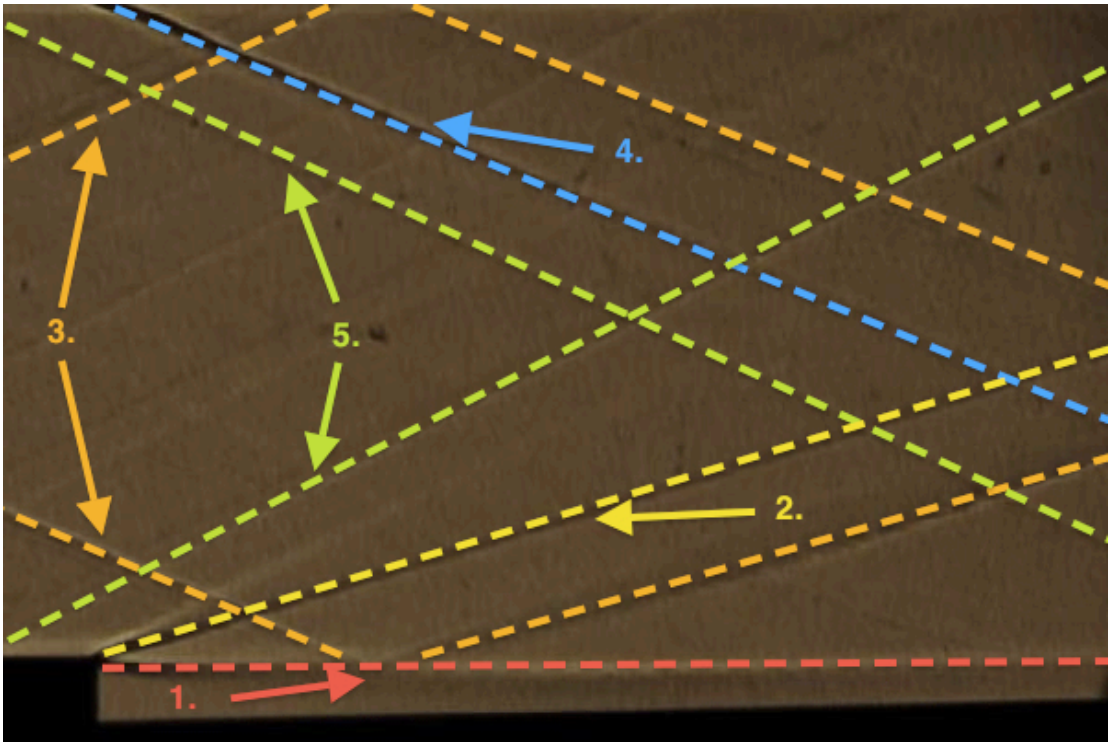

Figure 6.3: Important flow features for Test Case 0. These are: 1.) Shear layer 2.) Shock emanating from injection lip 3.) Shock waves from nozzle geometry 4.) Shock wave emanating from start of upper wall test section 5.) Shock wave emanating from end of nozzle.

Due to the poor quality of the schlieren videos, the image analysis code did not identify every important flow feature in every frame. Figure 6.4 shows the features that were identified in the reference image. This image was chosen as the reference because all but one of the important flow features was identified (the reflection of the third feature off of the shear layer was not captured). Several weak Mach waves were identified in the image as well, but these were not used for the analysis. The average angle and standard deviation of each feature is reported in Table 6.3. The results show that all flow features are steady during the duration of the experiment. There is very little variability among any of the detected lines, with the largest standard deviation being less than a quarter of a degree.

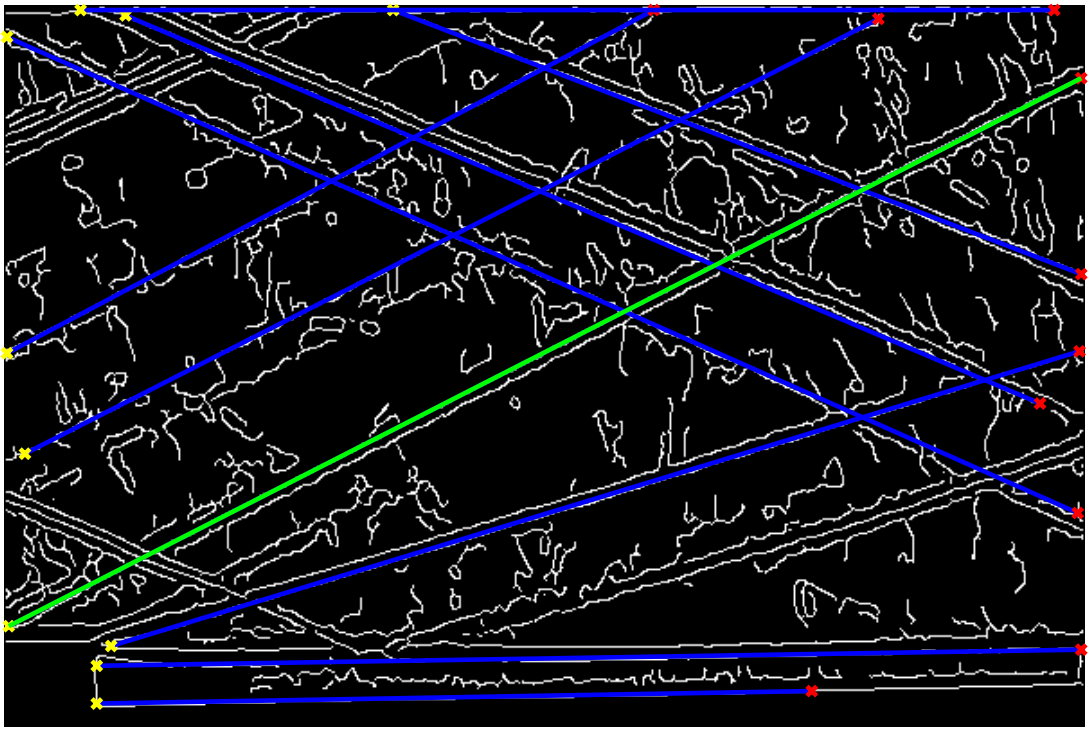

Figure 6.4: Sample schlieren image showing detected line features in flow for Test Case 0. Blue lines indicate detected features. Green indicates longest flow feature.

Table 6.3: Summary of results from automated schlieren image analysis for Test Case 0.

Feature	Mean Angle	Random Error	Standard Deviation	Number of Frames (Max: 72)
Shear Layer	178.74°	0.0515°	0.1637°	42
Lip Shock	163.23°	0.0444°	0.1392°	41
Throat Shock (Upper)	22.12°	0.1397°	0.2470°	13
Throat Shock (Lower)	N/A	N/A	N/A	N/A
Upper Wall Start	24.24°	0.0769°	0.1685°	20
Nozzle End Shock (Upper)	22.5°	0.0301°	0.1045°	50
Nozzle End Shock (Lower)	152.85°	0.0034°	0.0144°	72

6.1.2: Heat Flux Measurements

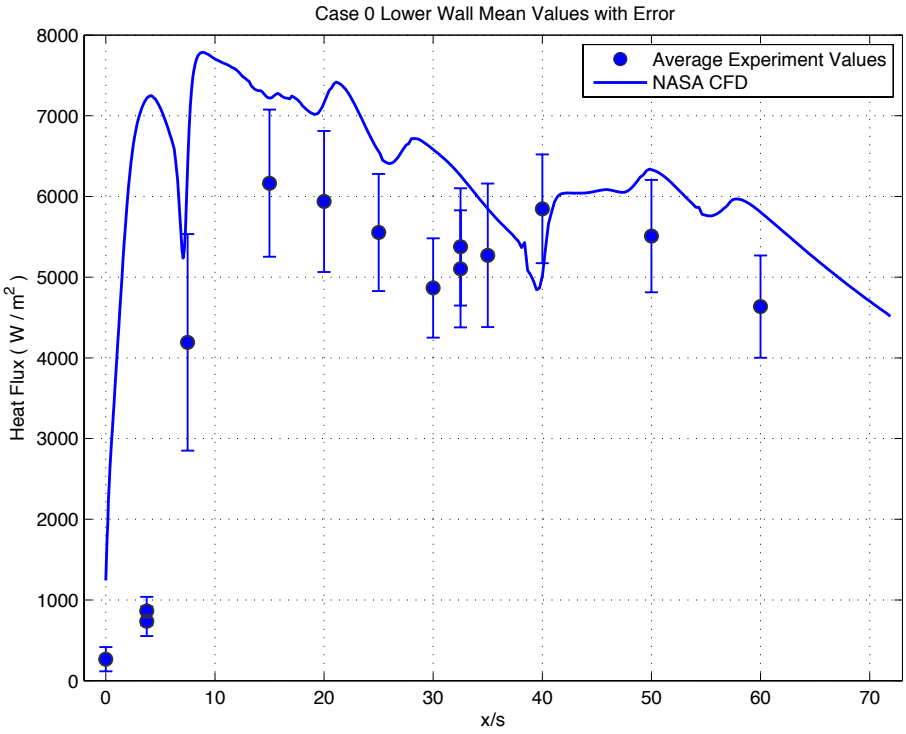

Figure 6.5: Case 0 Lower wall heat flux. Points indicate average of 13 experiments. Error bars give total uncertainty. Solid lines indicate numerical simulations from LOCI-CHEM simulations.

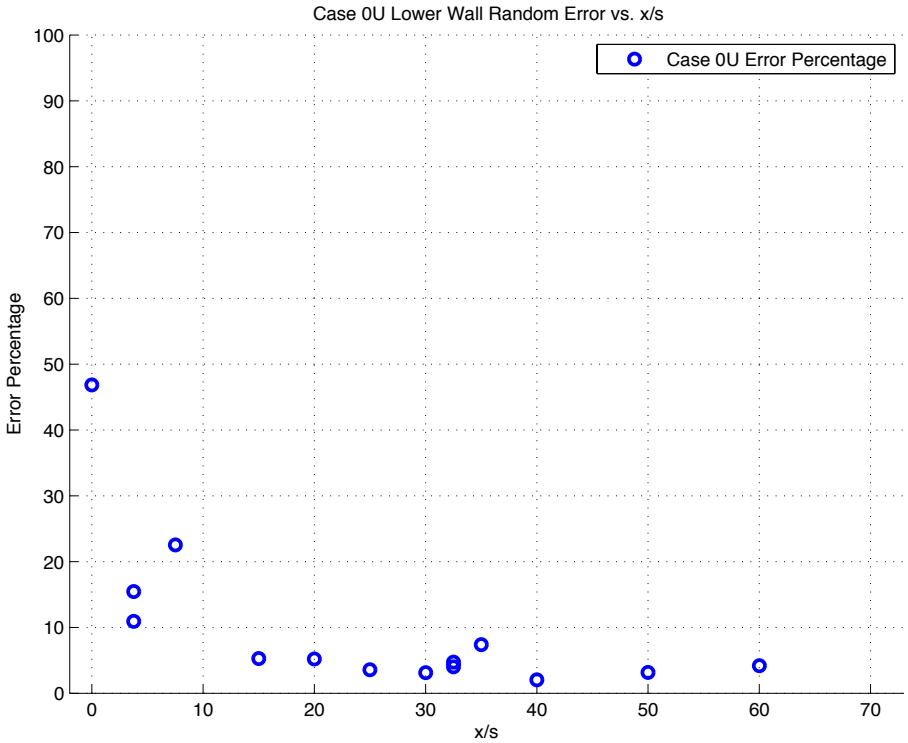

Figure 6.6: Random error vs. x/s location for Test Case 0.

Figure 6.5 shows the heat flux along the lower wall for the no film injection case. The numerical predictions from Dellimore's LOCI-CHEM simulations [5] are overlaid to allow comparison. While both simulation and experiment show rapid increases in wall heat flux with downstream distance in the near-louver region (x/s < 20), the increase occurs less abruptly and at a somewhat larger x/s (i.e. is delayed) in the experiments. This trend is opposite to Cruz's observations in subsonic wall-wake flows [47] (fig. 34 p. 110) where RANS predictions of film cooling effectiveness changed more slowly than the experiments in the near-louver region. Excluding the over-prediction and near-slot region, the trends in the CFD projections are similar to those observed in the experimental data. Figure 6.6 shows the random error plotted against axial location. This plot shows that there is a large amount of variability near the injection region (x/s < 15). The heat flux measurements in this region are smaller than in the rest of the test section and a small fluctuation from run to run greatly impacts the random error. Outside of this area, the random error is between 0 -10 % for the entire test region, indicating consistent measurements from run to run.

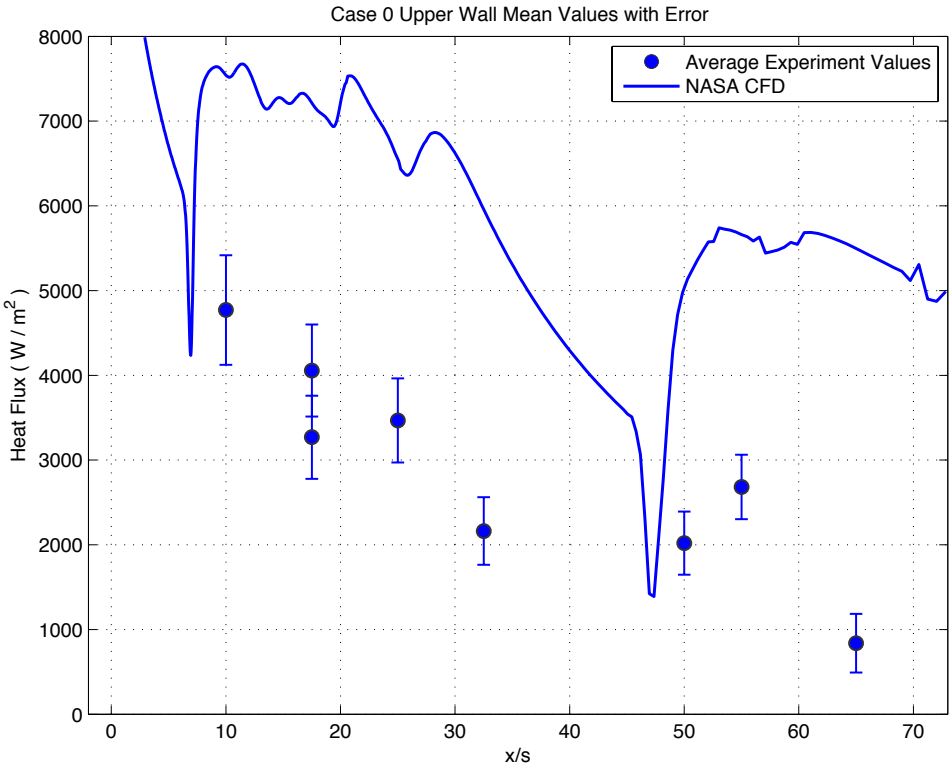

Figure 6.7: Case 0 Upper wall heat flux. Points indicate average of 10 experiments. Solid line indicates numerical simulation from LOCI-CHEM software.

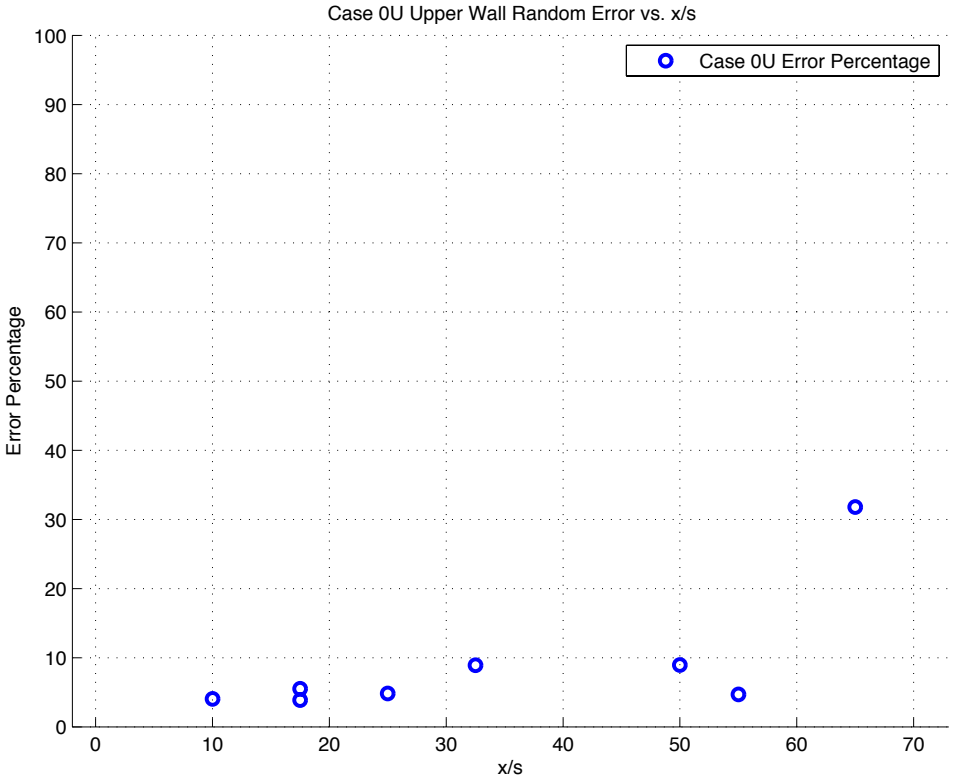

Figure 6.8: Random error vs. x/s location for Test Case 0.

Figure 6.7 shows the heat flux distribution along the upper wall for the no film injection case. As with the lower wall case, the CFD predictions seem to capture the general trend but do not accurately predict the actual heat flux values seen in the experiment. The random error (Figure 6.8) again demonstrates that there is little variability between test runs. The entire test section exhibits a random error less than 10% except for at x/s = 65. This location is near the impingement location of a shockwave (explained in section 6.1.3), which causes some variation in heat flux measurements between datasets.

6.1.3: Relation between Flow Structures and Heat Flux Distributions

Using the quantitative results from the image analysis code and knowledge of oblique shock waves and their reflections, it is possible to predict the shock structure throughout the test section. The results were used to produce a shock diagram that shows all of the impingement points for the major flow features throughout the test section. When viewed with the heat flux data on the same scale, it provides reasoning for many of the sudden fluctuations.

Figure 6.9 shows the generated shock diagram superimposed between the upper and lower wall heat flux results. Viewed in this manner, it is apparent that the shock impingement locations shown in the diagram directly correspond with sharp fluctuations in heat flux. The shock impingements on the upper wall at x/s = 7, 27, 48.8, and 57.4 seen in the diagram all correspond with sharp changes in the heat flux plot. The lower wall heat flux plot also shows fluctuations at the impingement locations of x/s = 27, 42, and 55.3. The large change in heat flux that is visible on the

lower wall plot at *x/s* = 7 is due to a shockwave that the analysis code did not detect (Throat Shock (Lower) from Table 6.3).

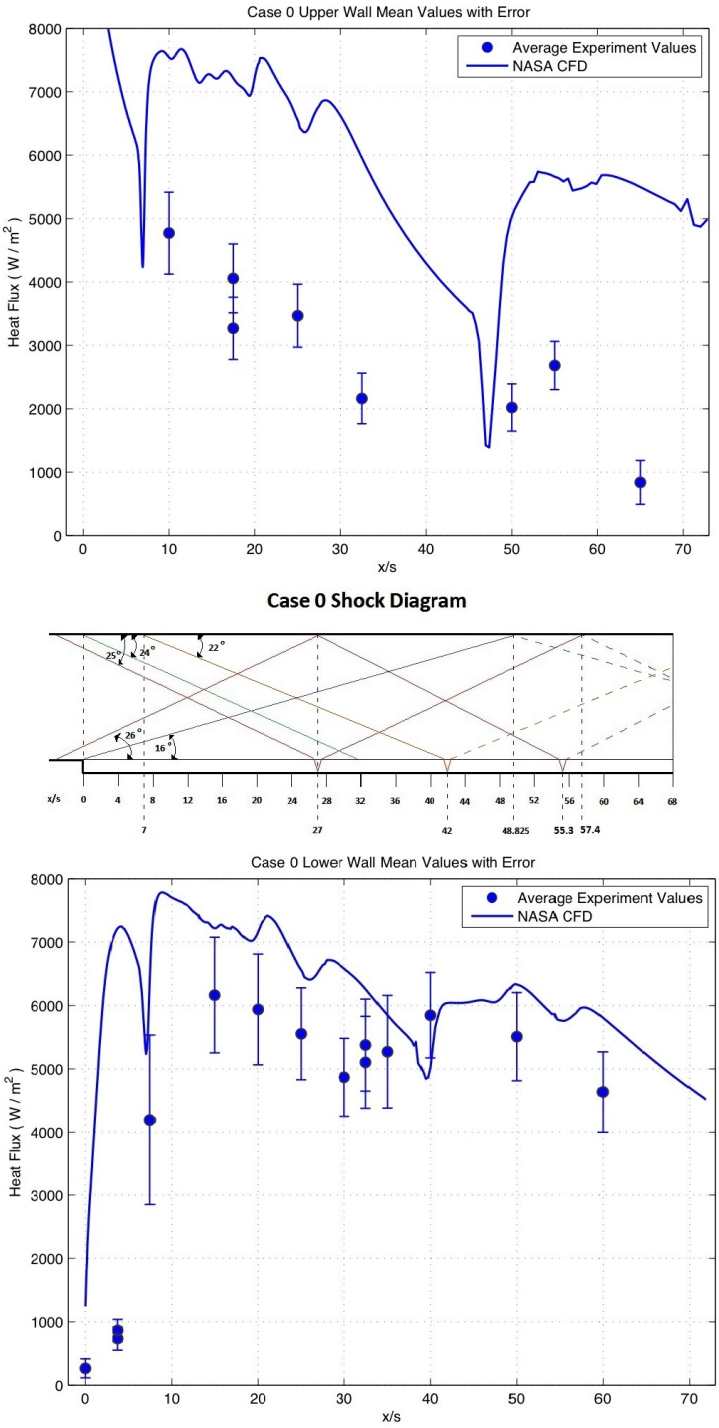

Figure 6.9: Top: Heat flux results for Test Case 0U. Middle: Shock diagram generated using image analysis code. Bottom: Heat flux results for Test Case 0U. All results are presented on the same axial scale.

6.1.4: Comparison to CFD

Film cooling effectiveness is not applicable to Test Case 0 (no film injection). The Ω variable defined in equations 5.8-5.10 provides a measure of the agreement between the experimental results and the CFD simulations. Figure 6.10 shows Ω plotted against axial location. The individual Ω_i values exhibit a large amount of scatter for $x/s < 15$ on the lower wall. This indicates variability in the experimental results in this region. This correlates with the results of the random error analysis, which showed increased error near the film injection louver. Beyond $x/s = 15$, the Ω_i values correspond well with the value of Ω_{bar}. The upper wall shows more variability throughout the test section, with a general increase in the spread of the Ω_i values as x/s location is increased.

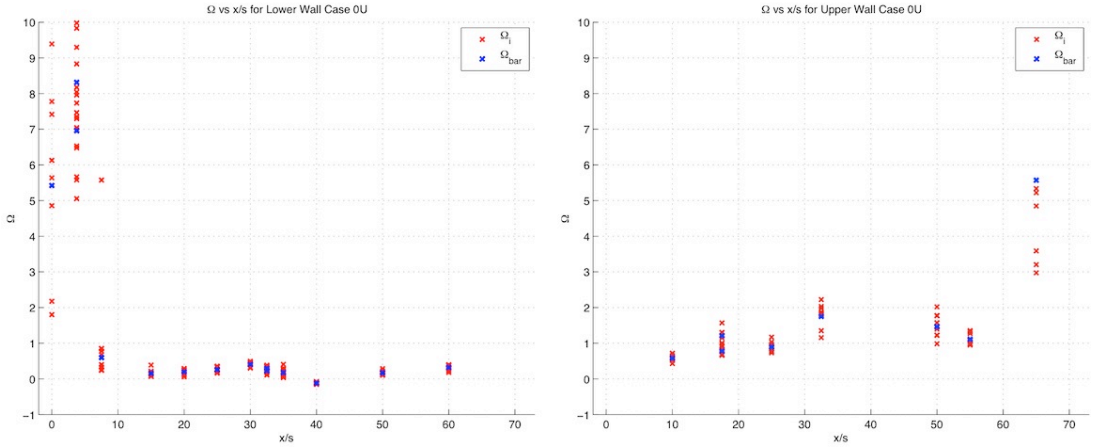

Figure 6.10: Ω_I and Ω_{bar} vs. x/s location for Test Case 0. Red x's indicate individual Ω_I values. Blue x's indicate Ω_{bar} values. Left: Lower wall. Right: Upper wall.

It is apparent from the analysis of the random error and Ω plots that the largest disagreement between the experimental and numerical results occurs in the film injection region ($x/s < 15$) on the lower wall. Including this region, the Ω value for Test Case 0 is 1.67 (both lower and upper wall $\Omega = 1.67$). Physically, this means that the CFD over-predicts the value of heat flux in the test section by 167 %. However, if

the film injection region is neglected, Ω is only 0.245 for the lower wall (see Figure 6.11). This indicates that the Loci-CHEM code predicts heat flux much more accurately outside of the injection region.

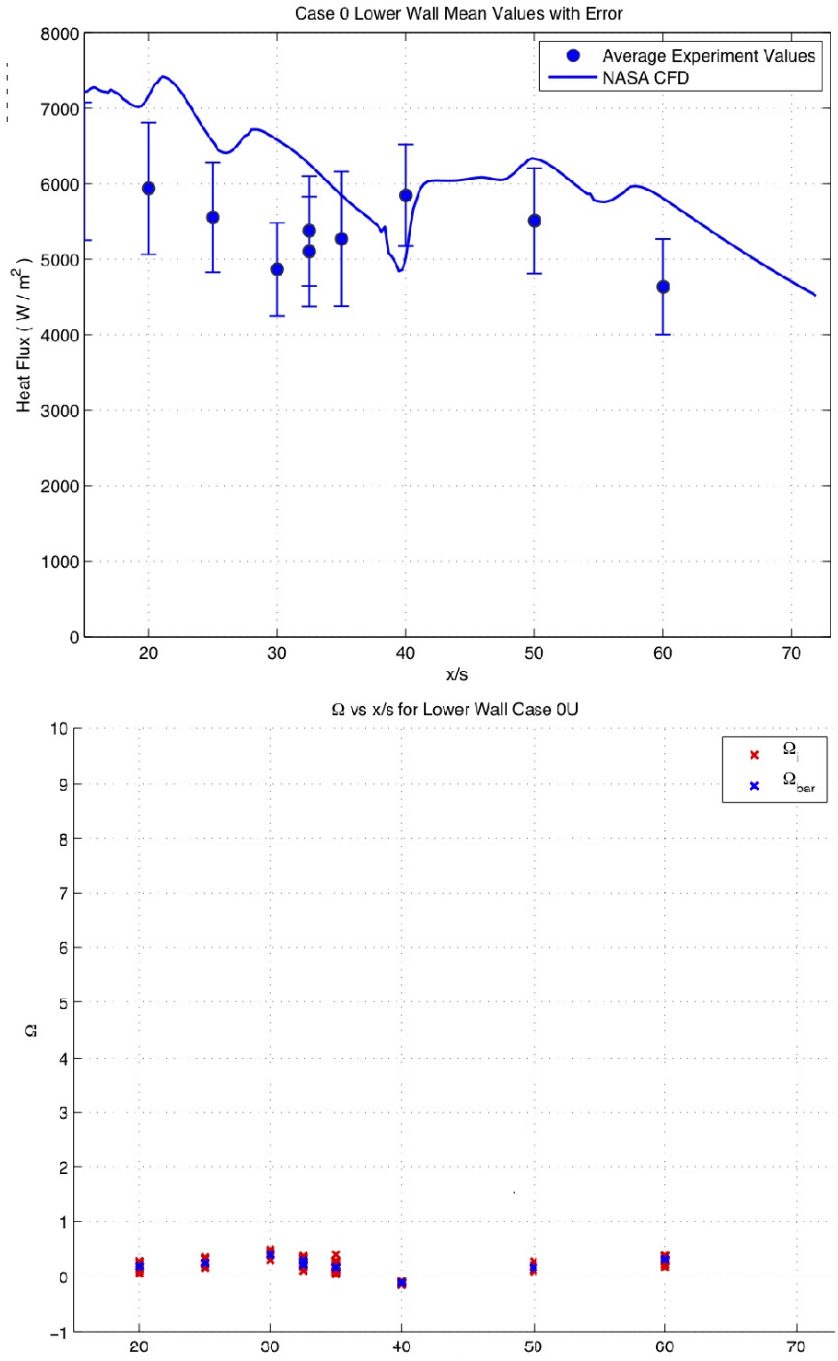

Figure 6.11: Test Case 0LU. Upper: Plot of heat flux vs. x/s for x/s > 15. Lower: Plot of Ω for x/s > 15.

6.1.5: Test Case 0 Summary Table

Table 6.4: Test Case 0 summary table

$T_{ambient}$	295 K
$P_{ambient}$	0.99 atm
T_{film}	N/A
P_{film}	N/A
Film throttle valve setting	Closed
Burner inlet valve setting	Closed
Ω (Upper Wall)	1.67
Ω (Lower Wall)	1.67
Average Heat Flux (Upper Wall)	2908 W/m^2
Average Heat Flux (Lower Wall)	4308 W/m^2
Peak Heat Flux (Upper Wall)	4770 W/m^2
Location of Peak Heat Flux (Upper Wall)	x/s = 10
Peak Heat Flux (Lower Wall)	6164 W/m^2
Location of Peak Heat Flux (Lower Wall)	x/s = 15
Average Effectiveness	N/A
Peak Effectiveness	N/A
Locations of Peak Effectiveness	N/A
Number of Schlieren Images	72

6.2: Test Case 1

Test Case 1 is the Mach 0.50 film injection case. The film-throttling valve in the intake pipe was partially opened to allow a subsonic film to develop along the lower wall. Experiments with both heated and unheated film (Test Cases 1H and 1U respectively) were performed for this test case. The film was expected to provide minimal protection due to the large difference in the film and core Mach numbers. The latter suggests that the convective Mach number is high and the shear layer between the film and core flows grows quickly. The impingement region marks the point where the growing shear layer contacts the lower wall and where the film protecting the wall breaks down. Thus, this is where the heat flux is expected to spike.

Test Case 1H proved to be more challenging than expected because of combustion problems in the film heater. The small amount of air flowing through the film heater for this specific test case required the use of a very small amount of propane. This made sustained combustion difficult to obtain. Only five data sets were obtained for Cases 1UH and 1LH for use in analysis because of the unstable combustion. As a result, the random component of the uncertainty in Case 1H is larger than in all other cases. Case 1UU plots present the average of 10 experiments and Case 1LU plots present the average of 13 experiments.

6.2.1: Schlieren Image Analysis

Figure 6.12: Sample schlieren image for Test Case 1.

Figure 6.12 shows a sample schlieren image for Test Case 1. This image was extracted from a schlieren video taken during one of the experiments and was used as the reference image for Test Case 1 in the image analysis code. Figure 6.13 shows five flow features that are important to the film cooling results. These structures are the same as those from Test Case 0 and their importance to the film cooling results were listed and explained in section 6.1.1.

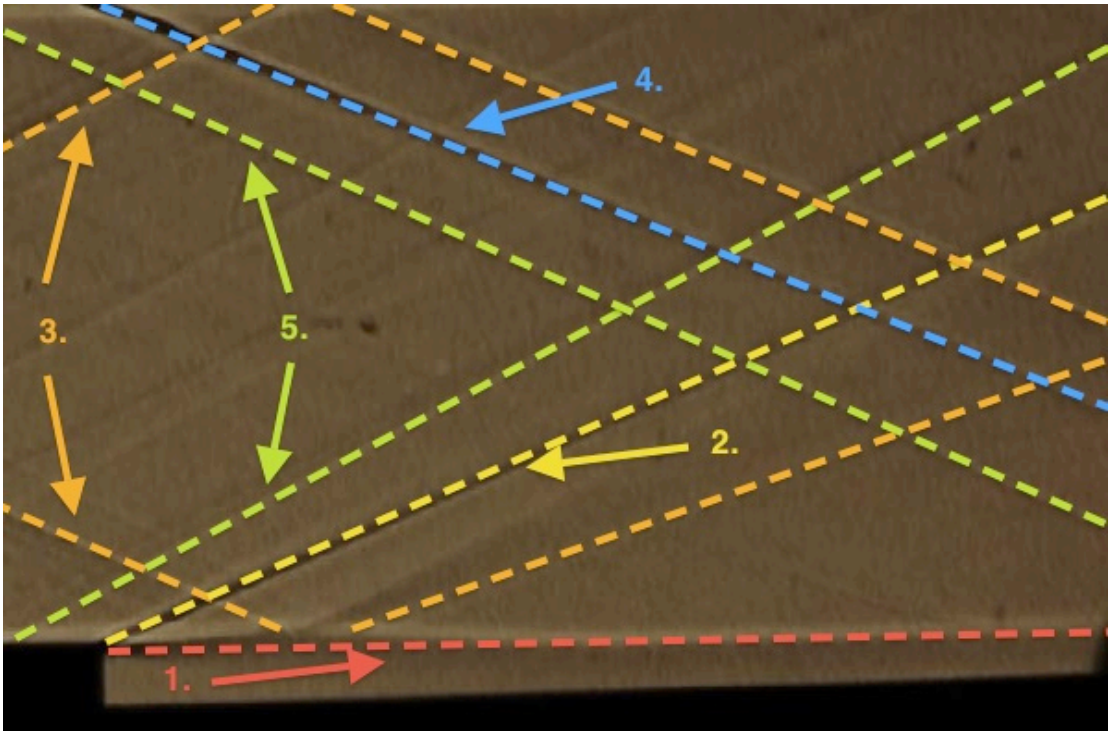

Figure 6.13: Important flow features for Test Case 1. These are: 1.) Shear layer 2.) Shock emanating from injection lip 3.) Shock waves from nozzle geometry 4.) Shock wave emanating from start of upper wall test section 5.) Shock wave emanating from end of nozzle.

Similar to the results from Test Case 0, the image analysis code did not identify every important flow feature in every frame. Figure 6.14 shows the features that were identified in the reference image. The reference image contains all of the major flow features except for the shockwaves emanating from the upstream nozzle contraction (feature 3, refer to Figure 6.13). Again, several weak Mach waves were identified in the image as well, but were not used for the analysis. The average angle and standard deviation of each feature is reported in Table 6.5. The results show that all flow features are steady during the duration of the experiment. There is even less variability than occurred in Test Case 0, with the largest standard deviation being approximately 0.15°.

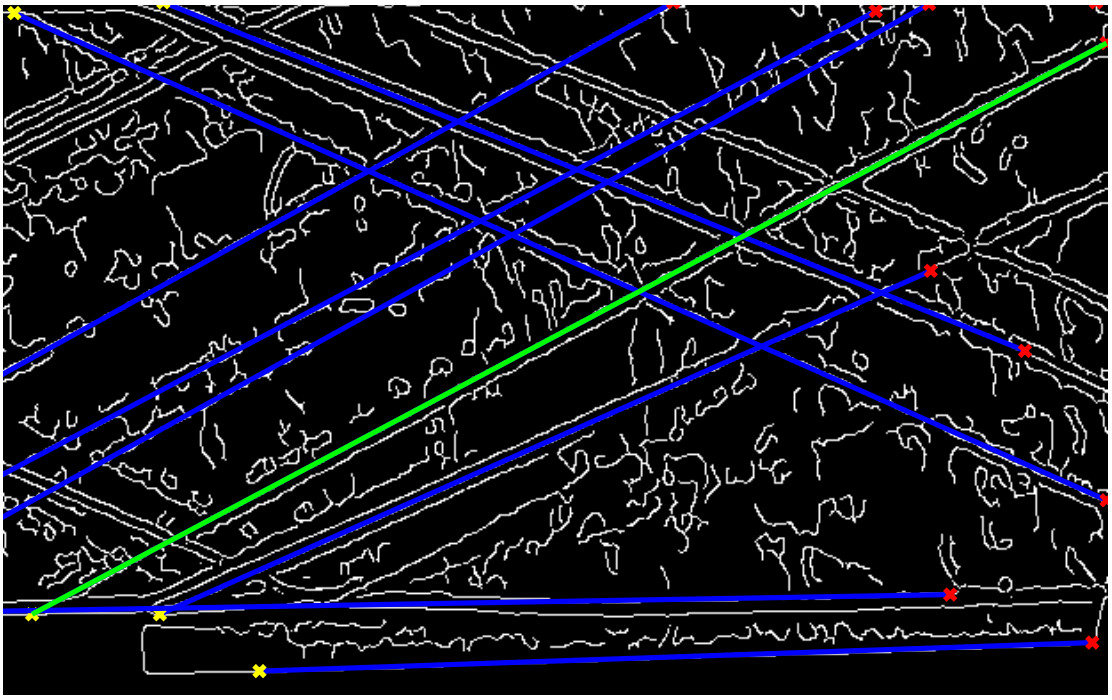

Figure 6.14: Sample schlieren image showing detected line features in flow for Test Case 1. Blue lines indicate detected features. Green indicates longest flow feature.

Table 6.5: Summary of results from automated schlieren image analysis for Test Case 1.

Feature	Mean Angle	Random Error	Standard Deviation	Number of Frames (Max: 72)
Shear Layer	178.77°	0.0117°	0.0367°	41
Lip Shock	156.02°	0.0602°	0.1321°	20
Throat Shock (Upper)	N/A	N/A	N/A	N/A
Throat Shock (Lower)	N/A	N/A	N/A	N/A
Upper Wall Start	22.07°	0.0188°	0.0760°	68
Nozzle End Shock (Upper)	23.94°	0.0398°	0.1278°	43
Nozzle End Shock (Lower)	152.18°	0.0808°	0.1534°	15

6.2.2: Heat Flux Measurements

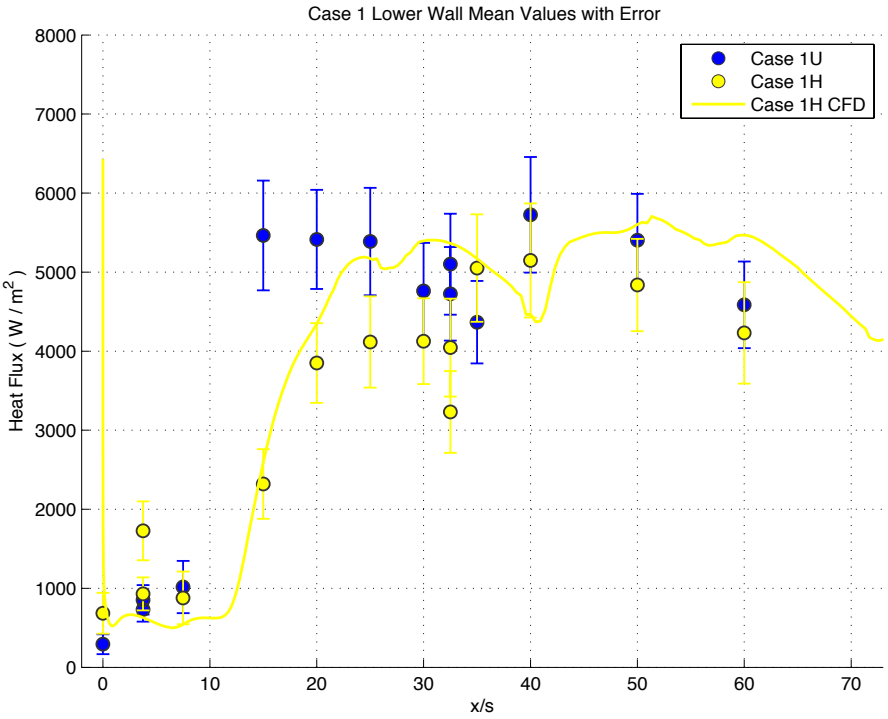

Figure 6.15: Case 1 Lower wall heat flux. Blue markers indicate average of 13 unheated experiments (Case 1LU). Yellow markers indicate average of 5 heated experiments (Case 1LH). Error bars give total uncertainty. Solid line indicates numerical simulations from LOCI-CHEM simulations.

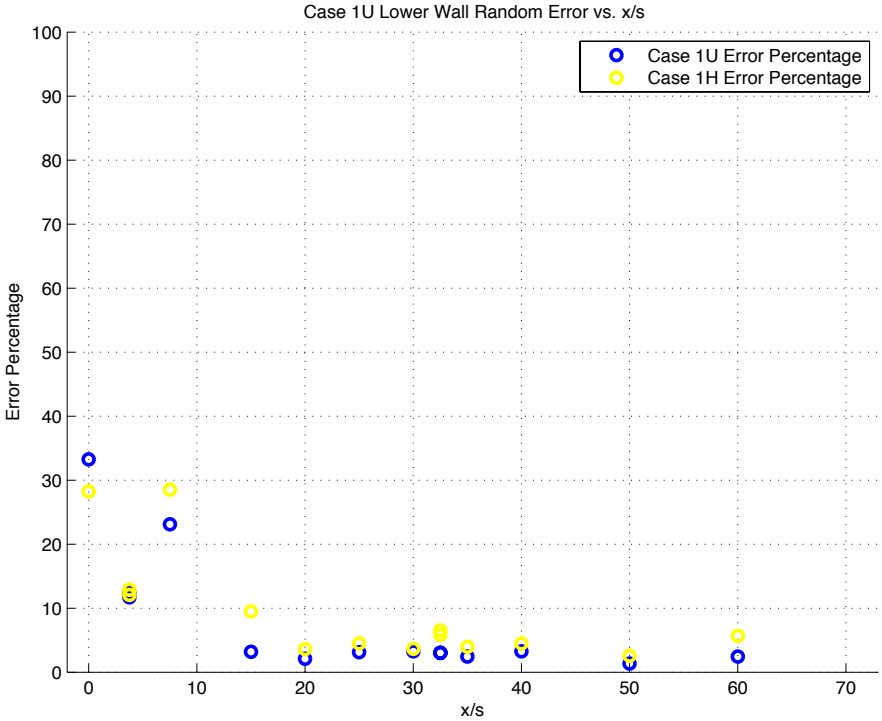

Figure 6.16: Random error vs. x/s location for Test Case 1. Blue markers indicate Case 1 LU. Yellow markers indicate Case 1 LH.

Figure 6.15 shows the heat flux along the lower wall for the Mach 0.50 heated and unheated film injection case (Case 1LH and Case 1LU respectively). Numerical predictions from Dellimore's LOCI-CHEM simulations [5] are overlaid to allow comparison with the heated test case (Case 1LH). Case 1LU demonstrates a rapid rise in heat flux near the injection point, similar to what was seen in Test Case 0. However, Case 1LH shows a much more gradual rise in heat flux. This is due to the increased thermal protection afforded by the heated film. Unlike the numerical solution from Test Case 0, the CFD results under-predict heat flux near the louver ($x/s < 15$). The trends in the CFD projection are similar to those observed in the heated experimental data (Case 1LH), matching very closely in the middle of the test region ($20 < x/s < 40$). Figure 6.16 shows the random error plotted against axial location. Similar to the results from Test Case 0, the most variability occurs near the film injection louver ($x/s < 15$). Beyond $x/s = 10$, the random error is between 0 -10 % for the entire test region, indicating consistent measurements from run to run. The random error is slightly higher for Case 1LH throughout the test region. This is expected due to the smaller number of tests performed at this condition.

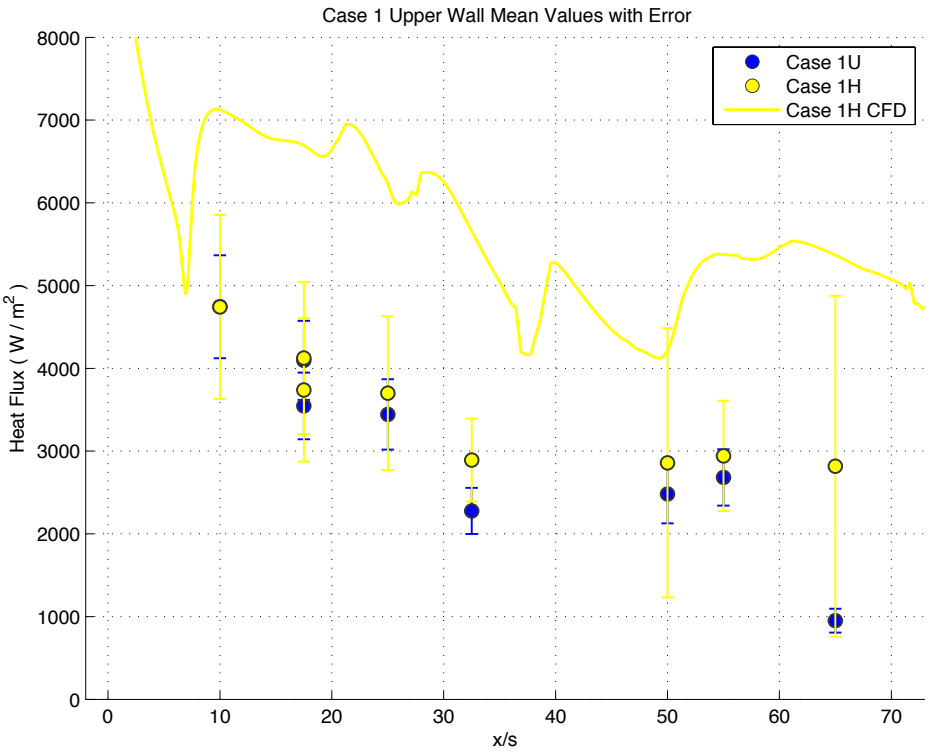

Figure 6.17: Case 1 Upper wall heat flux. Blue markers indicate average of 10 unheated experiments (Case 1UU). Yellow markers indicate average of 5 heated experiments (Case 1UH). Error bars give total uncertainty. Solid line indicates numerical simulations from LOCI-CHEM simulations.

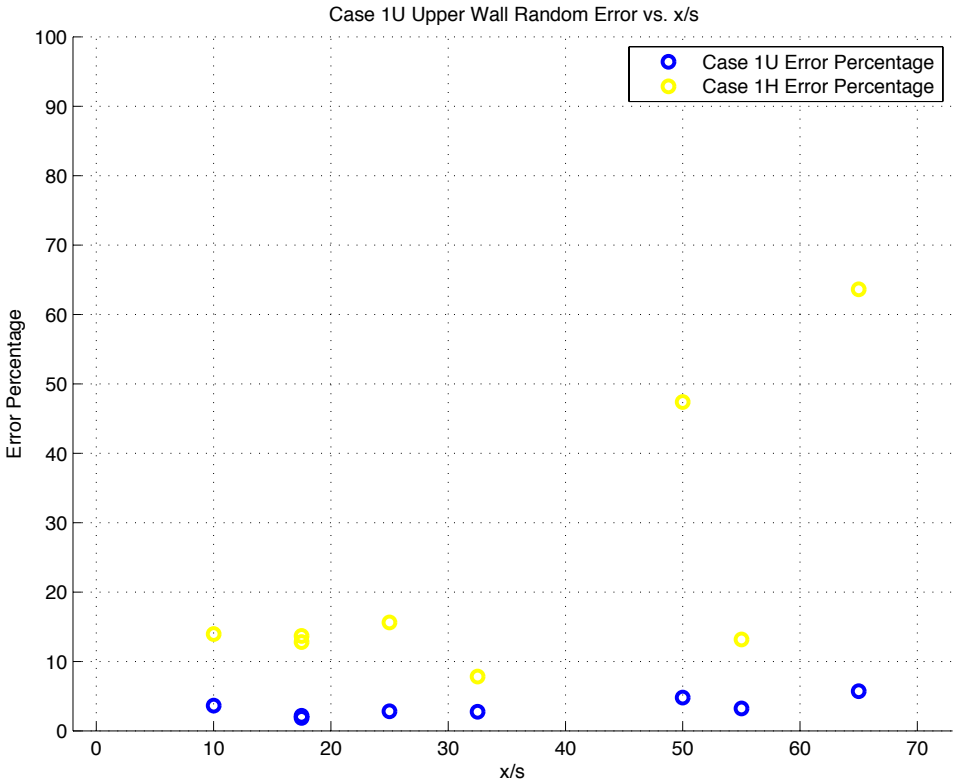

Figure 6.18: Random error vs. x/s location for Test Case 1. Blue markers indicate Case 1 UU. Yellow markers indicate Case 1 UH.

Figure 6.17 shows the heat flux distribution along the upper wall for the Mach 0.50 injection case. As seen with Test Case 0, the CFD prediction seems to capture the general trend but does not accurately predict the actual heat flux values seen in the experiment. The random error (Figure 6.18) is remarkably different for Case 1UU and Case 1UH. For Case 1UU, there is little variability between test runs and the random error is less than 10% throughout the test section. Case 1UH has a higher random error at every location and exhibits two sharp spikes at x/s = 50 and 65. These are partially due to the fact that the locations are near the impingement point of a shockwave (see section 6.2.3). The random error is also higher for Case 1UH due to the reduced number of tests performed at this condition.

6.2.3: Relation between Flow Structures and Heat Flux Distributions

The results of the schlieren image analysis code were used to produce a shock diagram that shows the impingement points for the major flow features throughout the test section. Not all significant flow features were detected (refer to Table 6.5). Figure 6.19 shows the generated shock diagram superimposed between the upper and lower wall heat flux results. It is again apparent that the shock impingement locations shown in the diagram directly correspond with fluctuations in heat flux. The shock impingements on the upper wall at x/s = 25.7, 34.65, and 55.3 seen in the diagram all correspond with changes in the heat flux plot. The lower wall heat flux plot also shows fluctuations at the impingement locations of x/s = 25.7 and 55.3. The large changes in heat flux that are visible on the upper wall plot at x/s = 7 and on the lower wall at x/s = 40 are due to a shockwave and it's reflection that the analysis code did not detect (Throat Shock (Lower) from Table 6.5).

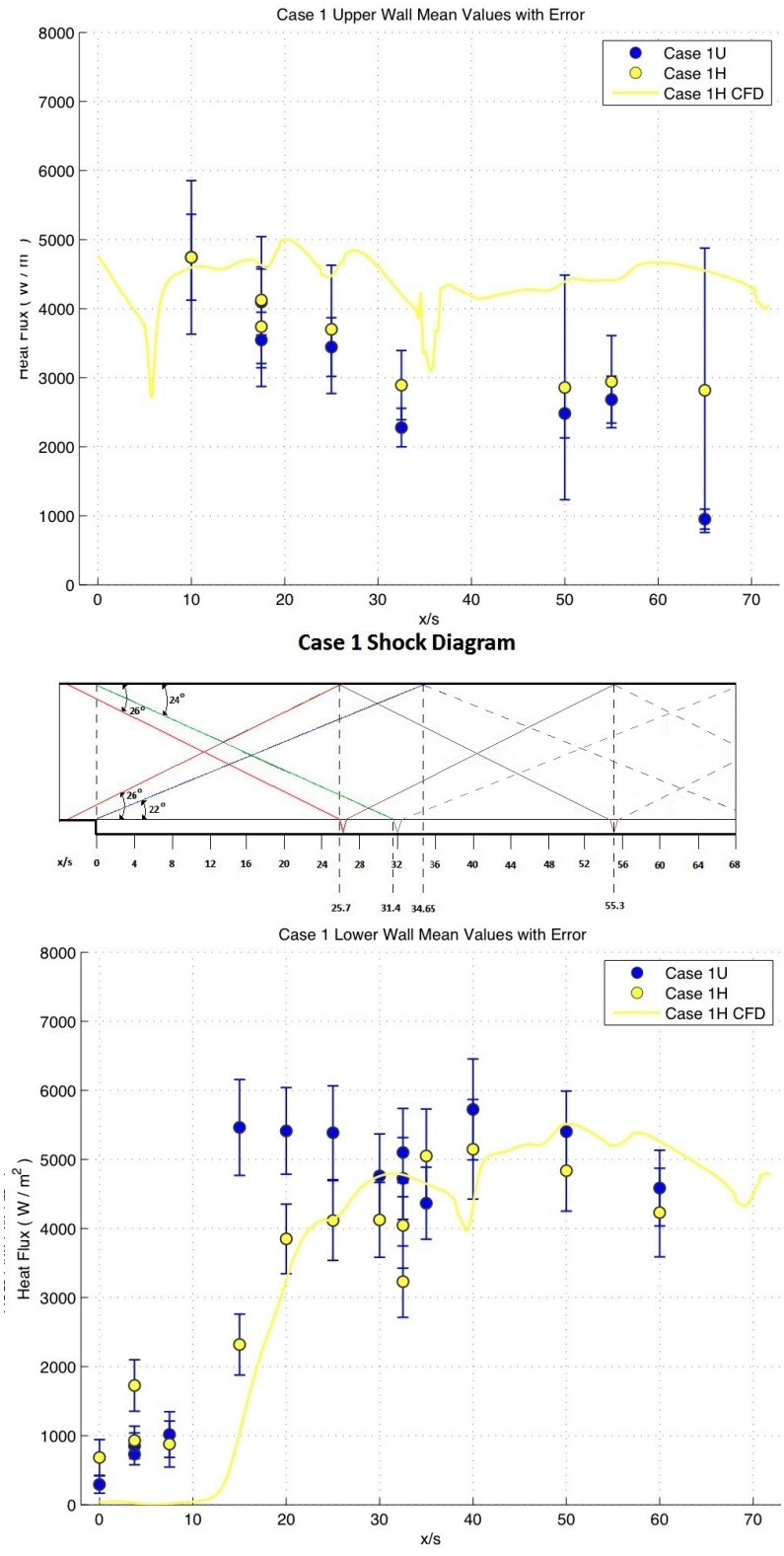

Figure 6.19: Top: Heat flux results for Test Case 1. Middle: Shock diagram generated using image analysis code. Bottom: Heat flux results for Test Case 1. All results are presented on the same axial scale.

6.2.4: Comparison to CFD

Film cooling effectiveness is calculated for Test Case 1H using equation 2.2 (see Figure 6.20). The lower wall data from Test Case 0 (Case 0LU) is used as the reference heat flux (Q_0). For both Case 1LU and Case 1LH, the area directly after the film injection louver is well protected. Both cases have an effectiveness above 75% at x/s = 7.5. The effectiveness for Case 1LU drops rapidly beyond this location, falling to approximately 10%. Case 1LH displays a more gradual decrease in the film cooling effectiveness, staying above 25 % before x/s = 30. The effectiveness for this case stays higher throughout the test section, falling below 10% at only two locations. The average effectiveness is 12.35 % for Case 1LU and 28.74 % for Case 1LH. This compares quite favorably to the average effectiveness of 30.31 % predicted by LOCI-CHEM for Case 1LH. In comparison to the CFD prediction, it can be seen that the numerical results overestimate the effectiveness at all but one location. The trend predicted by the CFD closely matches the trend of decreasing effectiveness seen in the experimental results.

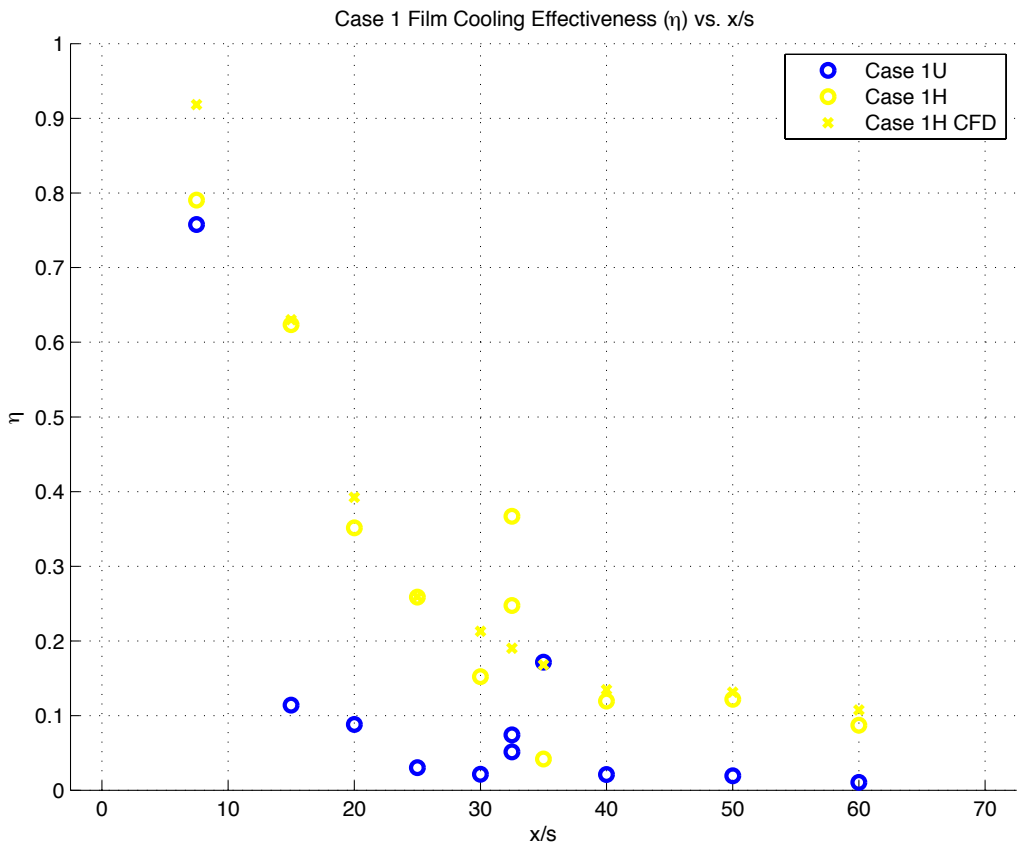

Figure 6.20: Film Cooling Effectiveness plot for Test Case 1. Blue markers indicate unheated film injection (Case 1LU). Yellow markers indicate heated film injection (Case 1LH). 'X' markers indicate numerical simulation from LOCI-CHEM software.

Figure 6.21 shows Ω plotted against axial location. Unlike the results from Test Case 0, the individual Ω_i values do not exhibit a large amount of scatter anywhere in the test region for the lower wall. This indicates there is very little variability at any specific axial location. This is slightly different from what the results of the random error analysis seemed to indicate. Although the random error values near the injection region were less than in Test Case 0, two of the *x/s* locations near the injection region had a random error greater than 25%. The upper wall again shows more variability throughout the test section, with a general increase in the spread of the Ω_i values as *x/s* location is increased and the worst spread occurring beyond *x/s* = 50.

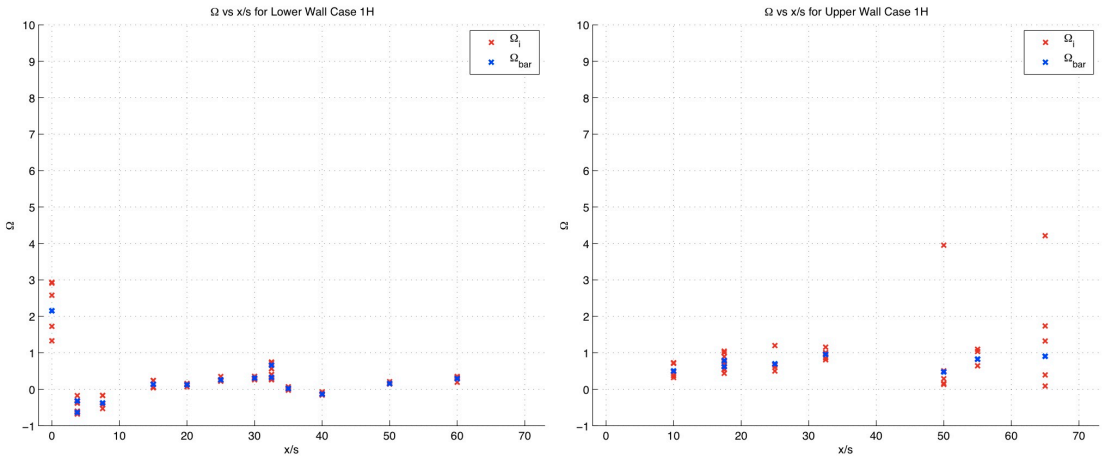

Figure 6.21: Ω_l and Ω_{bar} vs. x/s location for Test Case 1. Red x's indicate individual Ω_l values. Blue x's indicate Ω_{bar} values. Left: Lower wall. Right: Upper wall.

The Ω values for Case 1LH and Case 1UH are 0.21 and 0.72 respectively. Physically, this means that the CFD over-predicts the value of heat flux on lower wall by 21 % and on the upper wall by 72%. Excluding the film injection region on the lower wall again improves the agreement between the numerical solution and experiment values. The value of Ω drops to 0.16 (see Figure 6.22). This indicates that the Loci-CHEM code predicts heat flux very accurately outside of the injection region for this test case.

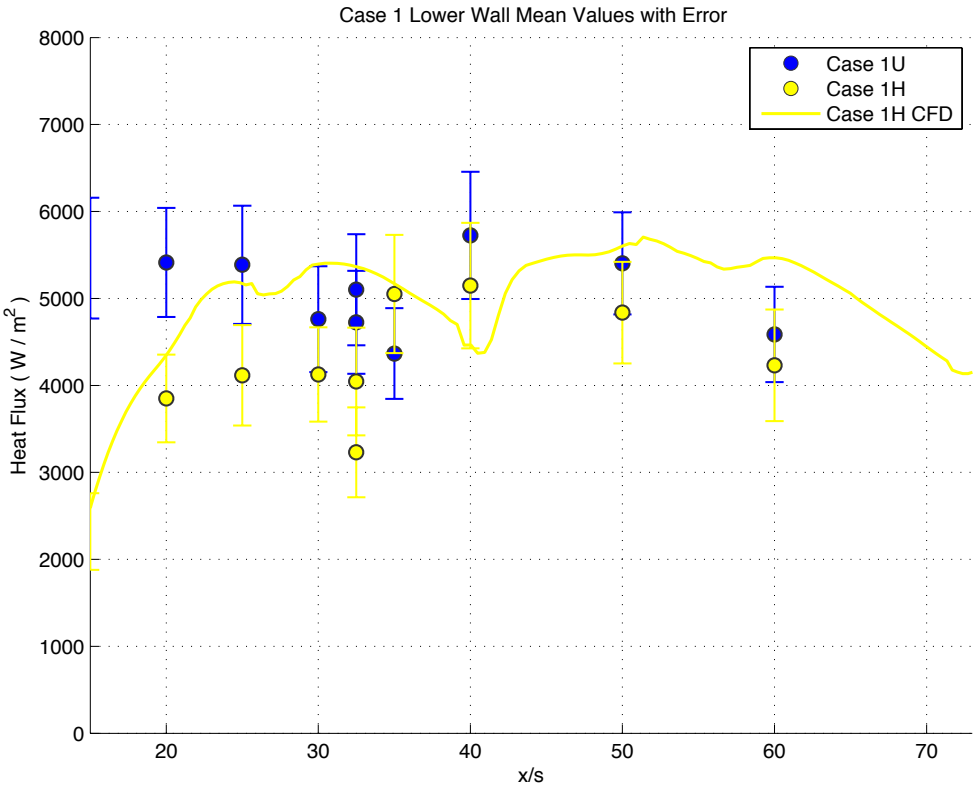

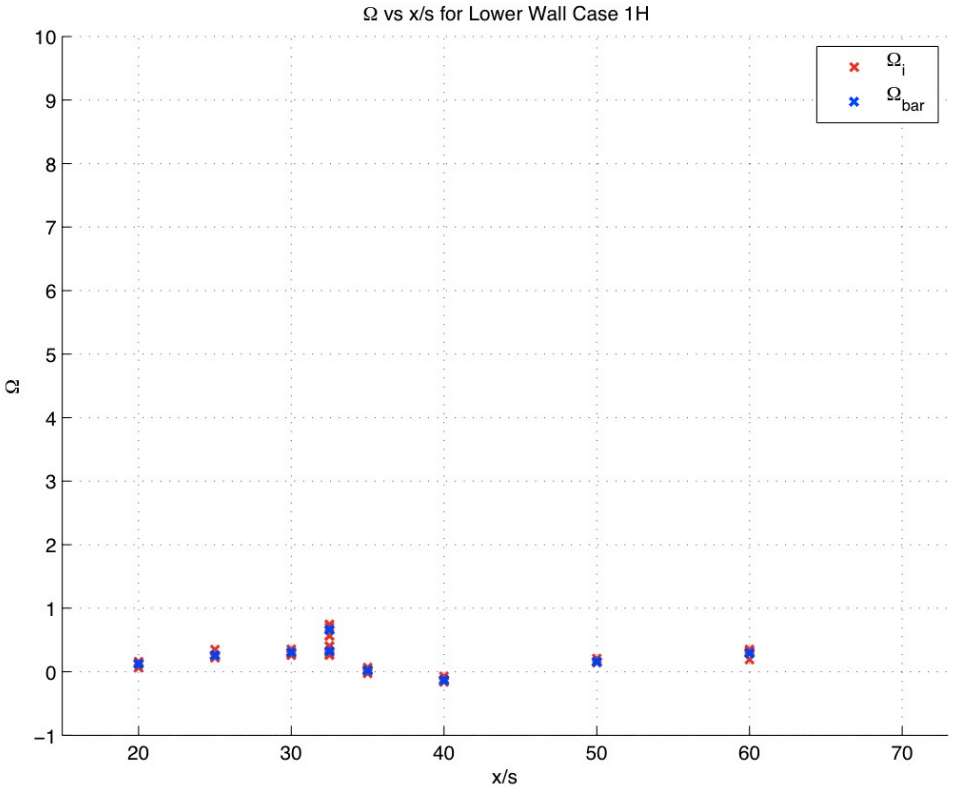

Figure 6.22: Test Case 1LH. Upper: Plot of heat flux vs. x/s for x/s > 15. Lower: Plot of Ω for x/s > 15.

6.2.5: Test Case 1 Summary Table

Table 6.5: Test Case 1UU and 1LU summary table

$T_{ambient}$	295 K
$P_{ambient}$	0.99 atm
T_{film}	295 K
P_{film}	0.0644 atm
Film throttle valve setting	Partially Open (~15 %)
Burner inlet valve setting	Closed
Ω (Upper Wall)	N/A
Ω (Lower Wall)	N/A
Average Heat Flux (Upper Wall)	3028 W/m^2
Average Heat Flux (Lower Wall)	3845 W/m^2
Peak Heat Flux (Upper Wall)	4743 W/m^2
Location of Peak Heat Flux (Upper Wall)	*x/s* = 10
Peak Heat Flux (Lower Wall)	5725 W/m^2
Location of Peak Heat Flux (Lower Wall)	*x/s* = 40
Average Effectiveness	0.1235 (12.35 %)
Peak Effectiveness	0.7576 (75.76 %)
Locations of Peak Effectiveness	*x/s* = 7.5
Number of Schlieren Images	72

Table 6.6: Test Case 1UH and 1LH summary table

$T_{ambient}$	295 K
$P_{ambient}$	0.98 atm
T_{film}	330 K
P_{film}	0.0725 atm
Film throttle valve setting	Partially Open (~15 %)
Burner inlet valve setting	Partially Open (~5 %)
Ω (Upper Wall)	0.33
Ω (Lower Wall)	- 0.26
Average Heat Flux (Upper Wall)	3227 W/m^2
Average Heat Flux (Lower Wall)	3477 W/m^2
Peak Heat Flux (Upper Wall)	4742 W/m^2
Location of Peak Heat Flux (Upper Wall)	*x/s* = 10
Peak Heat Flux (Lower Wall)	5148 W/m^2
Location of Peak Heat Flux (Lower Wall)	*x/s* = 40
Average Effectiveness	0.2874 (28.74 %)
Peak Effectiveness	0.7905 (79.05 %)
Locations of Peak Effectiveness	*x/s* = 7.5
Number of Schlieren Images	72

6.3: Test Case 2

Test Case 2 is the Mach 0.73 film injection case. The film-throttling valve in the intake pipe was partially opened to allow the formation of a film flow in the test section. Measurements were made with both a heated an unheated film (Test Case 2H and Test Case 2U respectively). It was expected that this case would provide significantly more protection than the previous case due to the higher speed film and reduced convective Mach number. This decreases the shear layer growth rate and moves it's impingement point farther downstream. This case most closely matches the velocity ratio present in the J-2X engine. The higher film Mach number in comparison to Test Case 1H allowed for a higher flow-rate through the film heater. This increased flow-rate allowed for stable combustion to be maintained throughout the experiment and a full 10 experiments to be completed. Case 2UU plots present the average of 10 experiments and Case 2LU plots present the average of 14 experiments. Case 2UH and Case 2LH plots present the average of 10 experiments.

6.3.1: Schlieren Image Analysis

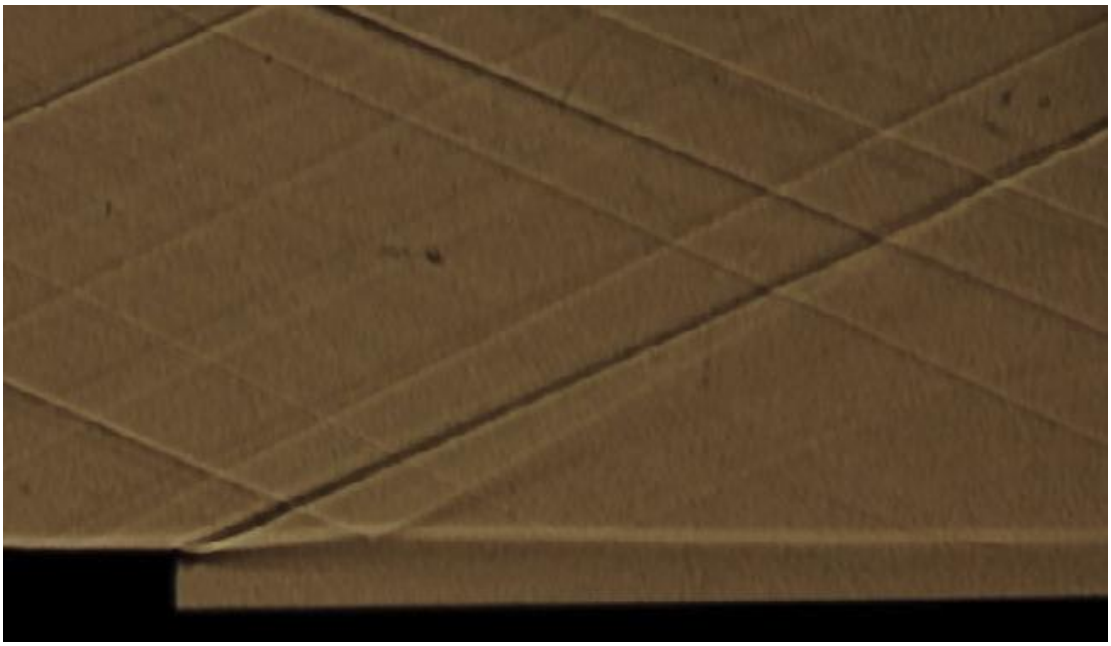

Figure 6.23: Sample schlieren image for Test Case 2.

Figure 6.23 shows a sample schlieren image for Test Case 2. This image was extracted from a schlieren video taken during one of the experiments and was used as the reference image for Test Case 2 in the image analysis code. Figure 6.24 shows five flow features that are important to the film cooling results. These structures are the same as those from Test Case 0 and Test Case 1 and their importance to the film cooling results were listed and explained in section 6.1.1.

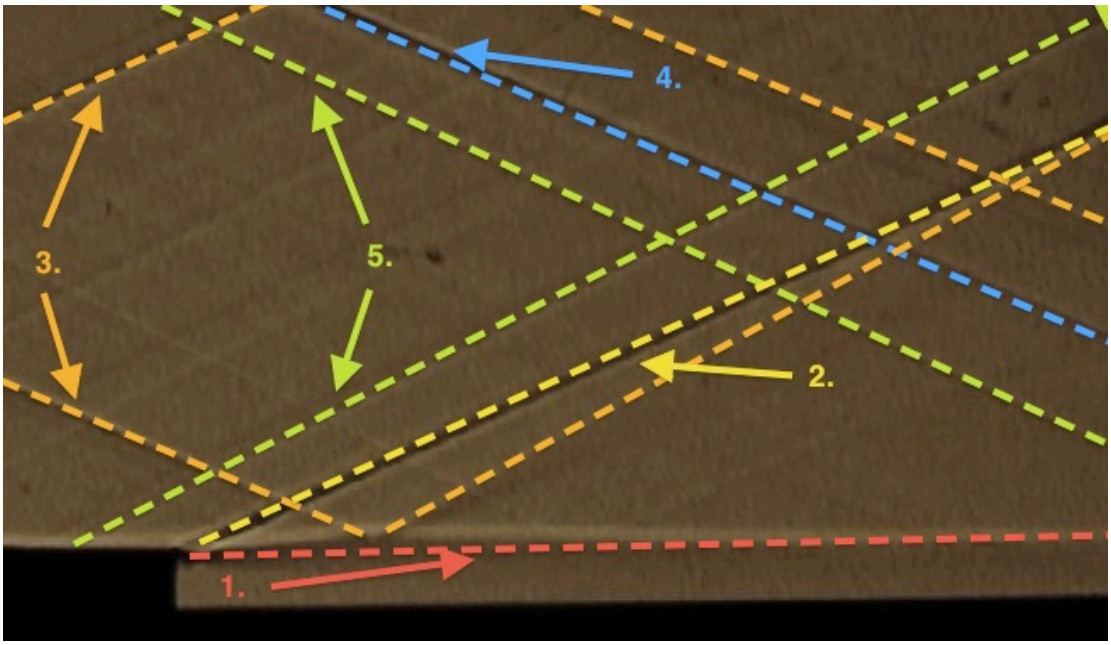

Figure 6.24: Important flow features for Test Case 2. These are: 1.) Shear layer 2.) Shock emanating from injection lip 3.) Shock waves from nozzle geometry 4.) Shock wave emanating from start of upper wall test section 5.) Shock wave emanating from end of nozzle.

Unlike the previous two test cases, the image analysis code was able to identify every important flow feature in at least some of the frames. Figure 6.25 shows the features that were identified in the reference image. This image was chosen as the reference because the code could detect all 5 major flow features. The only unnecessary line feature identified in the reference image was the lower wall. This value was discarded. The average angle and standard deviation of each feature is reported in Table 6.7. The results again show that all flow features are steady during the duration of the experiment. The lip shock does show some minor fluctuation, with a standard deviation of 0.77°. This is still very minor and changes the impingement point on the upper wall by less than a single slot height.

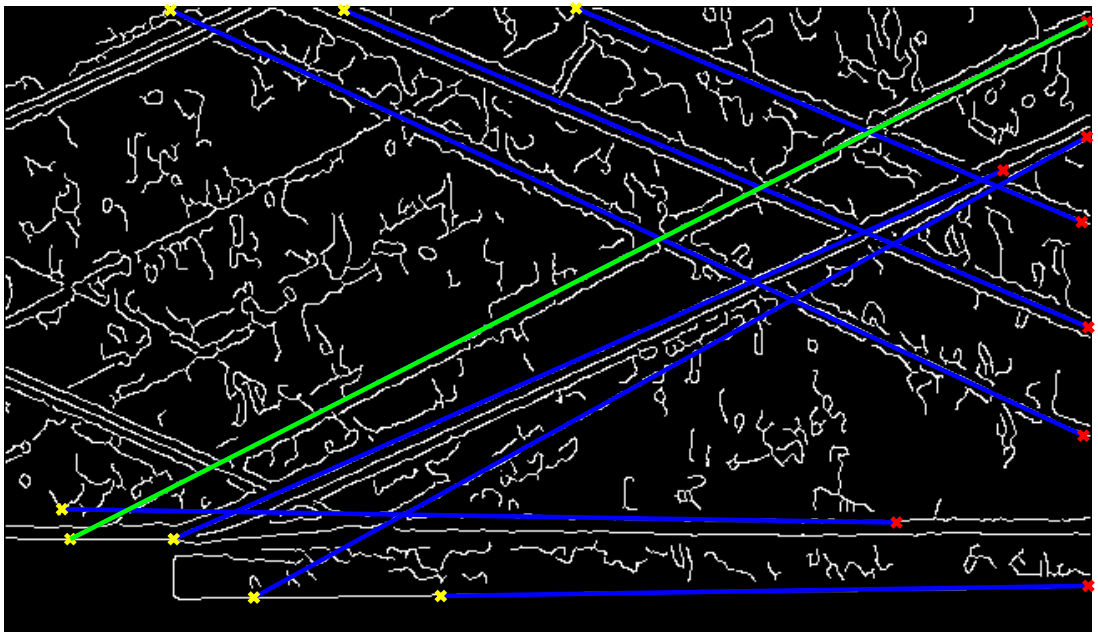

Figure 6.25: Sample schlieren image showing detected line features in flow for Test Case 2. Blue lines indicate detected features. Green indicates longest flow feature.

Table 6.7: Summary of results from automated schlieren image analysis for Test Case 2.

Feature	Mean Angle	Random Error	Standard Deviation	Number of Frames (Max: 72)
Shear Layer	0.78°	0.0276°	0.0938°	48
Lip Shock	155.49°	0.1667°	0.7707°	72
Throat Shock (Upper)	23°	0.0660°	0.1387°	34
Throat Shock (Lower)	150.49°	0.0423°	0.1135°	30
Upper Wall Start	23.07°	0.0223°	0.0933°	72
Nozzle End Shock (Upper)	24.86°	0.0137°	0.0565°	71
Nozzle End Shock (Lower)	152.9°	0.005°	0.0211°	72

6.3.2: Heat Flux Measurements

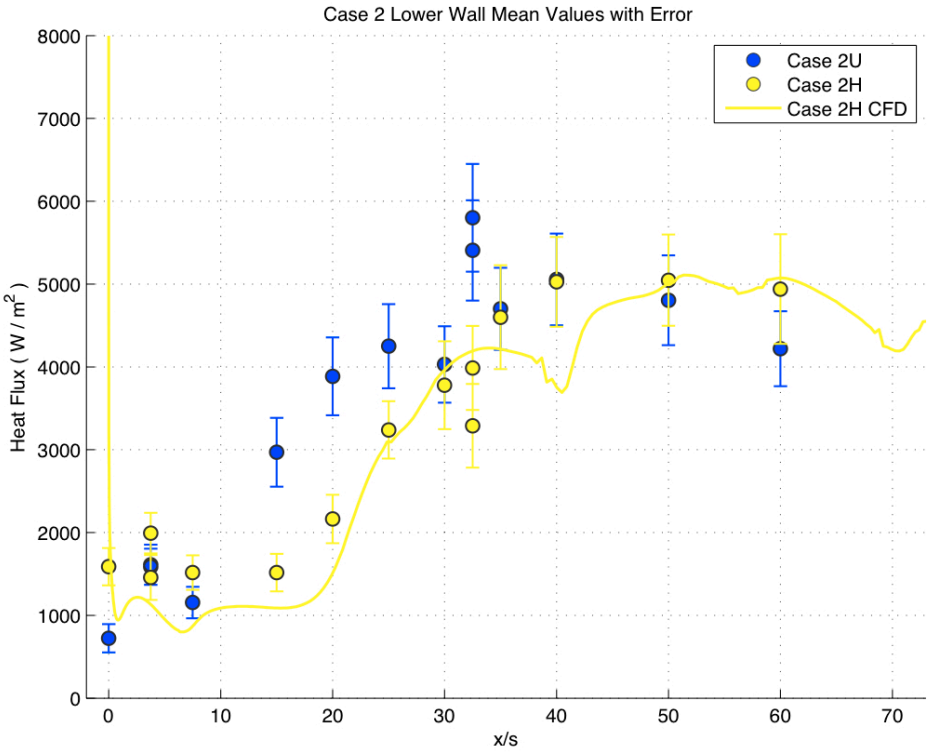

Figure 6.26: Case 2 Lower wall heat flux. Blue markers indicate average of 14 unheated experiments (Case 2LU). Yellow markers indicate average of 10 heated experiments (Case 2LH). Error bars give total uncertainty. Solid line indicates numerical simulations from LOCI-CHEM simulations.

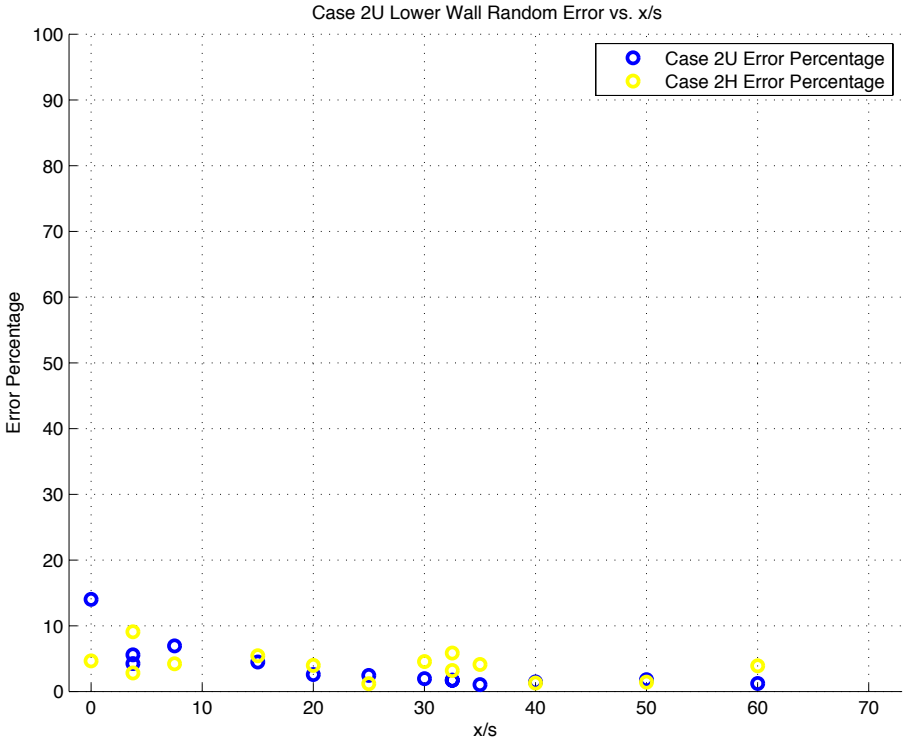

Figure 6.27: Random error vs. x/s location for Test Case 2. Blue markers indicate Case 2 LU. Yellow markers indicate Case 2 LH.

Figure 6.26 shows the heat flux along the lower wall for the Mach 0.73 film injection case. Numerical predictions from Dellimore's LOCI-CHEM simulations [5] are overlaid to allow comparison with the heated test results (Case 2LH). In comparison to Test Case 1, it can be seen that the protection provided by the film is greatly increased for both the heated and unheated films. Case 2LU and Case 2LH both exhibit a gradual rise in heat flux after $x/s = 15$ rather than the sudden rise that was visible for Test Case 0LU and Test Case 1LU. The gradual rise in heat flux leads to a peak occurring at $x/s = 32.5$ for Case 1LU and $x/s = 40$ for Case 1LH. This is a deviation from the expected behavior, in which the film provides similar protection until the impingement of the shear layer on the lower wall. The major differences between the numerical solution and the experimental results again occur at the film injection point. LOCI-CHEM predicts lower heat flux for the first 15 slot heights downstream of the film injection point. The trends in the CFD projection are very similar to those observed in the heated experimental data (Case 2LH), matching closely beyond the film injection region ($x/s > 15$). Figure 6.27 shows the random error plotted against axial location. There is very little variability anywhere in the test region. The random error for both test cases is below 15 % for the entire test region, indicating consistent measurements from run to run.

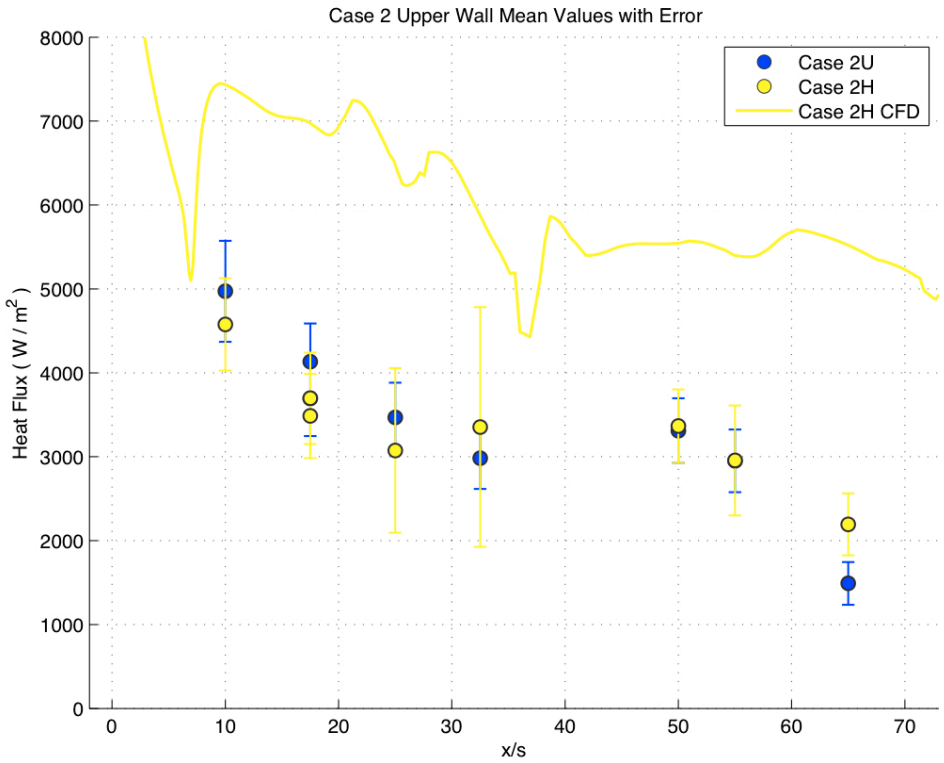

Figure 6.28: Case 2 Upper wall heat flux. Blue markers indicate average of 10 unheated experiments (Case 2UU). Yellow markers indicate average of 10 heated experiments (Case 2UH). Error bars give total uncertainty. Solid line indicates numerical simulations from LOCI-CHEM simulations.

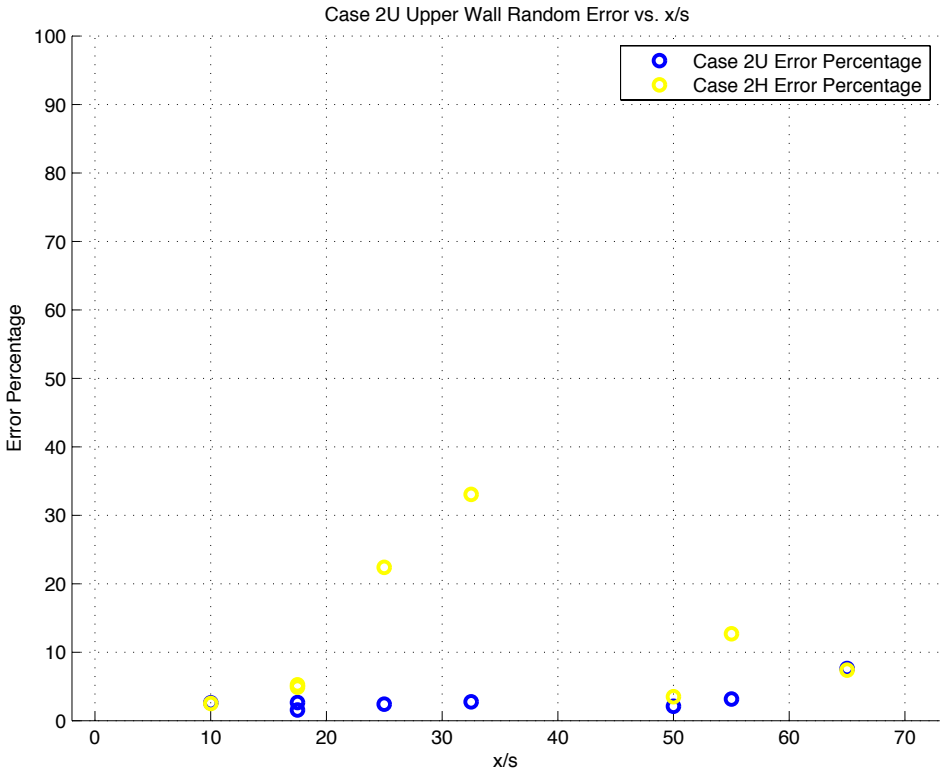

Figure 6.29: Random error vs. x/s location for Test Case 2. Blue markers indicate Case 2 UU. Yellow markers indicate Case 2 UH.

Figure 6.28 shows the heat flux distribution along the upper wall for the Mach 0.73 film injection case. As seen with the previous two test cases, the CFD prediction seems to capture the general trend but does not accurately predict the actual heat flux values seen in the experiment. The random error (Figure 6.29) again shows significant difference between Case 2UU and Case 2UH. For Case 2UU, there is little variability between test runs and the random error is less than 10% throughout the test section. Case 2UH has a significantly higher random error in the middle of the test section (x/s = 25 and 32.5). The fluctuation in this region is likely caused by the interaction of 3 separate shockwaves with the shear layer on the upper wall between $25 < x/s < 30$ (see section 6.3.3).

6.3.3: Relation between Flow Structures and Heat Flux Distribution

The results of the schlieren image analysis code were used to produce a shock diagram that shows the impingement points for the major flow features throughout the test section. All significant flow features were detected for this test case (refer to Table 6.7). Figure 6.30 shows the generated shock diagram superimposed between the upper and lower wall heat flux results. The shock impingements on the upper wall at x/s = 25.7, 28.7, 29.75 and 55.3 seen in the diagram all correspond with changes in the heat flux plot. There is no shockwave to explain the sudden decrease in heat flux at x/s = 42. The lower wall heat flux plot also shows fluctuations at the impingement locations of x/s = 25.7, 36.5 and 55.3. The most significant of these is the change at x/s = 36.5. The CFD solution predicts a large drop in heat flux, but the experimental values do not reflect this.

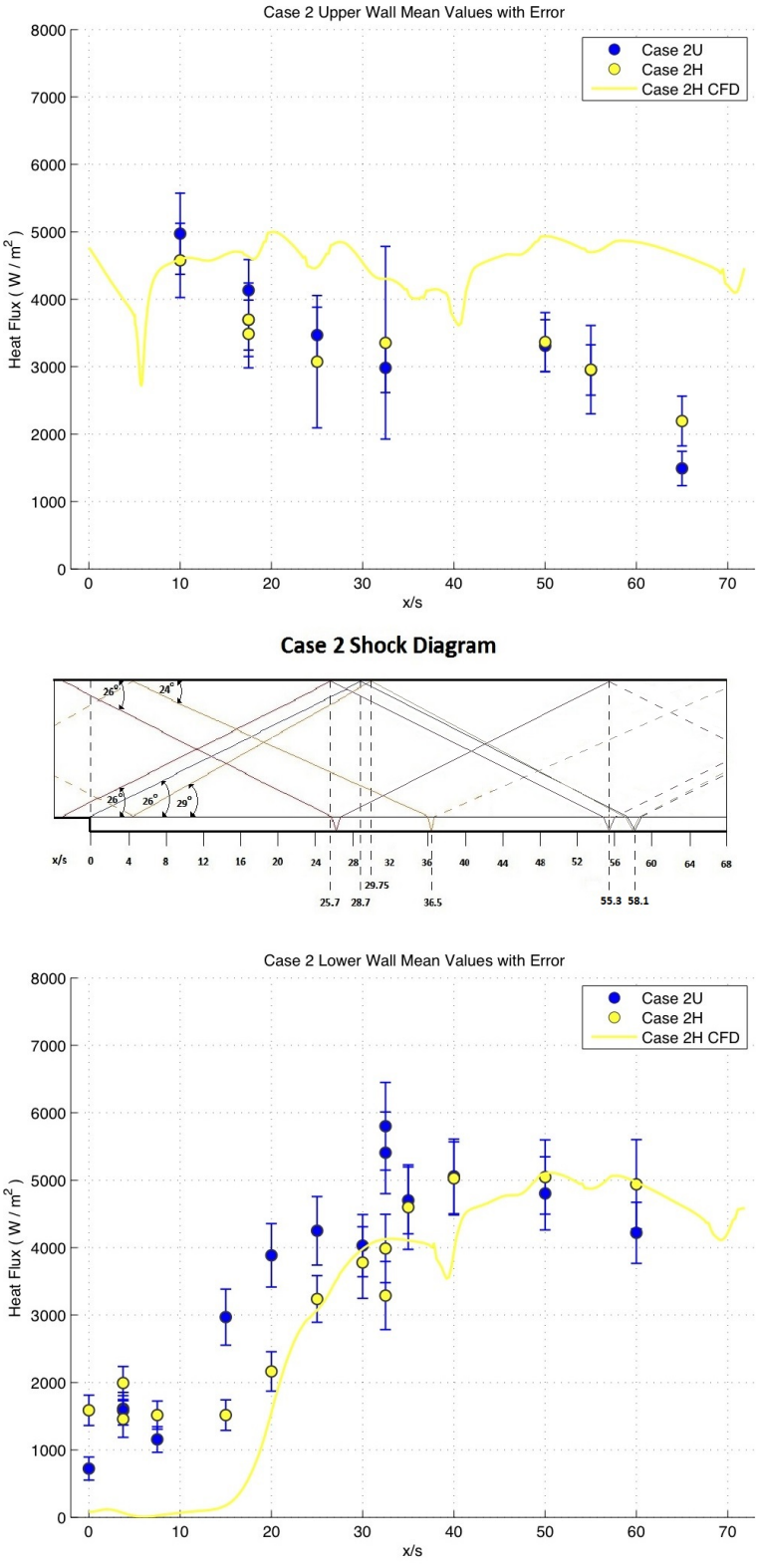

Figure 6.30: Top: Heat flux results for Test Case 2. Middle: Shock diagram generated using image analysis code. Bottom: Heat flux results for Test Case 2. All results are presented on the same axial scale.

6.3.4: Comparison to CFD

Film cooling effectiveness is calculated in the same manner as for Test Case 1H (see Figure 6.31). Again, the area directly after the film injection louver is well protected for both test cases. Surprisingly, Case 2LU has a higher effectiveness near the film injection louver. Both cases have an effectiveness above 50% for all points near the injection region ($x/s < 15$). The effectiveness for both cases displays a gradual decrease in the film cooling effectiveness, dropping to approximately 10 % before $x/s = 35$. The average effectiveness is 21.1 % for Case 2LU and 32.43 % for Case 2LH. These are both increases over the results from Test Case 1. In comparison to the CFD prediction, LOCI-CHEM predicts an average effectiveness of 47.35 % and overestimates the effectiveness every location. The difference is again most pronounced near the film injection point, with the numerical simulation predicting above 50% efficiency up to $x/s = 25$. The general trend predicted by the CFD closely matches the trend of decreasing effectiveness seen in the experimental results.

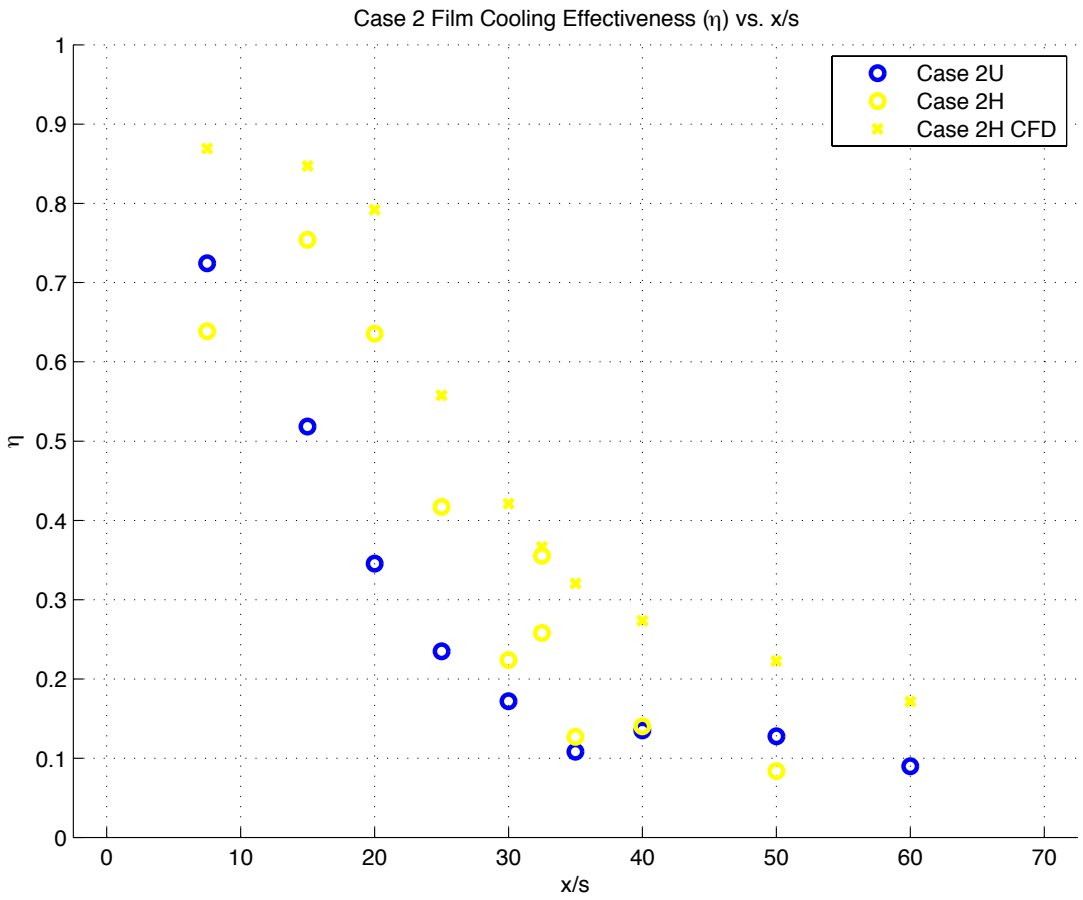

Figure 6.31: Film Cooling Effectiveness plot for Test Case 2. Blue markers indicate unheated film injection (Case 2LU). Yellow markers indicate heated film injection (Case 2LH). 'X' markers indicate numerical simulation from LOCI-CHEM software.

Figure 6.32 shows Ω plotted against axial location. As was seen in Test Case 1, the individual Ω_i values do not exhibit a large amount of scatter anywhere in the test region for the lower wall. This indicates there is very little variability at any specific axial location. This confirms what was seen in the random error analysis, where none of the *x/s* locations on the lower wall had a random error greater than 15 %. The upper wall shows slightly more variability after *x/s* = 15, but the spread of the Ω_i values is much narrower than what was seen in the previous two test cases.

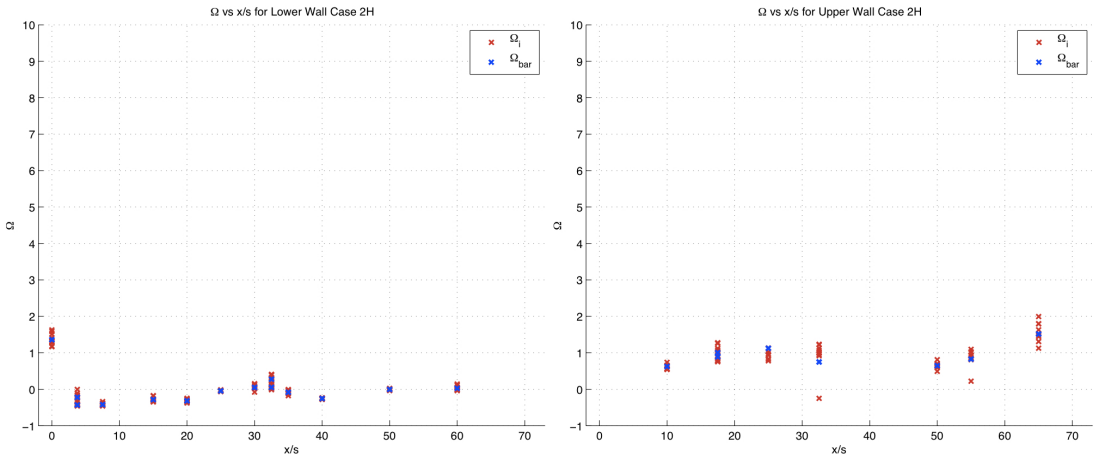

Figure 6.32: Ω_l and Ω_{bar} vs. x/s location for Test Case 2. Red x's indicate individual Ω_l values. Blue x's indicate Ω_{bar} values. Left: Lower wall. Right: Upper wall.

The Ω values for Case 2LH and Case 2UH are -0.02 and 0.92 respectively. This indicates a very close agreement between the CFD results and experimental values on the lower wall. The upper wall results do not show significant agreement. The CFD under-predicts the value of heat flux on lower wall and over-predicts the heat flux on the upper wall. Neglecting the film injection region ($x/s < 15$) on the lower wall does not improve the agreement between the numerical solution and experimental values for this test case. The value of Ω decreases to -0.09 (see Figure 6.33) with the exclusion of the area near the louver.

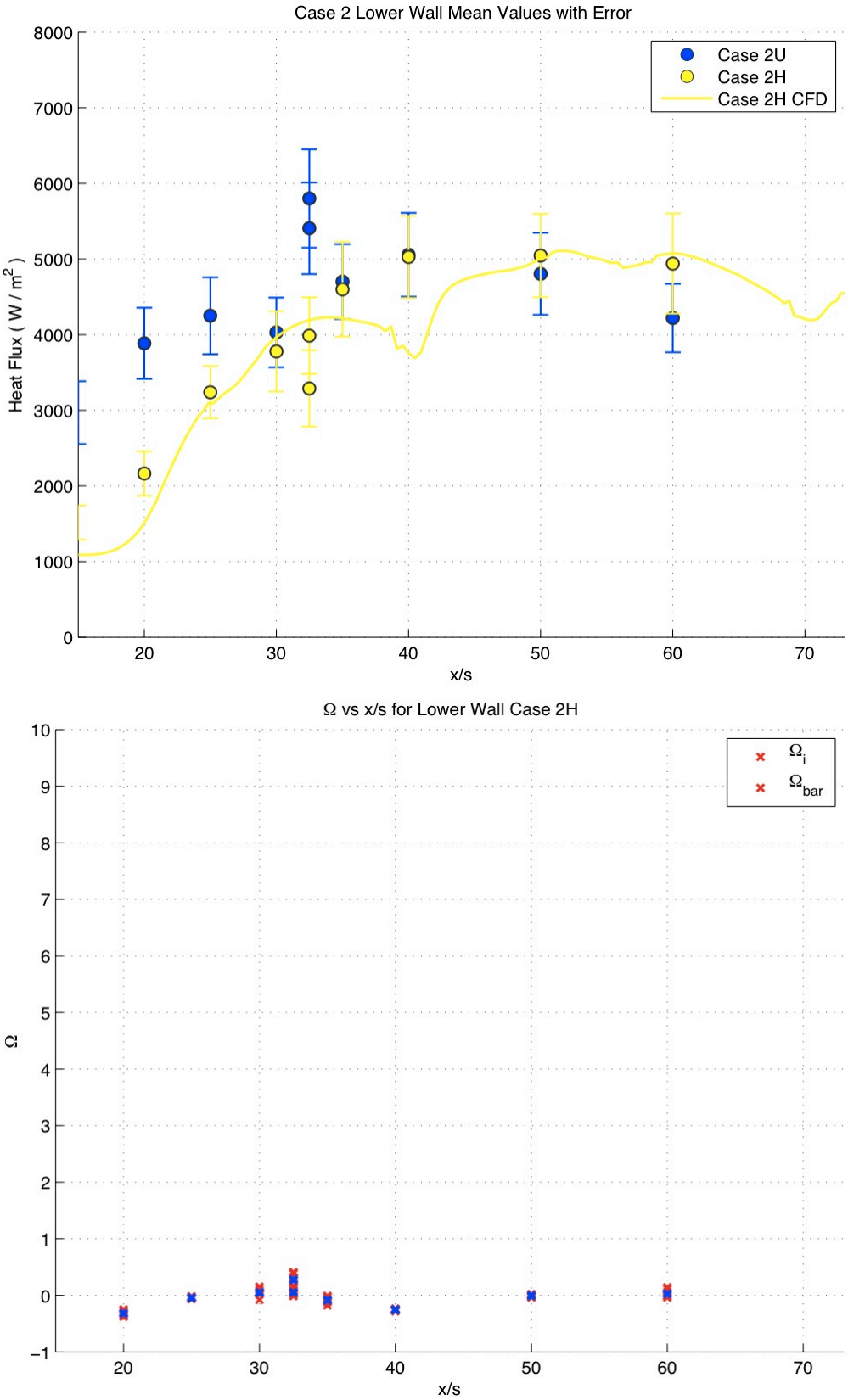

Figure 6.33: Test Case 2LH. Upper: Plot of heat flux vs. x/s for x/s > 15. Lower: Plot of Ω for x/s > 15.

6.3.5: Test Case 2 Summary Table

Table 6.8: Test Case 2UU and 2LU summary table

$T_{ambient}$	295 K
$P_{ambient}$	0.99 atm
T_{film}	295 K
P_{film}	0.09013 atm
Film throttle valve setting	Partially Open (~20 %)
Burner inlet valve setting	Closed
Ω (Upper Wall)	N/A
Ω (Lower Wall)	N/A
Average Heat Flux (Upper Wall)	3375 W/m^2
Average Heat Flux (Lower Wall)	3586 W/m^2
Peak Heat Flux (Upper Wall)	4971 W/m^2
Location of Peak Heat Flux (Upper Wall)	*x/s* = 10
Peak Heat Flux (Lower Wall)	5800 W/m^2
Location of Peak Heat Flux (Lower Wall)	*x/s* = 40
Average Effectiveness	0.2106 (21.06 %)
Peak Effectiveness	0.72.44 (72.44 %)
Locations of Peak Effectiveness	*x/s* = 7.5
Number of Schlieren Images	72

Table 6.9: Test Case 2UH and 2LH summary table

$T_{ambient}$	295 K
$P_{ambient}$	0.98 atm
T_{film}	330 K
P_{film}	0.10498 atm
Film throttle valve setting	Partially Open (~20 %)
Burner inlet valve setting	Partially Open (~15 %)
Ω (Upper Wall)	0.4372
Ω (Lower Wall)	- 0.3588
Average Heat Flux (Upper Wall)	3338 W/m^2
Average Heat Flux (Lower Wall)	3153 W/m^2
Peak Heat Flux (Upper Wall)	4576 W/m^2
Location of Peak Heat Flux (Upper Wall)	*x/s* = 10
Peak Heat Flux (Lower Wall)	5047 W/m^2
Location of Peak Heat Flux (Lower Wall)	*x/s* = 50
Average Effectiveness	0.3242 (32.42 %)
Peak Effectiveness	0.7539 (75.39 %)
Locations of Peak Effectiveness	15
Number of Schlieren Images	72

6.4: Test Case 3

Test Case 3 is the Mach 1.20 film injection case. The film-throttling valve in the intake pipe was opened to allow the formation of supersonic film flow in the test section. Measurements were made with both a heated and unheated film (Test Case 3H and Test Case 3U respectively). This case is significantly different than the previous cases in that the film flow through the test section is supersonic. This greatly reduces the convective Mach number and decreases the shear layer growth rate. This test case provides an environment in which to study how a supersonic film's behavior differs from that of a subsonic film. This is of great importance due to the fact that the film flow in the J-2X engine and many other rocket engines is supersonic. Comparing the predictions of LOCI-CHEM to experimental data for high-speed film flows is one of the primary objectives of this study. Case 3UU plots present the average of 10 experiments and Case 3LU plots present the average of 14 experiments. Case 3UH and Case 3LH plots present the average of 10 experiments.

6.4.1: Schlieren Image Analysis

Figure 6.34: Sample schlieren image for Test Case 23

Figure 6.34 shows a sample schlieren image for Test Case 3. This image was extracted from a schlieren video taken during one of the experiments and was used as the reference image for Test Case 3 in the image analysis code. The area near the film injection slot is particularly complex for Test Case 3. The presence of a supersonic film adds several flow features below the developing shear layer. Figure 6.35 shows a detailed diagram of the important flow phenomena in the film injection region. The boundary layers present on the upper and lower sections of the film louver turn toward each other as they move past the louver exit. In order to do so, they pass through expansion fans. When these flows meet, they must again turn and pass through expansion fans. These fans coalesce into oblique shocks. The oblique shock that forms on the lower part of the shear layer is reflected off of the wall and passes through the shear layer. As it passes through the shear layer, it is turned and passes into the core flow.

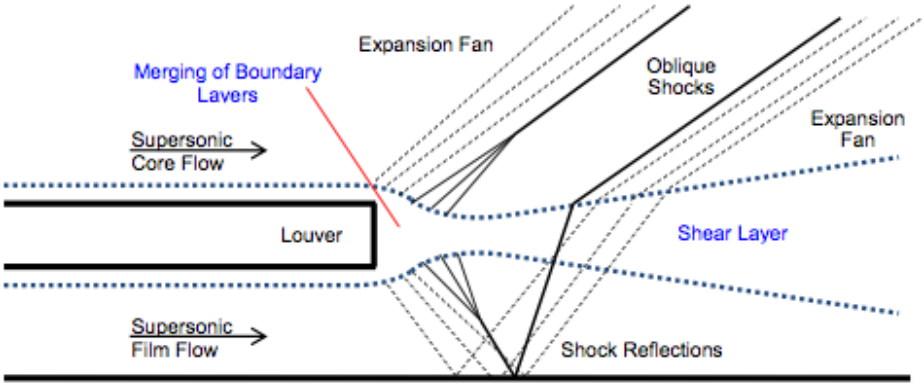

Figure 6.35: Flow features at the exit of film louver {Adapted from Maqbool [6] (2012)}.

Figure 6.36 shows six flow features that are important to the film cooling results. These first five structures are the same as those from the previous test cases but an additional structure is present in the film flow. This feature is the expansion fan that emanates downward from the film louver. When it hits the lower wall, it is reflected back as a shockwave and passes through the shear layer where it is turned downstream.

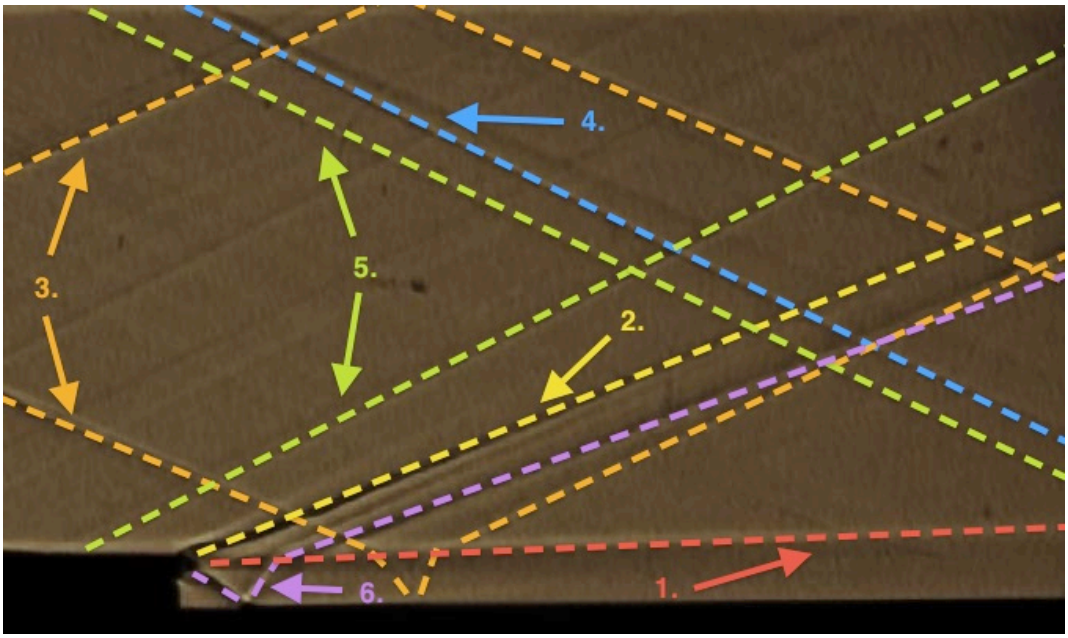

Figure 6.36: Important flow features for Test Case 3. These are: 1.) Shear layer 2.) Shock emanating from injection lip 3.) Shock waves from nozzle geometry 4.) Shock wave emanating from start of upper wall test section 5.) Shock wave emanating from end of nozzle 6.) Expansion fan and reflected shock emanating from film injection lip

The image analysis code was again able to identify every important flow feature in at least some of the frames. Figure 6.37 shows the features that were identified in the reference image. This image was chosen as the reference because the code could detect all 6 major flow features. The only unnecessary line feature identified in the reference image was a line artifact at the top of the imaging area. This value was discarded. The average angle and standard deviation of each feature is reported in Table 6.10. The results again show that all flow features are steady during the duration of the experiment. No single flow feature has a standard deviation greater than 0.31° during the duration of the experiment.

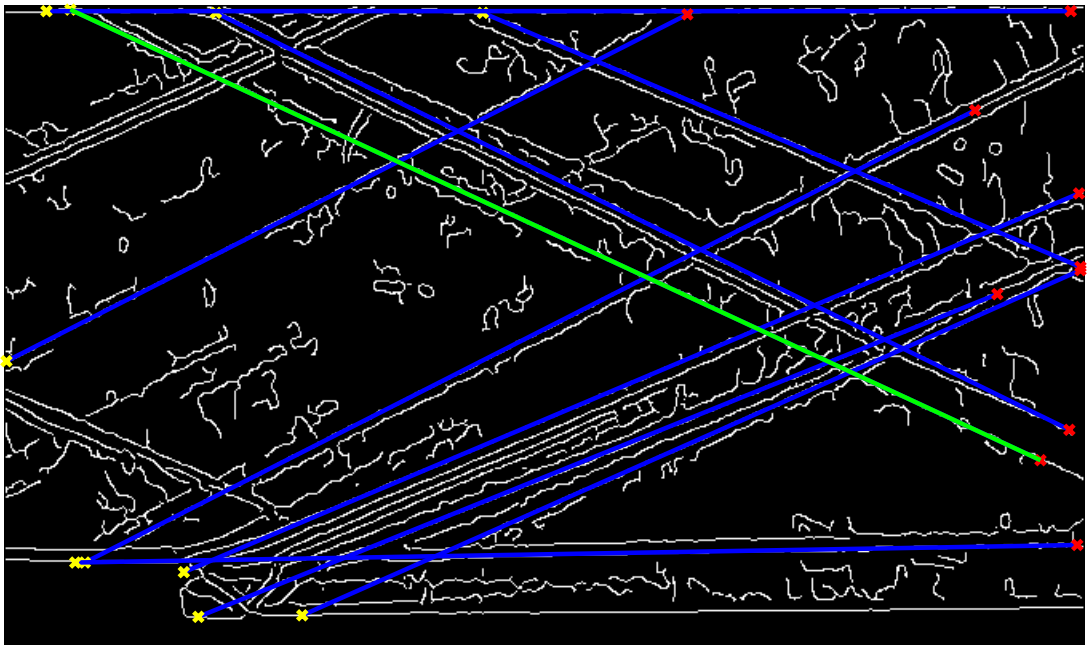

Figure 6.37: Sample schlieren image showing detected line features in flow for Test Case 3. Blue lines indicate detected features. Green indicates longest flow feature.

Table 6.10: Summary of results from automated schlieren image analysis for Test Case 3.

Feature	Mean Angle	Random Error	Standard Deviation	Number of Frames (Max: 72)
Shear Layer	178.88°	0.0218°	0.0741°	48
Lip Shock	157.34°	0.0555°	0.2159°	63
Throat Shock (Upper)	23.05°	0.1430°	0.3135°	20
Throat Shock (Lower)	152.25°	0.0386°	0.0535°	64
Upper Wall Start	24.94°	0.0373°	0.0951°	27
Nozzle End Shock (Upper)	23.21°	0.0115°	0.0431°	58
Nozzle End Shock (Lower)	153.09°	0.0116°	0.0484°	72
Reflected Expansion Fan Shock	157.91°	0.0718°	0.2815°	64

6.4.2: Heat Flux Measurements

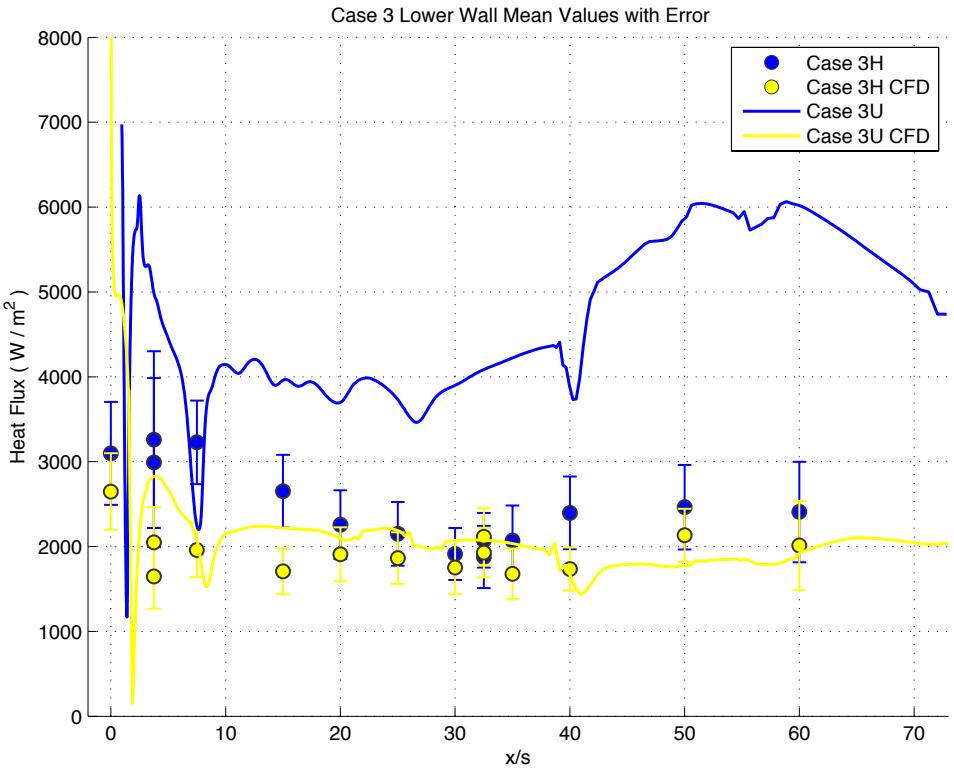

Figure 6.38: Case 3 Lower wall heat flux. Blue markers indicate average of 13 unheated experiments (Case 3LU). Yellow markers indicate average of 10 heated experiments (Case 3LH). Error bars give total uncertainty. Solid lines indicate numerical simulations from LOCI-CHEM simulations.

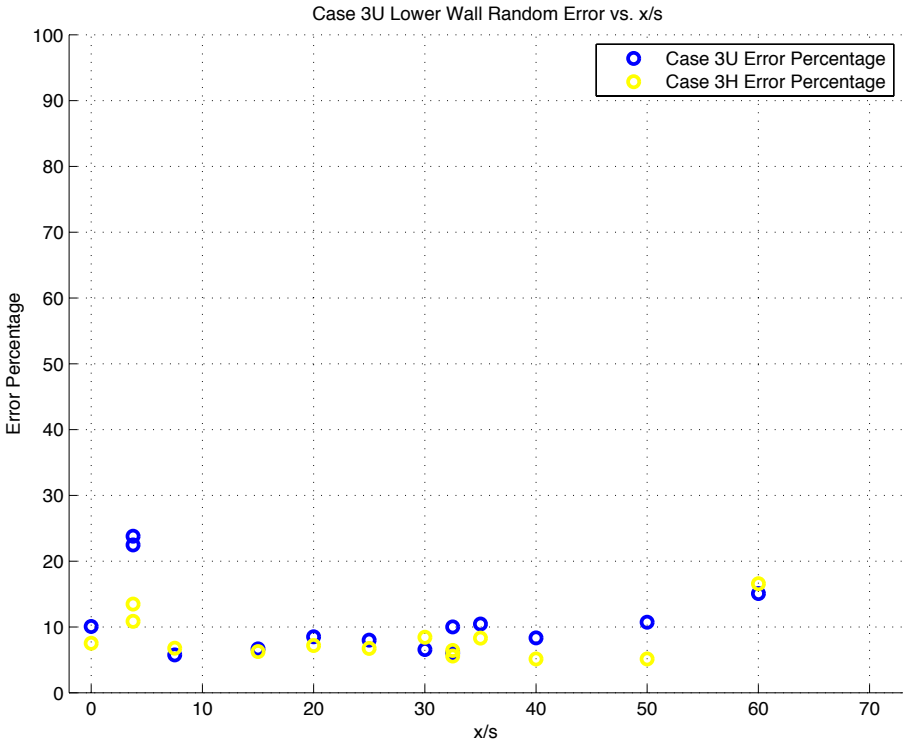

Figure 6.39: Random error vs. x/s location for Test Case 3. Blue markers indicate Case 3LU. Yellow markers indicate Case 3LH.

Figure 6.38 shows the heat flux along the lower wall for the Mach 1.20 film injection case. Numerical predictions for Case 3LH from Dellimore's LOCI-CHEM simulations [5] are overlaid to allow comparison with the heated test results. Additionally, unheated film CFD (Case 3LU) obtained from NASA is overlaid for comparison with the unheated test results. It can be seen from the comparison with the experimental results that the prediction by LOCI-CHEM again greatly over-predicts the heat flux for the unheated film injection (Case 3LU). There is no visible heat flux spike in the experimental data, indicating that the film protection layer does not break in the investigation window. A similar trend is again evident between the experimental data and CFD, with an initial rise in heat flux, followed by a gradual decrease and rise toward the end of the test section. However, LOCI-CHEM greatly

over-predicts the heat flux values throughout the test section, particularly after *x/s = 40*. Case 3LH again shows reasonable agreement between experimental data and CFD predictions. As was seen in the previous cases, the numerical simulations over-predict the wall heat flux throughout most of the test section, including the injection region. Figure 6.39 shows the random error plotted against axial location. Again, there is very little variability anywhere in the test region. The random error for both test cases is below 10 % for the majority of the test region, indicating consistent measurements from run to run.

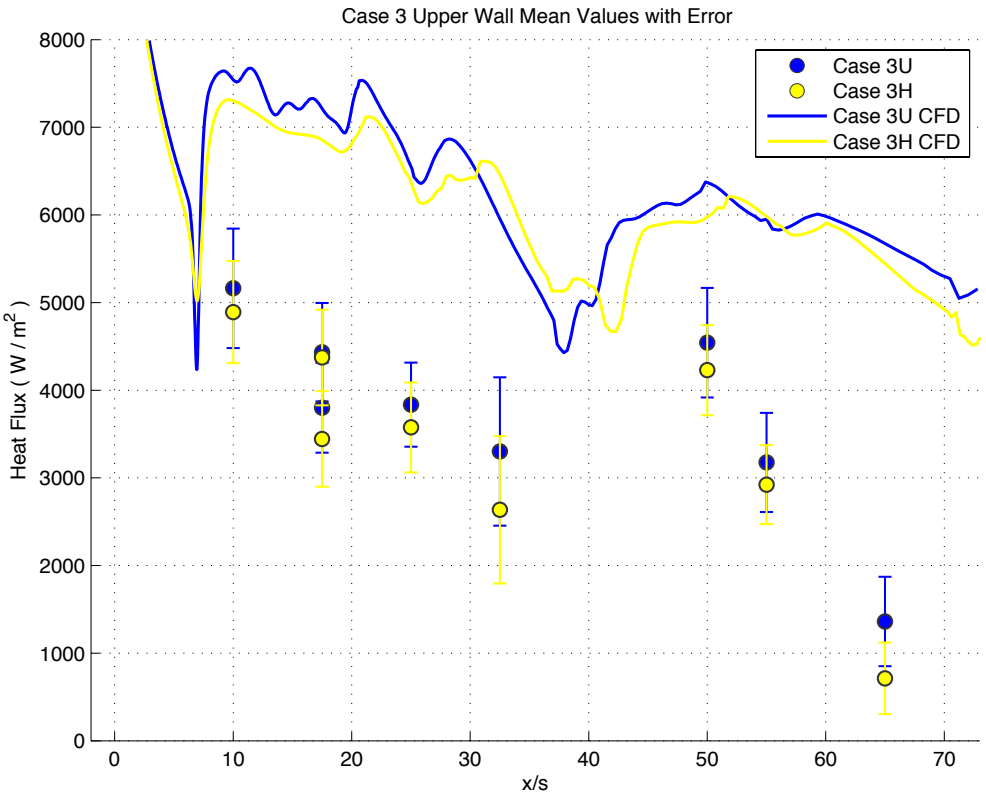

Figure 6.40: Case 3 Upper wall heat flux. Blue markers indicate average of 10 unheated experiments (Case 3UU). Yellow markers indicate average of 10 heated experiments (Case 3UH). Error bars give total uncertainty. Solid line indicates numerical simulations from LOCI-CHEM simulations.

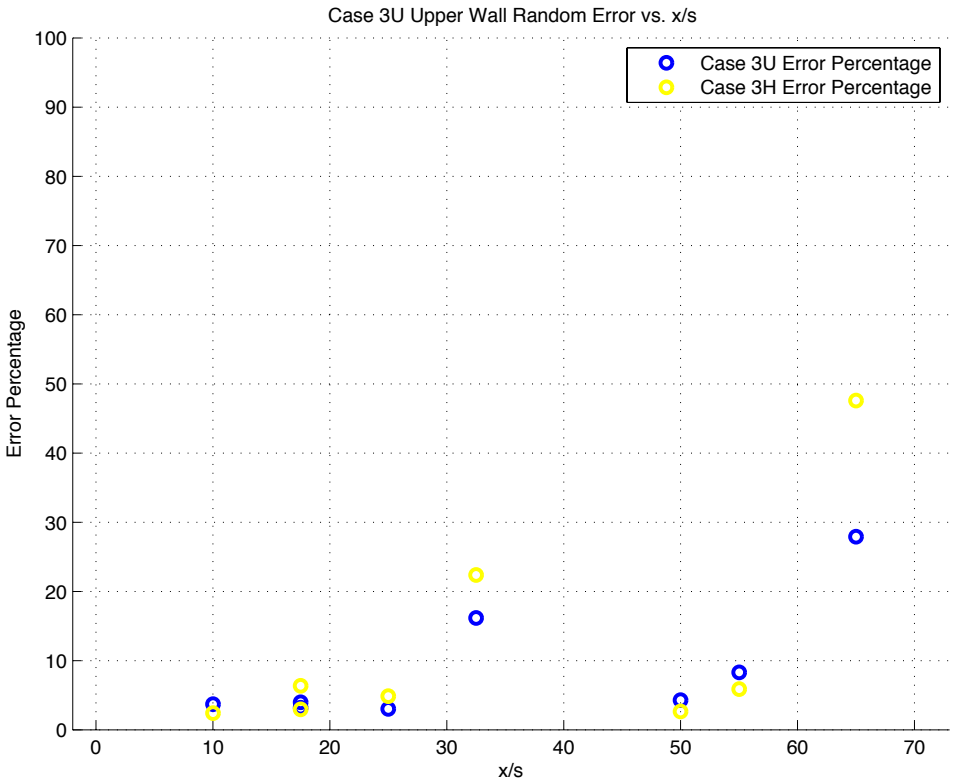

Figure 6.41: Random error vs. x/s location for Test Case 3. Blue markers indicate Case 3UU. Yellow markers indicate Case 3UH.

Figure 6.40 shows the heat flux distribution along the upper wall for the Mach 1.20 film injection case. The CFD prediction does not seem to capture the general trend or predict the heat flux values with any accuracy. The difference is particularly stark beyond $x/s = 50$. The random error (Figure 6.41) seems to indicate that there is little variability except at $x/s = 32.5$ and $x/s = 65$. Both of these locations are near shock impingement locations (see section 6.4.3). These impingements can cause significant variability at those locations from run to run. Except for the two locations noted, the random error is less than 10% throughout the test section.

6.4.3: Relation between Flow Structures and Heat Flux Distribution

The results of the schlieren image analysis code were used to produce a shock diagram that shows the impingement points for the major flow features throughout

the test section. All significant flow features were detected for this test case (refer to Table 6.10). Figure 6.42 shows the generated shock diagram superimposed between the upper and lower wall heat flux results. The shock impingements on the upper wall occur at x/s = 25.7, 34.7, 39.5 and 55.3. All of these locations correspond with changes in the numerical heat flux plot. The initial impingement point of the shockwave emanating from the nozzle contraction occurs around x/s = 5 and accounts for the sharp decrease seen in the CFD solution. The lower wall numerical heat flux solution also shows fluctuations at the impingement locations of x/s = 25.7, 36 and 55.3. The fluctuations near the injection region are caused by the expansion fan on the film louver and the impingement of the shockwave from the nozzle contraction. The CFD solution predicts a drop in heat flux in this region, and the experimental values also reflect this.

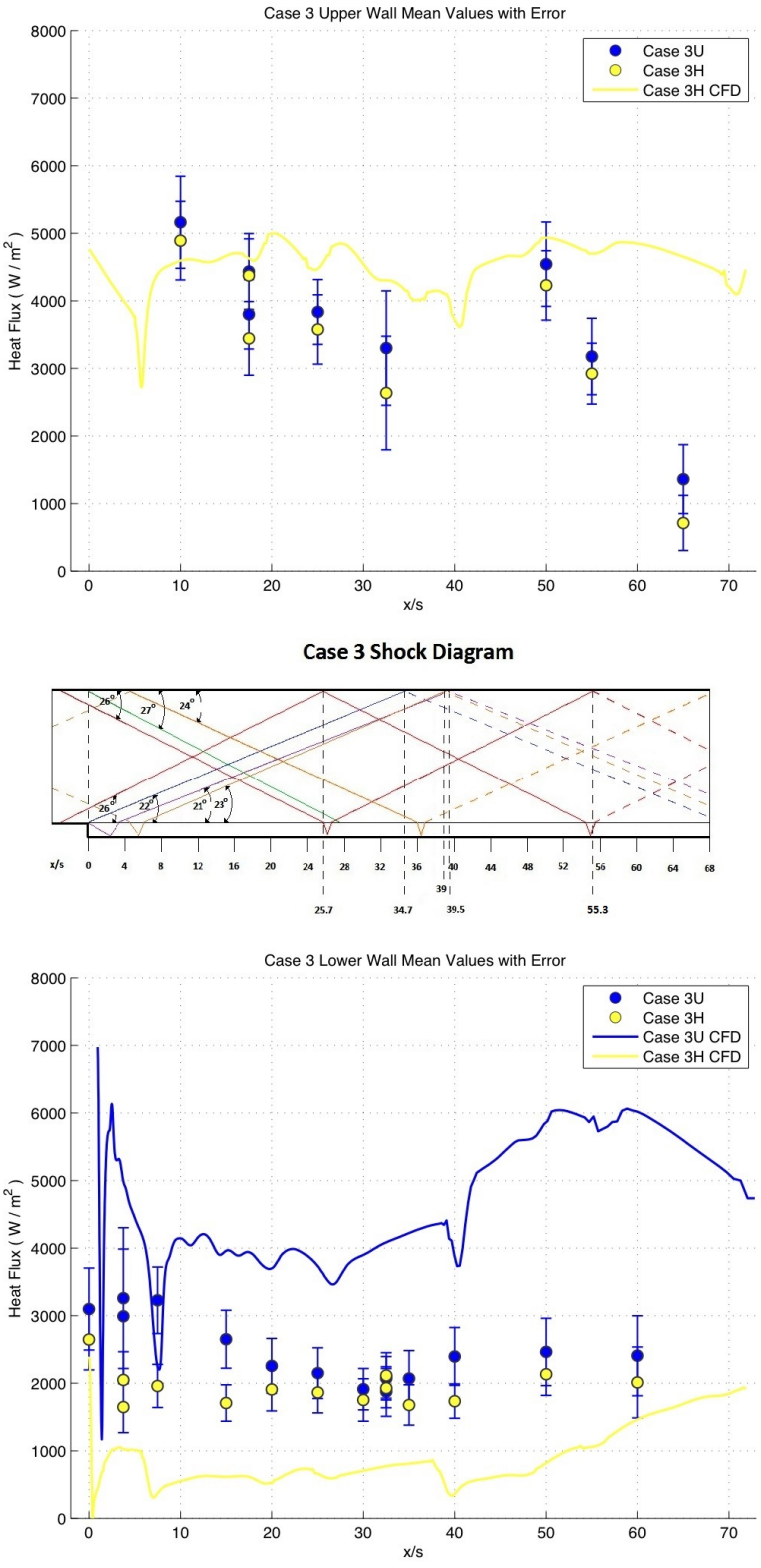

Figure 6.42: Top: Heat flux results for Test Case 3. Middle: Shock diagram generated using image analysis code. Bottom: Heat flux results for Test Case 3. All results are presented on the same axial scale.

6.4.4: Comparison to CFD

Film cooling effectiveness is calculated for Case 3LU and Case 3LH (see Figure 6.43). Unlike the previous two test cases, the area directly after the film injection louver is the worst protected for both test cases. Both cases exhibit less than 60% effectiveness near the film louver. The film provides more protection as axial location is increased. This is the opposite of expected result. Case 3LH exhibits an effectiveness greater than 50% for the entire test section. The same trend is visible for both test cases, with an initial increase and then a slow, steady decrease in effectiveness. The average effectiveness is 55.61 % for Case 3LU and 63.92 % for Case 3LH. These are large increases over the results from the previous test cases, which was expected. Loci-CHEM predicts an average effectiveness of 36.12 % for Case 3LU and 69.13 % for Case 3LH. The CFD predictions and their relation to the experimental results differ greatly between both cases. Loci-CHEM under-predicts the film cooling effectiveness everywhere but next to the film injection louver for Case 3LH and shows little correlation to the experiment trends beyond x/s = 32.5. The simulation data for Case 3LH matches closely with the experimental throughout the test region, with the largest disagreement occurring near the injection region.

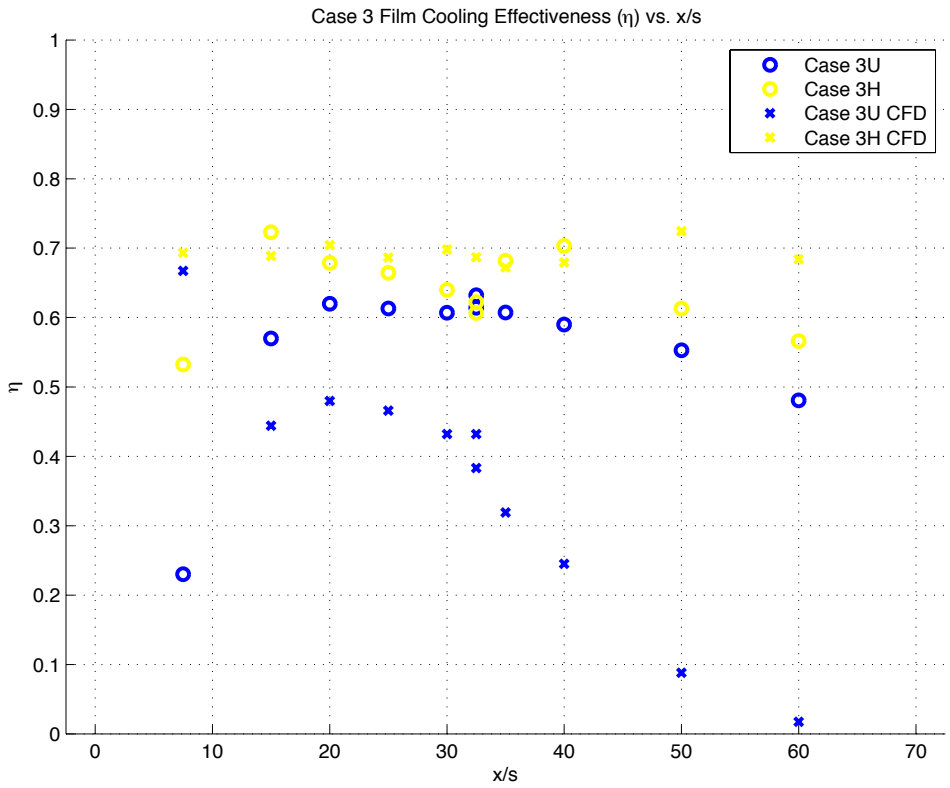

Figure 6.43: Film Cooling Effectiveness plot for Test Case 3. Blue markers indicate unheated film injection (Case 3LU). Yellow markers indicate heated film injection (Case 3LH). 'X' markers indicate numerical simulations from LOCI-CHEM software.

Figures 6.44 and 6.45 show Ω plotted against axial location for Case 3U and 3H respectively. The Ω_i values for Case 3U exhibit considerably more scatter on both the upper and lower walls than Case 3H. The variability seen in these results was not seen in the random error analysis, where results for both test cases were comparable. Overall, there is still little variability at any specific axial location. As has been the case for the last several test cases, the upper wall shows a lot of variability at x/s = 65.

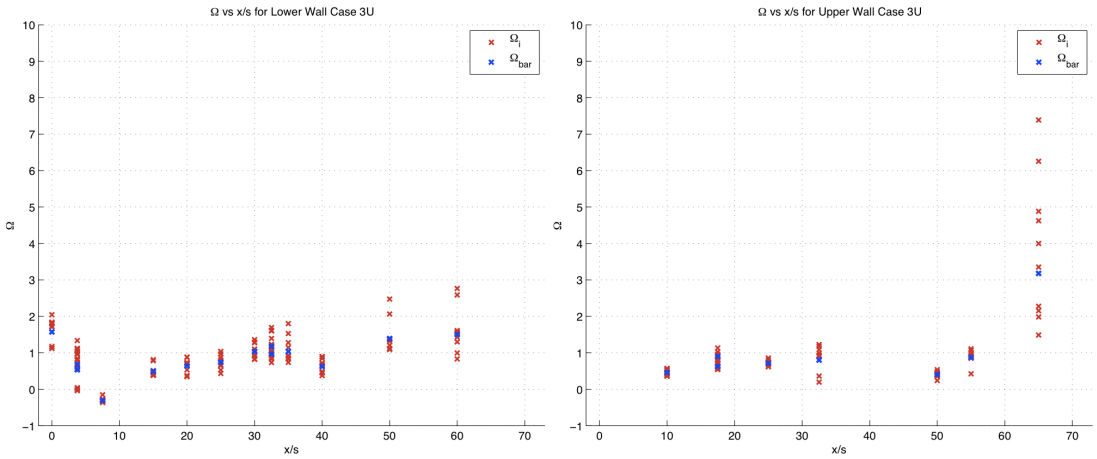

Figure 6.44: Ω_I and Ω_{bar} vs. x/s location for Test Case 3U. Red x's indicate individual Ω_I values. Blue x's indicate Ω_{bar} values. Left: Lower wall. Right: Upper wall.

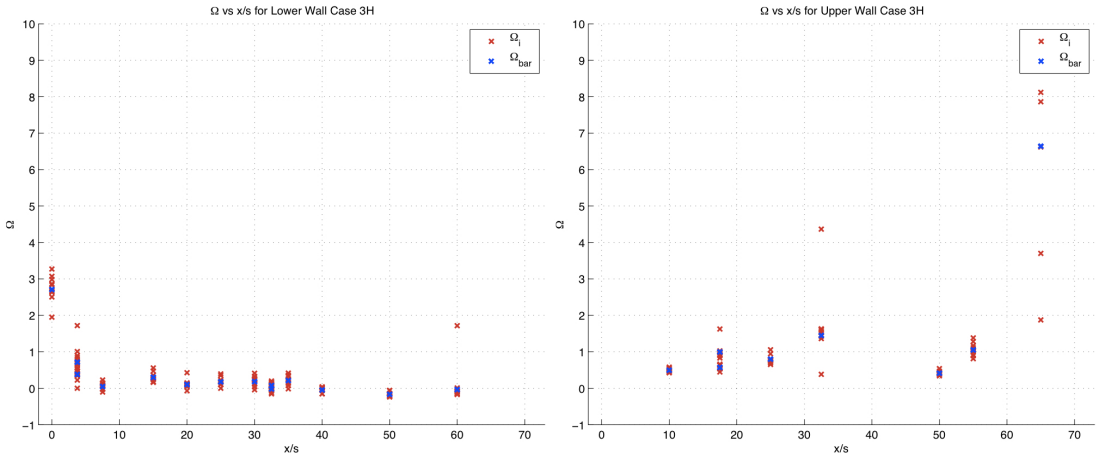

Figure 6.45: Ω_I and Ω_{bar} vs. x/s location for Test Case 3H. Red x's indicate individual Ω_I values. Blue x's indicate Ω_{bar} values. Left: Lower wall. Right: Upper wall.

The Ω values for Case 3LH and Case 3UH are 0.33 and 1.55 respectively. The Ω values for Case 3LU and Case 3UU are 0.86 and 0.99 respectively. These are worse than what was seen for Test Case 1 and Test Case 2. For both test cases, Loci-CHEM over-predicts the heat flux on both walls. Neglecting the film injection region (x/s < 15) on the lower wall again improves the agreement between the numerical solution and experimental values. . The value of Ω drops to 0.075 for Case 3LH and 0.84 for Case 3LU (see Figure 6.46).

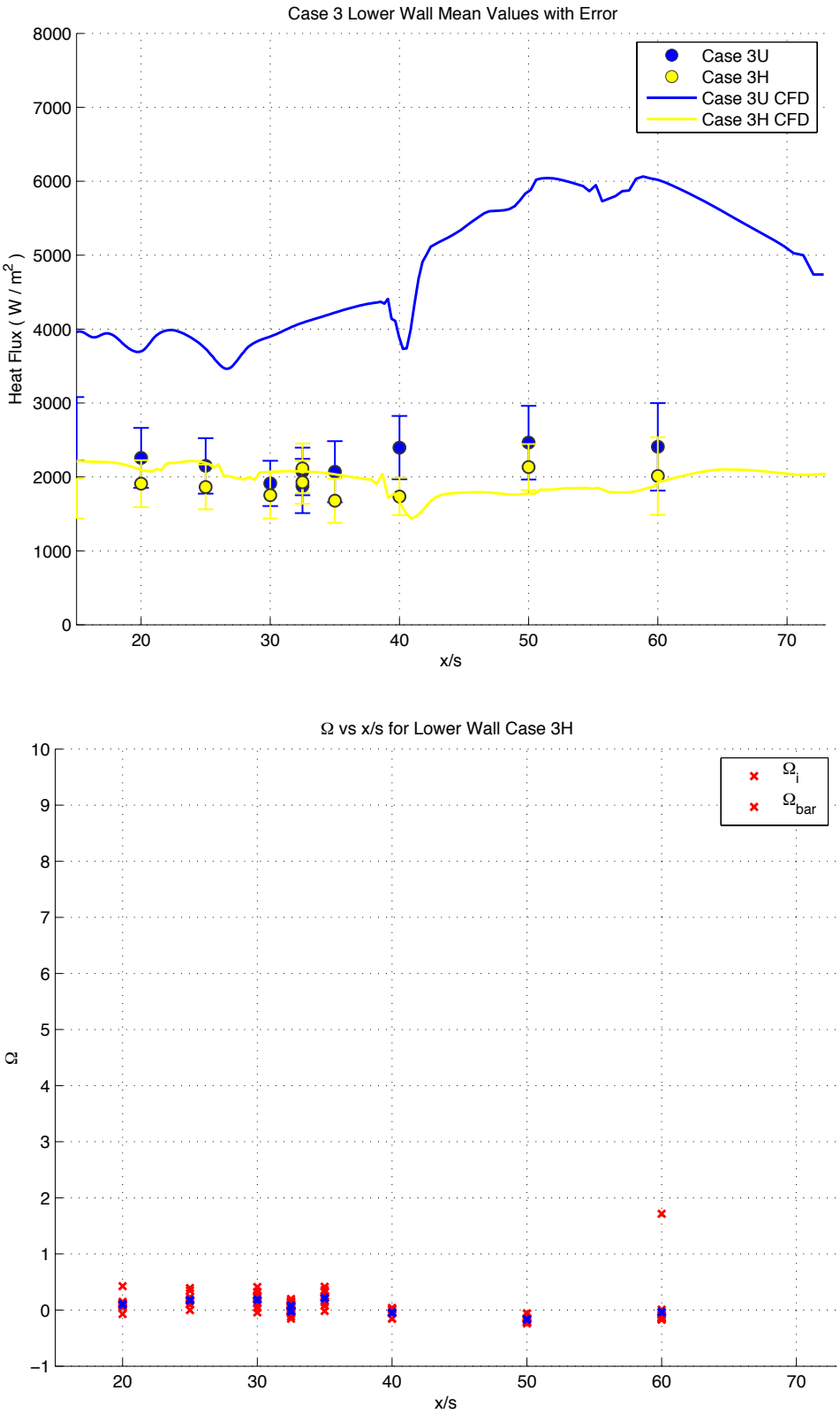

Figure 6.46: Test Case 3LH and 3UH. Upper: Plot of heat flux vs. x/s for x/s > 15. Lower: Plot of Ω for x/s > 15.

6.4.5: Test Case 3 Summary Table

Table 6.11: Test Case 3UU and 3LU summary table

$T_{ambient}$	295 K
$P_{ambient}$	0.99 atm
T_{film}	295 K
P_{film}	0.21376 atm
Film throttle valve setting	Partially Open (~40 %)
Burner inlet valve setting	Closed
Ω (Upper Wall)	0.995
Ω (Lower Wall)	0.8622
Average Heat Flux (Upper Wall)	2488 W/m^2
Average Heat Flux (Lower Wall)	3702 W/m^2
Peak Heat Flux (Upper Wall)	5163 W/m^2
Location of Peak Heat Flux (Upper Wall)	*x/s* = 10
Peak Heat Flux (Lower Wall)	3259 W/m^2
Location of Peak Heat Flux (Lower Wall)	*x/s* = 2.5
Average Effectiveness	0.5561 (55.61 %)
Peak Effectiveness	0.6198 (61.98 %)
Locations of Peak Effectiveness	*x/s* = 32.5
Number of Schlieren Images	72

Table 6.12: Test Case 3UH and 3LH summary table

$T_{ambient}$	295 K
$P_{ambient}$	0.98 atm
T_{film}	330 K
P_{film}	0.27752 atm
Film throttle valve setting	Partially Open (~40 %)
Burner inlet valve setting	Partially Open (~25 %)
Ω (Upper Wall)	0.9751
Ω (Lower Wall)	- 0.5584
Average Heat Flux (Upper Wall)	3348 W/m^2
Average Heat Flux (Lower Wall)	1938 W/m^2
Peak Heat Flux (Upper Wall)	4891W/m^2
Location of Peak Heat Flux (Upper Wall)	*x/s* = 10
Peak Heat Flux (Lower Wall)	2648 W/m^2
Location of Peak Heat Flux (Lower Wall)	*x/s* = 0
Average Effectiveness	0.6392 (63.92 %)
Peak Effectiveness	0.7230 (72.30 %)
Locations of Peak Effectiveness	15
Number of Schlieren Images	72

6.5: Experiment Summary Tables

Table 6.13: Summary table for unheated film test cases

	Test Case 0U	**Test Case 1U**	**Test Case 2U**	**Test Case 3U**
$T_{ambient}$	295 K	295 K	295 K	295 K
$P_{ambient}$	0.99 atm	0.99 atm	0.99 atm	0.99 atm
T_{film}	N/A	295 K	295 K	295 K
P_{film}	N/A	0.0644 atm	0.09013 atm	0.21376 atm
Film throttle valve setting	Closed	Partially Open (~15 %)	Partially Open (~20 %)	Partially Open (~40 %)
Burner inlet valve setting	Closed	Closed	Closed	Closed
Ω (Upper Wall)	1.67	N/A	N/A	0.995
Ω (Lower Wall)	1.67	N/A	N/A	0.8622
Average Heat Flux (Upper Wall)	2908 W/m^2	3028 W/m^2	3375 W/m^2	2488 W/m^2
Average Heat Flux (Lower Wall)	4308 W/m^2	3845 W/m^2	3586 W/m^2	3702 W/m^2
Peak Heat Flux (Upper Wall)	4770 W/m^2	4743 W/m^2	4971 W/m^2	5163 W/m^2
Location of Peak Heat Flux (Upper Wall)	x/s = 10	x/s = 10	x/s = 10	x/s = 10
Peak Heat Flux (Lower Wall)	6164 W/m^2	5725 W/m^2	5800 W/m^2	3259 W/m^2
Location of Peak Heat Flux (Lower Wall)	x/s = 15	x/s = 40	x/s = 40	x/s = 2.5
Average Effectiveness	N/A	0.1235 (12.35 %)	0.2106 (21.06 %)	0.5561 (55.61 %)
Peak Effectiveness	N/A	0.7576 (75.76 %)	0.72.44 (72.44 %)	0.6198 (61.98 %)
Locations of Peak Effectiveness	N/A	x/s = 7.5	x/s = 7.5	x/s = 32.5
Number of Schlieren Images	72	72	72	72

Table 6.14: Summary table for heated film test cases

	Test Case 1H	**Test Case 2H**	**Test Case 3H**
$T_{ambient}$	295 K	295 K	295 K
$P_{ambient}$	0.98 atm	0.98 atm	0.98 atm
T_{film}	330 K	330 K	330 K
P_{film}	0.0725 atm	0.10498 atm	0.27752 atm
Film throttle valve setting	Partially Open (~15 %)	Partially Open (~20 %)	Partially Open (~40 %)
Burner inlet valve setting	Partially Open (~5 %)	Partially Open (~15 %)	Partially Open (~25 %)
Ω (Upper Wall)	0.33	0.4372	0.9751
Ω (Lower Wall)	- 0.26	- 0.3588	- 0.5584
Average Heat Flux (Upper Wall)	3227 W/m^2	3338 W/m^2	3348 W/m^2
Average Heat Flux (Lower Wall)	3477 W/m^2	3153 W/m^2	1938 W/m^2
Peak Heat Flux (Upper Wall)	4742 W/m^2	4576 W/m^2	4891W/m^2
Location of Peak Heat Flux (Upper Wall)	x/s = 10	x/s = 10	x/s = 10
Peak Heat Flux (Lower Wall)	5148 W/m^2	5047 W/m^2	2648 W/m^2
Location of Peak Heat Flux (Lower Wall)	x/s = 40	x/s = 50	x/s = 0
Average Effectiveness	0.2874 (28.74 %)	0.3242 (32.42 %)	0.6392 (63.92 %)
Peak Effectiveness	0.7905 (79.05 %)	0.7539 (75.39 %)	0.7230 (72.30 %)
Locations of Peak Effectiveness	x/s = 7.5	x/s = 15	x/s = 15
Number of Schlieren Images	72	72	72

Chapter 7: Conclusion

7.1: Summary of Findings

The main goals of this thesis were to acquire and analyze large sets of experimental film cooling data for use in the validation of NASA's LOCI-CHEM computational fluid dynamics tool and develop a simple program that is able to accurately extract the geometry of important flow features in Schlieren photographs. Using the test matrix previously developed by Dellimore [5] and the film cooling experiment constructed by Maqbool [6], a large quantity of film cooling data at conditions relevant to the J-2X engine has been produced. Data for a minimum of 10 experiments at the conditions of each test case, with the exception of Test Case 1H (5 experiments), has been acquired.

All heat flux data has been analyzed using an analytical method for determining heat flux developed by Maqbool and is compared to available CFD data for each individual test case. In comparison with the unheated test cases, the numerical simulations by Loci-CHEM consistently over-predict the heat flux for both the upper and lower wall. The simulations are a much better fit to the subsonic heated film cases (Test Cases 1H and 2H). These results for the lower wall agree to within 19%, with the largest disagreements occurring near the film injection point. The supersonic heated film case (Test Case 3H) does not agree with the CFD predictions to any significant degree, with an average difference of over 50%. Additionally, Loci-CHEM under-predicts the heat flux into the wall in this test case, a departure from all previous test cases.

Film cooling effectiveness profiles for all test cases have been calculated and compared to the numerical results generated by Loci-CHEM. It was found that for all test cases with heated film, Loci-CHEM over-predicts the protection offered by the film. This over-estimation was the greatest near the film injection point. This trend was reversed for Test Case 3U, with Loci-CHEM under-predicting the film cooling effectiveness at almost all locations. The most significant disagreement between the experimental and numerical film cooling effectiveness profiles for all cases occurred at the film injection point.

In order to acquire the necessary heat flux data, the construction of a film heater was required. This film heater allowed the proper study of this film-heating experiment by ensuring that the recovery temperature of the film was between the wall temperature and the core flow temperature. Additionally, due to the failure of the experiment testing surfaces, several modifications were made to the experimental apparatus to increase the durability of the test section. These included increasing the depth of the temperature sensors, adding a radius to the heat flux gauge slugs, adding Heli-Coil® inserts to increase the strength of the MACOR® plates, and adding supports to decrease the load transferred to the lower testing surfaces.

Schlieren movies have been acquired and analyzed with machine vision techniques for all test cases. This was done through the use of code developed in MATLAB. All movies are processed into individual images and analyzed sequentially to extract significant flow features and geometries. These features can be overlaid on the original images to allow for better visual understanding and comparison. Additionally, all features are sorted and stored to allow the investigation

of individual flow features throughout the duration of the experiment. The expansion of the shear layer between the core and film flow could not be reliably extracted due to the quality of the Schlieren images obtained. The investigation of the shockwaves emanating from the film louver showed a significant change in angle between the subsonic test cases. This causes some unexpected fluctuation in the upper wall heat flux where the shockwave impinges on the upper testing surface. This phenomenon was further demonstrated by the practical application of using the data from the machine vision analysis to generate shock diagrams for the entire test section. It was seen that shock impingement locations greatly altered the heat flux on both the upper and lower wall.

7.2: Main Contributions

1.) A large set of fundamental film cooling data at conditions relevant to those found in a real world engine (NASA/Pratt &Whitney Rocketdyne J-2X) has been generated for use in code validation and for future comparison. Measured parameters include wall heat flux distributions, flow structures and geometry, and pressure data obtained at three separate film injection conditions.

2.) A new and innovative automated Schlieren image analysis tool has been developed to automatically extract line features and identify their geometry using machine vision techniques. This tool can be easily adapted to suit a variety of needs and provides quantitative data on flow structures in film cooling flows.

3.) The supersonic film cooling experiment developed by Maqbool has been completed and improved through the addition of a film heater and more robust components.

4.) Initial comparison of experimental results with numerical simulations by LOCI-CHEM indicates a good fit for subsonic film injection cases. The supersonic film injection cases do not match the CFD results as favorably.

7.3: Future Work

Recommendations for future work include:

1.) Improved Schlieren image quality through the use of high-speed camera and better light sources. This will greatly improve the feature detection allowed through machine vision analysis.

2.) Continued development and usage of machine vision techniques to analyze high-speed Schlieren images. This will allow the study of startup phenomenon and allow closer examination of the flow features at the film injection point.

3.) Modification to current testing apparatus to allow the study of a favorable pressure gradient experiment. This would better simulate the conditions found in a real-world rocket nozzle.

4.) Modification to testing apparatus and nozzle configuration to eliminate shockwaves caused by poor design. This will increase the reliability of future data throughout the testing region by eliminating several impingement locations.

5.) Modification to testing apparatus to allow for the controlled movement of shock-boundary layer interaction point. This will allow for the study of the effect of shock impingement on film cooling effectiveness.

Appendices

Appendix A: Schlieren Analysis MATLAB Code

```
% Code to Extract Frames from Video, Process Images and Identify Angles
% Creates individual images for each frame of movie. Also creates text
% files Angles.txt, X1.txt, X2.txt, Y1.txt, Y2.txt. These hold information
% for post processing Hough Line constructs.

clear all
close all
clc

% Initial Input
vid = input('Name of file: ','s');
sigma = input('Value of Sigma: ');
MinLength = input('Minimum length for Hough Lines (positive real scalar): ');
FillGap = input('Cutoff length for filling Hough Lines(positive real scalar): ');

%% Video Frame Extraction
% Create Movie Object
tic
readerobj = VideoReader(vid);
nFrames = get(readerobj, 'numberOfFrames');
nFrames = nFrames-1;

% Extract Frames and Output to File
for k = 1 : nFrames
    % Extract Frames
    vidFrame = read(readerobj,k);
    mov.cdata = vidFrame;
    % Crop Image (remove useless data)
    mov.cdata = imcrop(mov.cdata,[400,100,600,400]);
    % Write to File
    imagename=strcat(int2str(k), '.jpg');
    imwrite(mov.cdata, strcat('Frame-',imagename));
    % Print Current Frame to Command Window
    p = 100*k/nFrames;
    disp(['Extracted frame ', num2str(k),', ', num2str(p),'% done.']);
end

disp(['Finished Frame Extraction']);

%% Image Analysis
%Preallocate
Angles = zeros(nFrames,2);

% Image Processing Loop
for i = 1:nFrames
    % File Address
    imagename = strcat(int2str(i), '.jpg');
    file = strcat('Frame-',imagename);
```

```
    % Image Conversion
    IMG = imread(file);
    IMG = im2double(IMG);
    GRY = rgb2gray(IMG);

    % Edge Detection
    figure
    CN = edge(GRY,'canny',[],sigma);
    close

    % Perform Hough Transform to Find Angles
    [H,theta,rho] = hough(CN,'Theta',-90:0.05:89);
    peaks = houghpeaks(H,10);
    lines = houghlines(CN,theta,rho,peaks,'FillGap',FillGap,'MinLength',MinLength);

    % Store Angles and Corresponding Endpoints
    for j = 1:length(lines)
       Angles(i,j) = lines(j).theta + 90;
       X1(i,j) = lines(j).point1(1);
       Y1(i,j) = lines(j).point1(2);
       X2(i,j) = lines(j).point2(1);
       Y2(i,j) = lines(j).point2(2);
    end
    close all

    % Print Current Frame to Command Window
    p = 100*i/nFrames;
    disp(['Finished processing frame: ', num2str(i),', ', num2str(p),'% done.']);
end

dlmwrite('Angles.txt', Angles,'delimiter','\t');
dlmwrite('X1.txt', X1,'delimiter','\t')
dlmwrite('Y1.txt', Y1,'delimiter','\t')
dlmwrite('X2.txt', X2,'delimiter','\t')
dlmwrite('Y2.txt', Y2,'delimiter','\t')
disp(['Finished Processing All Frames']);
toc
```

```
% This code rearranges Angles.txt according to x1 and y1 locations and
% calculates: average shock angle, fluctuation of shock angles during the duration of the
% experiment. Other useful information is plotted.

clear all
close all
clc

% Read in Arrays of Data from .txt files
tic
Angles = dlmread('Angles.txt');
X1 = dlmread('X1.txt');
X2 = dlmread('X2.txt');
Y1 = dlmread('Y1.txt');
Y2 = dlmread('Y2.txt');

% Detect tunnel startup in images and select frames to use
for i = 1:length(Angles)
   if Angles(i,4) > 0
      StartFrame = i;
      EndFrame = StartFrame + (6*24);
      break
   end
end

% Trim Angles, X1, X2, Y1, and Y2 to correct size
j = 1;
for i = StartFrame:EndFrame
      ANGTRIM(j,:) = Angles(i,:);
      X1TRIM(j,:) = X1(i,:);
      Y1TRIM(j,:) = Y1(i,:);
      X2TRIM(j,:) = X2(i,:);
      Y2TRIM(j,:) = Y2(i,:);
      j = j + 1;
end

% Plot Shock Angles and Positions
[imax, jmax] = size(ANGTRIM);
for i = 1:imax
   for j = 1:jmax
      XHalf(i,j) = (X1TRIM(i,j) + X2TRIM(i,j))/2;
      YHalf(i,j) = (Y1TRIM(i,j) + Y2TRIM(i,j))/2;
      if XHalf(i,j) > 0
            subplot(2,2,1)
            plot3(XHalf(i,j),YHalf(i,j), ANGTRIM(i,j),'rx')
            hold on
            grid on
            axis([0 500 0 500 0 200])
            xlabel('X position (pixels)');
            ylabel('Y position (pixels)');
            zlabel('Angle (degrees)');
            title('3D View of Shock Angles vs Location of Mid Shock')
            subplot(2,2,2);
            plot (XHalf(i,j), YHalf(i,j),'cx')
            hold on
```

```
            grid on
            axis([0 500 0 500])
            xlabel('X position (pixels)');
            ylabel('Y position (pixels)');
            title('X and Y Coordinates of Mid Shock')
            subplot(2,2,3);
            plot (XHalf(i,j), ANGTRIM(i,j),'bx')
            hold on
            grid on
            axis([0 500 0 200])
            xlabel('X position (pixels)');
            ylabel('Angle (degrees)');
            title('Shock Angle vs X Location of Mid Shock')
            subplot(2,2,4);
            plot (YHalf(i,j), ANGTRIM(i,j),'gx')
            hold on
            grid on
            axis([0 500 0 200])
            xlabel('Y position (pixels)');
            ylabel('Angle (degrees)');
            title('Shock Angle vs Y Location of Mid Shock')

        end
    end
end

% Create Median Midpoint Line Location Matrix
S = (EndFrame - StartFrame)/2;
if rem(S,1) ~= 0
    S = S + 0.5;
end
for x = S:(EndFrame - StartFrame)
    if XHalf(x,7) > 0
        break
    end
    S = S+1;
end

MLL(1,:) = XHalf(S,:);
MLL(2,:) = YHalf(S,:);
MLL(3,:) = ANGTRIM(S,:);

% Loop to Organize Angles by midline locations
c1 = 0;c2 = 0;c3 = 0;c4 = 0;c5 = 0;c6 = 0;c7 = 0;
PM = 12.5;
for i = 1:imax
    for j = 1:jmax
        % IF Logic to compare to Midline Locations
        if XHalf(i,j) > (MLL(1,1)-PM) && XHalf(i,j) < (MLL(1,1)+PM)
            if YHalf(i,j) > (MLL(2,1)-PM) && YHalf(i,j) < (MLL(2,1)+PM)
                if ANGTRIM(i,j) > (MLL(3,1)-2) && ANGTRIM(i,j) < (MLL(3,1)+2)
                    c1 = c1+1;
                    Line1(c1,1) = XHalf(i,j);
                    Line1(c1,2) = YHalf(i,j);
                    Line1(c1,3) = ANGTRIM(i,j);
```

```
        end
    end
end
if XHalf(i,j) > (MLL(1,2)-PM) && XHalf(i,j) < (MLL(1,2)+PM)
    if YHalf(i,j) > (MLL(2,2)-PM) && YHalf(i,j) < (MLL(2,2)+PM)
        if ANGTRIM(i,j) > (MLL(3,2)-2) && ANGTRIM(i,j) < (MLL(3,2)+2)
            if ANGTRIM(i,j) ~= 0
                c2 = c2+1;
                Line2(c2,1) = XHalf(i,j);
                Line2(c2,2) = YHalf(i,j);
                Line2(c2,3) = ANGTRIM(i,j);
            end
        end
    end
end
if XHalf(i,j) > (MLL(1,3)-PM) && XHalf(i,j) < (MLL(1,3)+PM)
    if YHalf(i,j) > (MLL(2,3)-PM) && YHalf(i,j) < (MLL(2,3)+PM)
        if ANGTRIM(i,j) > (MLL(3,3)-1) && ANGTRIM(i,j) < (MLL(3,3)+1)
            c3 = c3+1;
            Line3(c3,1) = XHalf(i,j);
            Line3(c3,2) = YHalf(i,j);
            Line3(c3,3) = ANGTRIM(i,j);
        end
    end
end
if XHalf(i,j) > (MLL(1,4)-PM) && XHalf(i,j) < (MLL(1,4)+PM)
    if YHalf(i,j) > (MLL(2,4)-PM) && YHalf(i,j) < (MLL(2,4)+PM)
        if ANGTRIM(i,j) > (MLL(3,4)-2) && ANGTRIM(i,j) < (MLL(3,4)+2)
            c4 = c4+1;
            Line4(c4,1) = XHalf(i,j);
            Line4(c4,2) = YHalf(i,j);
            Line4(c4,3) = ANGTRIM(i,j);
        end
    end
end
if XHalf(i,j) > (MLL(1,5)-PM) && XHalf(i,j) < (MLL(1,5)+PM)
    if YHalf(i,j) > (MLL(2,5)-PM) && YHalf(i,j) < (MLL(2,5)+PM)
        if ANGTRIM(i,j) > (MLL(3,5)-2) && ANGTRIM(i,j) < (MLL(3,5)+2)
            c5 = c5+1;
            Line5(c5,1) = XHalf(i,j);
            Line5(c5,2) = YHalf(i,j);
            Line5(c5,3) = ANGTRIM(i,j);
        end
    end
end
if XHalf(i,j) > (MLL(1,6)-PM) && XHalf(i,j) < (MLL(1,6)+PM)
    if YHalf(i,j) > (MLL(2,6)-PM) && YHalf(i,j) < (MLL(2,6)+PM)
        if ANGTRIM(i,j) > (MLL(3,6)-2) && ANGTRIM(i,j) < (MLL(3,6)+2)
            c6 = c6+1;
            Line6(c6,1) = XHalf(i,j);
            Line6(c6,2) = YHalf(i,j);
            Line6(c6,3) = ANGTRIM(i,j);
        end
    end
end
if XHalf(i,j) > (MLL(1,7)-PM) && XHalf(i,j) < (MLL(1,7)+PM)
```

```
            if YHalf(i,j) > (MLL(2,7)-PM) && YHalf(i,j) < (MLL(2,7)+PM)
                if ANGTRIM(i,j) > (MLL(3,7)-1) && ANGTRIM(i,j) < (MLL(3,7)+1)
                    c7 = c7+1;
                    Line7(c7,1) = XHalf(i,j);
                    Line7(c7,2) = YHalf(i,j);
                    Line7(c7,3) = ANGTRIM(i,j);
                end
            end
        end
    end
end

f = (EndFrame-StartFrame)+1;
ig1 = (length(Line1));
ig2 = (length(Line2));
ig3 = (length(Line3));
ig4 = (length(Line4));
ig5 = (length(Line5));
ig6 = (length(Line6));
ig7 = (length(Line7));
disp([num2str(ig1),' of ', num2str(f),' frames exhibit Shock 1']);
disp([num2str(ig2),' of ', num2str(f),' frames exhibit Shock 2']);
disp([num2str(ig3),' of ', num2str(f),' frames exhibit Shock 3']);
disp([num2str(ig4),' of ', num2str(f),' frames exhibit Shock 4']);
disp([num2str(ig5),' of ', num2str(f),' frames exhibit Shock 5']);
disp([num2str(ig6),' of ', num2str(f),' frames exhibit Shock 6']);
disp([num2str(ig7),' of ', num2str(f),' frames exhibit Shock 7']);

% Compute Averages along Lines
Mean1 = mean(Line1(:,3),1);
Mean2 = mean(Line2(:,3),1);
Mean3 = mean(Line3(:,3),1);
Mean4 = mean(Line4(:,3),1);
Mean5 = mean(Line5(:,3),1);
Mean6 = mean(Line6(:,3),1);
Mean7 = mean(Line7(:,3),1);

% Plot
figure
hold on
plot(1,Mean1,'bo','LineWidth',2)
plot(2,Mean2,'go','LineWidth',2)
plot(3,Mean3,'ro','LineWidth',2)
plot(4,Mean4,'yo','LineWidth',2)
plot(5,Mean5,'co','LineWidth',2)
plot(6,Mean6,'mo','LineWidth',2)
plot(7,Mean7,'ko','LineWidth',2)
grid on
xlabel('Shock Number')
ylabel('Shock Angle (degrees)')
legend('Shock 1','Shock 2','Shock 3','Shock 4','Shock 5','Shock 6','Shock 7','Location','NorthWest')
axis([0 8 -5 180])

% Shock Fluctuation
Lines = {Line1(:,3) Line2(:,3) Line3(:,3) Line4(:,3) Line5(:,3) Line6(:,3) Line7(:,3)};
```

```
Means = [Mean1 Mean2 Mean3 Mean4 Mean5 Mean6 Mean7];
t1 = 2.0106;t2 = 1.9766;t3 = 1.9858;t4 = 1.9787;t5 = 1.9768;t6 = 1.9847;t7 = 1.9901;
T = [t1 t2 t3 t4 t5 t6 t7];
Lengths = [length(Line1) length(Line2) length(Line3) length(Line4) length(Line5) length(Line6)
length(Line7)];
for i = 1:length(Means)
   a = 0;
   Line = Lines{1,i};
   for j = 1:Lengths(i)
      SVInter(i) = (Line(j,1)-Means(1,i))^2;
      a = a +SVInter(i);
   end
   SampleVar(i) = a/(Lengths(1,i)-1);
   StdDev(i) = sqrt(SampleVar(i));
   StdDevMeans(i) = StdDev(i)/sqrt(Lengths(1,i));
   RandErr(i) = T(1,i)*StdDevMeans(i);
end

figure
S0 = errorbar(1,Means(1,1),RandErr(1,1));
set(S0,'LineWidth', 1, 'Marker', 'o','MarkerSize', 7,'MarkerEdgeColor' ,...
   [.2 .2 .2], 'MarkerFaceColor', [.2 .2 .2],'LineStyle','none');
hold on
S1 = errorbar(2,Means(1,2),RandErr(1,2));
set(S1,'LineWidth', 1, 'Marker', 'o','MarkerSize', 7,'MarkerEdgeColor' ,...
   [.2 .2 .2], 'MarkerFaceColor', [.3 .3 .3],'LineStyle','none');
S2 = errorbar(3,Means(1,3),RandErr(1,3));
set(S2,'LineWidth', 1, 'Marker', 'o','MarkerSize', 7,'MarkerEdgeColor' ,...
   [.2 .2 .2], 'MarkerFaceColor', [.4 .4 .4],'LineStyle','none');
S3 = errorbar(4,Means(1,4),RandErr(1,4));
set(S3,'LineWidth', 1, 'Marker', 'o','MarkerSize', 7,'MarkerEdgeColor' ,...
   [.2 .2 .2], 'MarkerFaceColor', [.5 .5 .5],'LineStyle','none');
S4 = errorbar(5,Means(1,5),RandErr(1,5));
set(S4,'LineWidth', 1, 'Marker', 'o','MarkerSize', 7,'MarkerEdgeColor' ,...
   [.2 .2 .2], 'MarkerFaceColor', [.6 .6 .6],'LineStyle','none');
S5 = errorbar(6,Means(1,6),RandErr(1,6));
set(S5,'LineWidth', 1, 'Marker', 'o','MarkerSize', 7,'MarkerEdgeColor' ,...
   [.2 .2 .2], 'MarkerFaceColor', [.8 .8 .8],'LineStyle','none');
S6 = errorbar(7,Means(1,7),RandErr(1,7));
set(S6,'LineWidth', 1, 'Marker', 'o','MarkerSize', 7,'MarkerEdgeColor' ,...
   [.2 .2 .2], 'MarkerFaceColor', [.9 .9 .9],'LineStyle','none');
grid on
xlabel('Shock Number')
ylabel('Shock Angle (degrees)')
legend('Shock 1','Shock 2','Shock 3','Shock 4','Shock 5','Shock 6','Shock 7','Location','NorthWest')
title('Shock Angle vs. Shock Number with Errorbars');
axis([0.5 7.5 -5 180])


toc
```

Appendix B: Sample Schlieren Images

Test Case 0

Test Case 1

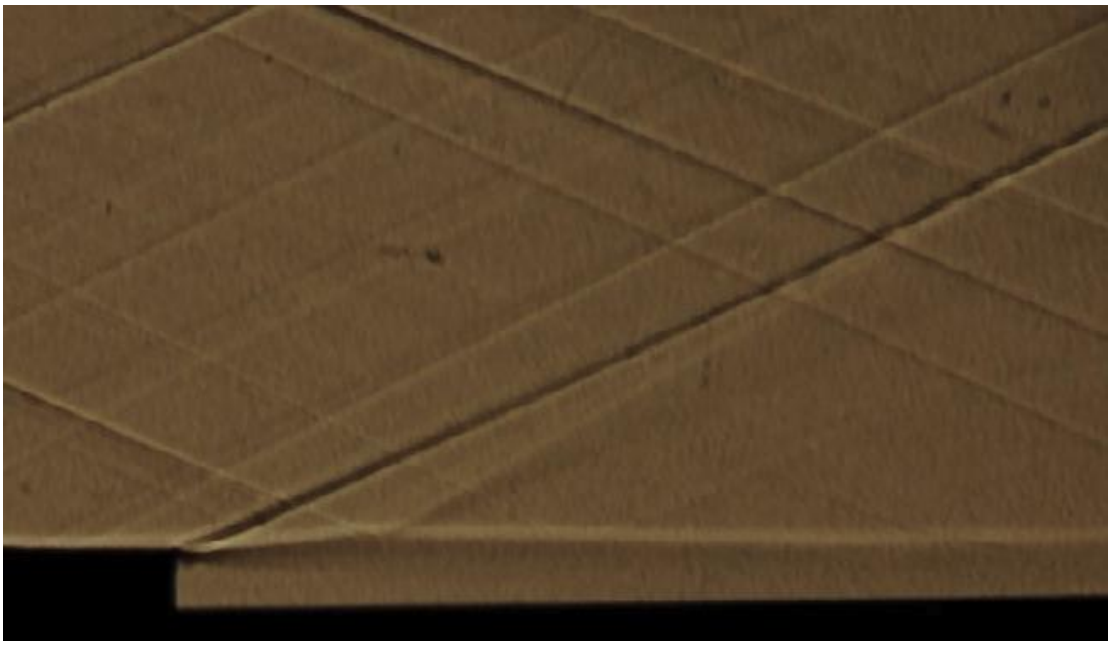

Test Case 2

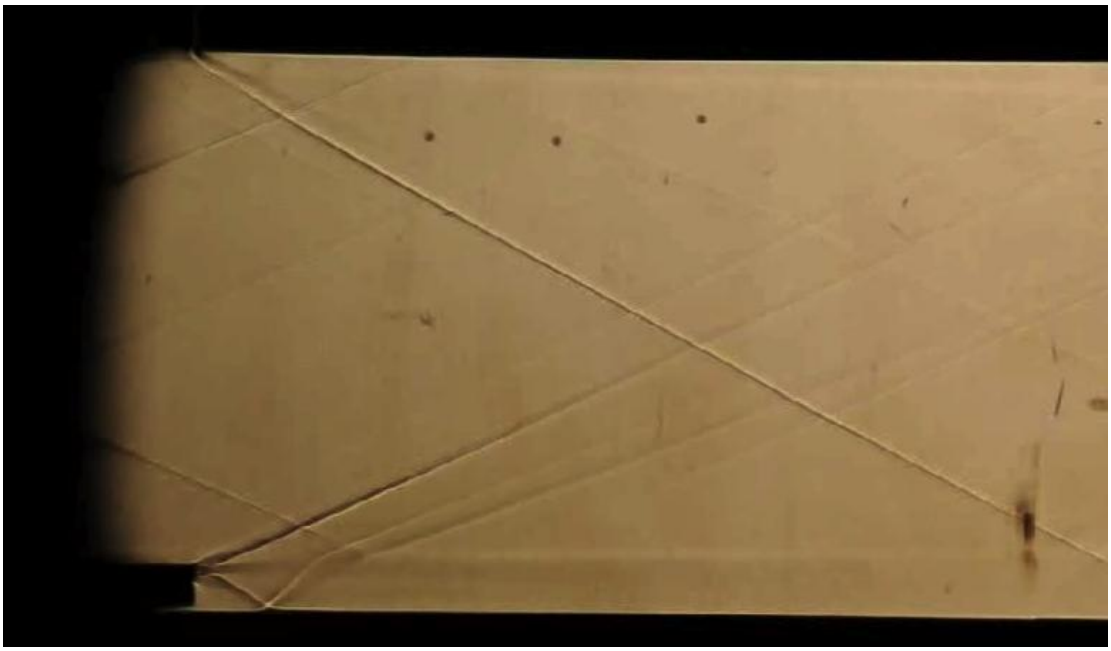

Test Case 3

Bibliography

[1] Sutton, G. P. and Biblarz, O., "Rocket Propulsion Elements," *7th Edition, Wiley-Interscience, 2000.*

[2] Kerrebrock, J. L., "Aircraft Engines and Gas Turbines," *2nd Edition, The MIT Press, 1992.*

[3] Campbell, J.G., Batha, D.R., Carey, M.D., Nagy, A.R., and Stechman, R.C., "Thrust Chamber Cooling Techniques for Spacecraft Engines," *NASA Technical Documents*, July, 1963.

[4] Toyama, S., "Numerical Analysis of Nozzle Cooling for Upper-stage Liquid Rocket Engines," AIAA2005-387, AIAA 43rd Aerospace Sciences Meeting, January 2005, Reno, NV.

[5] Dellimore, K., "Modeling and Simulation of Mixing Layer Flows For Rocket Engine Film Cooling," *Ph.D. dissertation, University of Maryland, 2010.*

[6] Maqbool, D. (2011). Development of an experiment for Measuring Film Cooling Performance in Supersonic Flows. M.S. Thesis, University of Maryland.

[7] Thomas F. Irvine, J., *Advances in Heat Transfer* (Vol. 7). New York, New York, US Academic Press, 1971.

[8] Hansmann, T., Wilhelmi, H., and Bohn, D., "An Experimental Investigation of the Film Cooling Process at High Temperatures and Velocities," *AIAA-93-5062, AIAA/DGLR 5th International*

[9] Adrian, R., Scattering particle characteristics and their effect on pulsed laser measurements of fluid flow: speckle velocimetry vs. particle image velocimetry. *Applied Optics*, 23, 1690-1691, 1984.

[10] Pawalak, G. and Armi, L., "Vortex Dynamics in a Spatially Accelerating Shear Layer," *Journal of Fluid Mechanics*, 376, pp. 1-35, 1991.

[11] Samimy, M. and Lele, S.K., "Motion of Particles with Inertia in a Compressible Free Shear Layer," *Physics of Fluids,* Vol. 3, 1991.

[12] Settles, G. S., "Schlieren and Shadowgraphy Techniques: Visualizing Phenomena in Transparent Media," *Springer-Verlag, Berlin/New York/Heidelber, 2001*.

[13] Papamoschou, D. and Roshko, A., "The Compressible Turbulent Shear Layer: an Experimental Study," *Journal of Fluid Mechanics*, Vol. 197, pp. 453-477, 1988.

[14] Smith, N., "Extraction of Oblique Structures in Noisy Schlieren Sequences Using Computer Vision Techniques," *AIAA Journal*, Vol. 50, No, 5, 2012, pp. 1145-1155.

[15] Boden, R. H., "Heat Transfer in Rocket Motors and the Application of Film and Sweat Cooling," *Transactions of ASME*, Vol. 73, 1951, pp. 385-390.

[16] Goldstein, R. J., Eckert, E. R. G., Tsou, F. K., and Haji-Sheikh, A., "Film Cooling with Air and Helium Injection Through a Rearward-Facing Slot into a Supersonic Air Flow," *AIAA Journal*. Vol. 4, pp. 981-985. June 1966.

[17] Juhany, K. A. and Hunt, M. L., "Flow-Field Measurements in Supersonic Film Cooling Including the Effect of Shock Wave Interaction," AIAA-92-2950, AIAA 27th Thermophysics Conference, July 1992, Nashville, T.
[18] Bass, R., Hardin, L., and Rodgers, R., "Supersonic Film Cooling," *AIAA-90-5239, AIAA 2nd International Aerospace Planes Conference, Oct. 1990, Orlando, FL*.
[19] Aupoix, B., Mignosi, A., Viala, S., Bouvier, F., and Gaillard, R., "Experimental and Numerical Study of Supersonic Film Cooling," *AIAA Journal,* Vol. 36 no. 6, pp. 915-923, 1998.
[20] Vuillermoz, P., Weiland, C., Aupoix, B., Grosdemange, H., and Bigert, M., "Advanced Nozzle Technology for Gryogenic Engines," *Second International Symposium on Liquid Rocket Propulsion*, ONERA, Chatillon, France, 1995, pp. 23-1-23-20.
[21] Krehl, P. and Engemann, S., "August Toepler – the first who visualized shock waves," *Shock Waves*, Vol. 5, pp. 1-18, 1995.
[22] Settles, Gary S., "Schlieren and Shadowgraph Techniques: Visualizing Phenomena in Trapnsparent Media," *1st Edition, Springer, 2001*.
[23] Cranz, C. Schardin, H., "Kinematographie auf rhendem film und mit extrem hoher Bildfrequenz," *Z. Phys.* Vol. 56, pp. 147-183, 1929.
[24] Schardin, H., "Schlieren Methods and Their Applications," *Ergebnisse der Exakten Naturwissenshaften,* Vol. 20, pp. 303-439, 1942 (English translation: NASA TT F-12,732).
[25] Canny, J., "A Computational Approach to Edge Detection," *IEEE Transactions on Pattern Analysis and Machine Intelligence,* Vol. PAMI-8, No. 6, pp. 679-698, 1986.
[26] Deriche, R., "Using Canny's criteria to drive a recursively implemented optimal edge detector", *Int. J. Computer Vision,* Vol. 1, pp. 167-187, 1987.
[27] Luo. Y., and Duraiswami, R., "Canny edge detection on NVIDIA CUDA", in: *Computer Vision and Pattern Recognition Workshops*, IEEE Computer Society Press, 2008.
[28] Diller, T.E., "Advances in Heat Flux Measurements," *Advances in Heat Transfer*, Voume 23, 1993.
[29] Schults, D.L. and Jones, T.V., "Heat Transfer Measurements in Short-DurationHypersonic Facilities," *AGARD Report,* AGARD-AG-165, 1973.
[30] Incropera, F.P., "Fundamentals of Heat and Mass Transfer," *6th Edition, Wiley & Sons, 2007*.
[31] Chen. C.J., and Chiou, J.S., "Prediction of Surface Temperature and Heat Flux from an Interior Temperature Response," *Letters in Heat and Mass Transfer*, Vol. 3, pp. 539-548, 1972.
[32] Monde, M., "Analytical Method in Inverse Heat Transfer Problem using Laplace Transform Technique," *International Journal of Heat and Mass Transfer*, Vol. 43, pp. 3965-3975, 2000.
[33] Beck, J.V., Blackwell, B., and Haji-Sheikh,A., "Comparison of Some Inverse Heat Conduction Methods using Experimental Data," *International Journal of Heat and Mass Transfer*, vol. 39, no. 17, 1996, pp. 3659 – 3657.

[34] Ozisik, M.N. and Orlande, H.R.B., " Inverse Heat Transfer," *Taylor and Francis*, 2000.
[35] Chen, C.J. and Thomsen, D.M., "On Determination of Transient Surface Temperature and Heat Flux by Embedded Thermocouples in a Hollow Cylinder," *AIAA Journal*, vol. 13, no. 5, 1975, pp. 697 – 699.
[36] Chen, C.J. and Chiou, J.S., "Prediction of Surface Temperature and Heat Flux from an Interior Temperature Response," *Letters in Heat and Mass Transfer*, vol.3, 1974, pp. 539 – 548.
[37] Imber, M. and Khan, J., "Prediction of Transient Temperature Distributions with Embedded Thermocouples," *AIAA Journal*, vol. 10, no. 6, 1972, pp. 784 – 789.
[38] Monde, M., "Analytical Method in Inverse Heat Transfer Problem using Laplace Transform Technique," *International Journal of Heat and Mass Tansfer*, vol. 43, 2000, pp. 3965 – 3975.
[39] Yan, X.T., "On the Thermal Penetration Depth in Fourier Heat Conduction," *8th AIAA/ASME Joint Thermophysics and Heat Transfer Conference,* June 2002, St. Louis, MO.
[40] Anderson, J.D., "Modern Compressible Flow: With Historical Perspective", *McGraw –Hill Science/Engineering/Math, 3rd Edition, July 2002.*
[41] Young, W.C., and Budynas, R.G., "Roark's Formulas for Stress and Strain", *McGraw-Hill Professional, 7th Edition, September 2001.*
[42] Pilkey, W.D., Pilkey, D.F., "Peterson's Stress Concentration Factors", *John Wiley & Sons, 3rd Edition, January 2008.*
[43] J. Adams, K. Parulski, and K. Spaulding, "Color processing in digital cameras," *IEEE Micro*, vol. 18, no. 6, pp. 20-31, 1998.
[44] B. Gunturk, J. Glotzbach, Y. Altunbasak, R. Schager, and R. Mersereau, "Demosaicking: Color Filter Array Interpolation," *IEEE Signal Processing Magazine*, vol. 22, no. 1, pp. 44-54, 2005.
[45] *Bayer Image of Statue.* Photograph. n.d. Cambridge in Colour, Digital Camera Sensors. *http://www.cambridgeincolour.com/tutorials/camera-sensors.htm.* 06 June 2013.
[46] Menter, F. R., "Two-Equation Eddy-Viscosity Turbulence Models for Engineering Applications," *AIAA Journal*, Vol. 32, 1994, pp. 269-289.
[47] Cruz, C., "Experimental and Numerical Characterization of Turbulent Slot Film Cooling," *Ph.D. dissertation, University of Maryland, 2008.*
[48] "Test Uncertainty," ASME PTC 19.1-1998, American Society of Mechanical Engineers.